ABSTRACT

Title of dissertation: MAGNETISM AND SUPERCONDUCTIVITY IN TOPOTACTICALLY MODIFIED TRANSITION METAL CHALCOGENIDES

Brandon Cody Wilfong
Doctor of Philosophy, 2020

Dissertation directed by: Professor Efrain Rodriguez
Department of Chemistry and Biochemistry

Professor Johnpierre Paglione
Department of Physics

Inspired by the structure of the simplest iron-based chalcogenide superconductor, FeSe, the class of tetrahedral transition metal chalcogenides (TTMCs) exhibit interesting chemical and physical properties due to its structure. This structure consists of tetrahedrally coordinated transition metal chalcogenides stacked to form two dimensional layers held together by van der Waals forces. This structure and its associated tetrahedral coordination of transition metal to chalcogenide, square transition metal sublattice, van der Waals layered structure, and *d*-electron filling at the Fermi level yields interesting properties from superconductivity to frustrated itinerant magnetism.

In this dissertation work, we demonstrate that the anti-PbO type Fe*Ch* (*Ch* = S, Se, Te) structure offers a perfect platform for the study of superconductivity in the iron-based system as well as new physics as the class is expanded to different transition metals. Prior to this work, the binaries of the TTMC family was limited to iron, but has been expanded

to cobalt. In the cobalt compound, CoSe, superconductivity in the FeSe binary is suppressed and a frustrated spin glass-like magnetic state emerges. Beyond the binaries, we have shown that topotactic hydrothermal synthetic routes on the iron chalcogenide system can lead to novel intercalated phases where long range magnetic order can co-exist with superconductivity in the (LiOH)FeSe system. This synthetic scheme also allows the intercalation of organic molecules, specifically ethylenediamine, to form organic-inorganic hybrids which can offer a new avenue for designing heterolayer compounds with complex interlayer interactions and bonding.

MAGNETISM AND SUPERCONDUCTIVITY IN TOPOTACTICALLY MODIFIED TRANSITION METAL CHALOCGENDIES

by

Brandon Cody Wilfong

Dissertation submitted to the Faculty of the Graduate School of the
University of Maryland, College Park in partial fulfillment
of the requirements for the degree of
Doctor of Philosophy
2020

Advisory Committee:
Professor Efrain Rodriguez, Chair/Co-advisor
Professor Johnpierre Paglione, Co-advsior
Professor Ichiro Takeuchi
Professor Andrei Vedernikov
Professor Nicholas Butch

© Copyright by
Brandon Cody Wilfong
2020

Foreward

The following is a list of all the manuscripts that I have contributed to during my time as a graduate student those marked as under review, in submission, or in preparation denote manuscripts which have yet to be officially published. An asterisk denotes manuscripts that make up the work described in this thesis.

* Zhou, X.; Wilfong, B.; Vivanco, H.; Paglione, J.; Brown, C. M.; and Rodriguez, E. E. Metastable layered cobalt chalcogenides from topochemical deintercalation. *J. Am. Chem. Soc.* **2016**, 138(50), 16432-16442.

Larson, A. M.; Wilfong, B.; Moetakef, P.; Brown, C. M; Zavalij, P.; and Rodriguez, E. E. Metal–insulator transition tuned by magnetic field in $Bi_{1.7}V_8O_{16}$ hollandite. *J. Mater. Chem. C*. **2017**, 5(20), 4967-4976.

Zhou, X.; Eckberg, C.; Wilfong, B.; Liou, S. C.; Vivanco, H. K.; Paglione, J.; and Rodriguez, E. E. Superconductivity and magnetism in iron sulfides intercalated by metal hydroxides. *Chem. Sci.* **2017**, 8(5), 3781-3788.

Zhou, X.; Wilfong, B.; Liou, S. C.; Hodovanets, H.; Brown; C. M., and Rodriguez, E. E. Proton and ammonia intercalation into layered iron chalcogenides. *Chem. Comm.* **2018**, 54(50), 6895-6898.

* Wilfong, B.; Zhou, X.; Vivanco, H.; Campbell, D. J.; Wang, K.; Graf, D.; Paglione, J.; and Rodriguez, E. E. Frustrated magnetism in the tetragonal CoSe analog

of superconducting FeSe. *Phys. Rev. B*. **2018**, 97(10), 104408.

Virtue, A.; Zhou, X.; Wilfong, B.; Lynn, J. W.; Taddei, K.; Zavalij, P.; Wang, L.; and Rodriguez, E. E. Magnetic order effects on the electronic structure of K*M*MnS_2 (*M*= Cu, Li) with the $ThCr_2Si_2$-type structure. *Phys. Rev. Mater.*, **2019**, 3(4), 044411.

Zhou, X.; Wang, L.; Fan, X.; Wilfong, B.; Liou, S. C.; Wang, Y.; Zheng, H.; Feng, Z.; Wang, C.; and Rodriguez, E. E. (2020). Isotope Effect between H_2O and D_2O in Hydrothermal Synthesis. *Chem. Mater.* **2020**, 32(2), 769-775.

* Wilfong, B.; Zhou, X.; Zheng, H.; Babra, N.; Brown, C. M.; Lynn, J. W.; Taddei, K.; Paglione, J.; and Rodriguez, E. E. Long range magnetic order in hydroxide layer doped ($Li_{1-xy}Fe_xMn_yOD$) FeSe. arXiv preprint arXiv:1912.09329, *under review*.

* Wilfong, B.; Zhou, Z.; Zheng, H.; Jayathilake, R.; Campbell, D.J.; Liou, S.C.; Paglione, J.; and Rodriguez, E.E. Alkali metal-free hydrothermal synthesis of ethylenediamine intercalated iron chalcogenides. *in preparation*.

Campbell, D.J.; Wilfong, B.; Zic, M.; Zavalij, P.; Rodriguez, E.E.; and Paglione, J. Preparation and Properties of KCo_2As_2 Single Crystals. *in preparation*.

Dedication

To my parents who have supported me in every aspect of my life and have given me every opportunity to pursue and achieve any goal I desired. And to my best friend, Elizabeth Cardosa who's love and support has made everything possible.

Acknowledgments

I would like to thank both of my advisors Professor Efrain Rodriguez and Professor Johnpierre Paglione for guidance and support for this dissertation work. I would also like to thank my other committee members, Professors Ichiro Takeuchi, Andrei Vedernikov, and Nicholas Butch for their time to review this dissertation and valuable advice to improve this work.

I want to thank the present and past members of the Rodriguez and Paglione groups for their assistance with experiments and pleasant company: Xiuquan Zhou, Huafei Zheng, Stephanie Gnewuch, Timothy Diethrich, Lahari Balisetty, Austin Virtue, Amber Larson, Tianyu Li, Daniel Campbell, Chris Eckberg, Connor Roncaioli, Halyna Hodovanets, Shanta Saha, I-Lin Liu. In particular, my collaboration with Dr. Xiuquan Zhou led to an incredible 3 years of learning, productivity and friendship which made this thesis work possible. I am grateful to the three undergraduate students who helped with my research in the chemistry and physics departments: Hector Vivanco, Navneeth Babra and Mark Zic. This work could not have been done without all of their help over these five years.

I would like to thank Drs. Peter Zavalij, Sz-Chian Liou, and Marya Anderson at the University of Maryland user facilities for their assistance with structural, microscopy, and elemental analysis analysis. I would also like to thank Drs. Craig Brown, Jeffrey Lynn, Jose Rodriguez, Yiming Qui, Keith Taddei, and Simon Kimber for their assistance with neutron scattering and spectroscopy.

Research at the University of Maryland was supported by the NSF Career DMR-1455118, AFOSR Grant No. FA9550-14-10332, and the Gordon and Betty Moore Foun-

dation Grant No. GBMF4419. We also acknowledge support from the Maryland Nanocenter and Center for Nanophysics and Advanced Materials. We acknowledge the support of the National Institute of Standards and Technology, U. S. Department of Commerce, in providing the neutron research facilities used in this work. The use of the Advanced Photon Source at Argonne National Laboratory was supported by the U. S. Department of Energy, Office of Science, Office of Basic Energy Sciences, under Contract No. DE-AC02-06CH11357. In particular, we acknowledge the use of 11-BM and 17-BM through collaboration with Dr. Andrey Yakovenko. We acknowledge the University of Maryland supercomputing resources (http://www.it.umd.edu/hpcc) made available for conducting the research reported in this work.

Lastly, I cannot be more thankful for the support of my friends and family of the past five years. Doctoral coursework and research can be intensely difficult at times and the unwavering support of my friends and family, even when they don't know what I am talking about, has made this process not only doable but enjoyable. In particular, Elizabeth and Matt have been constants and helped make the past five years a time of learning and personal growth for which I am incredibly thankful.

Contents

List of Tables

List of Figures

List of Abbreviations

2D	two-dimensional
AFM	antiferromagnetic
BCS	Bardeen-Cooper-Schrieffer
CSD	Cambridge Structural Database
Ch	chalcogenide
DSC	differential scanning calorimetry
EDA	ethylenediamine
EDS	energy dispersive X-ray spectroscopy
DFT	density functional theory
FC	field-cooled
FM	ferromagnetic
GGA	generalized gradient approximation
ICP-AES	inductively coupled plasma atomic emission spectroscopy
ICSD	Inorganic Crystallographic Structural Database
MPMS	magnetic properties measurement system
NCNR	NIST Center for Neutron Research
NPD	neutron powder diffraction
PAW	projector augmented wave
Pn	pnictide
PPMS	physical property measurement system
PSD	position sensitive detector
SEM	scanning electron microscope
SQUID	superconducting quantum interference device
T_c	Critical Temperature
TEM	transmission electron microscope
TGA	thermogravimetric analysis
TTMC	tetragonal transition metal chalcogenide
VASP	the Vienna Ab-initio Simulation Package
XRD	X-ray diffraction
ZFC	zero field-cooled

Chapter 1: Introduction

1.1 Iron-based superconductors - background and motivation

The discovery of superconductivity in 1911 by Heike Kamerlingh Onnes was, like many discoveries in science, a serendipitous event.[1] Onnes was conducting research on cryogenics in attempts to achieve temperatures in which helium would liquefy. Through the course of these experiment, he measured the resistance of mercury and observed a transition, called the critical temperature (T_c), from finite resistance to a seemingly zero resistance state at 4.2 K. This was the first measurement of the superconducting state of a material. Through continued work, it was determined that superconductivity is not just the observation of a zero resistance state. Magnetic measurements of samples in the superconducting state exhibited perfect diamagnetism as external magnetic flux was completely expelled - this phenomena was dubbed the Meissner effect after its founder.[2] Both of these phenomena have possible commercial applications. As to be expected, research in this new field exploded as zero resistance components or wires would completely revolutionize the world's electronic industry and electrical grid. The main hurdle the field has faced since its discovery is that the critical temperature at which most materials become superconducting is very low and thus requires expensive and complex cryogenic systems to achieve their respective superconducting states. However, research into syn-

thesis of new superconductors, fundamental properties and theory of superconductivity has continued to be topical for the past 100+ years.

The early work on superconductors encompassed work on a specific type of superconductor which would later be called “conventional" superconductors. The behavior of these materials could be extremely well by the microscopic theory of superconductivity described by Bardeen, Cooper and Schrieffer (BCS theory) which was awarded the Nobel Prize in 1972.[3] A formal description and work through of BSC theory can be found in many texts including the seminal textbook by Tinkham.[4] The key takeaways from the theory were the following: 1) electrons at the Fermi level under an attractive potential can form bound pairs called Cooper pairs,[5] 2) external magnetic fields decay exponentially inside of a superconductor,[6,7] 3) the critical temperature experiences an isotope effect,[8,9] and 4) the electron-electron coupling is mediated by phonons. The experimental work leading up to BCS theory and the culmination of a microscopic theory to describe the experimental observations exemplifies the amazing conjunction of experimental and theoretical work to describe the natural world. One problem which arose was the necessity of a phonon-mediated mechanism to describe superconductivity of these systems. This was assumed to set an upper-limit of critical temperature to the region of 30 - 50 K[10] for known systems as the time. The key requirements were that the material had to have a high density of states at the Fermi level (the system must be metallic), a high Debye frequency (lighter elements preferred) and strong electron-phonon coupling. Of course, these latter two are linked in most materials, thus the critical temperature “limit" of 30 - 50 K was imposed based on the currently known materials. However, it was later famously predicted that metallic hydrogen would be a room temperature superconductor[11]

which means the superconductivity in BCS theory does not have an actual limit - its just limited by the currently available materials. This conventional thinking regarding superconductors behaving in line with BCS theory was abruptly shook with the discovery of a new class of superconducting materials.

In 1986, Bednorz and Muller discovered superconductivity in Ba-La-Cu-O ceramic system at 30 K which kicked off the field of high-temperature or “unconventional" superconductors. They were awarded Nobel Prize in 1987 for their discovery. This work began an incredible amount of research activity around these new materials called the cuprate superconductors.[12–15] Two of the most important materials discovered through this research have critical temperatures above the limit of liquid nitrogen which significantly expanded the possibility of integrating these materials into commericialization. This is because liquid nitrogen cyrogenic systems are much cheaper and easier to manage than liquid helium systems. These two materials are $YBa_2Cu_3O_{7-x}$ (YBCO) which has a T_c= 93 K[16] and the other $Bi_2Sr_2Ca_{n-1}Cu_nO_{2n+4+x}$ (BSSCO) with a critical temperature up to 108 K[17] depending on which composition is measured. In general, all cuprate superconductors are built around the structural motif of Cu-O planes which consist of a checkerboard lattice of Cu^{2+} and O^{2-} ions which are separated by different spacers layers. The superconductivity in these systems comes from electrons within CuO_2 planes. The main differences between these materials and previous “conventional" superconductors are: 1) the undoped phases exhibit insulating and antiferromagnetic long range order before doping,[18] 2) upon both electron or hole-doping antiferromagnetic order is suppressed and superconductivity is induced which suggests electronic interactions rather than electron-phonon are responsible for superconductivity emergence, 3) the observed

superconducting gap is not isotropic[19,20] indicating non s-wave pairing. Although 30+ years have passed since their discovery, the mechanism which causes superconductivity in the cuprate systems is still not fully understood. Despite that, high temperature cuprate superconductors have begun to be integrated into commercial applications[21] and still offers a hot-bed of research activity.

The field of superconductivity was up-ended again with the discovery of another class of superconducting materials called the iron-based superconductors. The discovery of superconductivity in $LaO_{1-x}F_xFeAs$ in 2008 by Hosono *et al.* opened up an entire new field of study on superconducting materials containing iron pnictide or iron chalcogenide layers.[22] Historically, magnetism and superconductivity were considered antagonistic, which caused the excitement around the possibility of superconductors built out of the prototypical ferromagnetic element to explode. Ever since, there has been a fury of work done by chemists and physicists alike attempting to understand the mechanism(s) for superconductivity in this family of compounds through guided synthesis of analogous compounds offering different probes into the physical system.[23–27] The physics of the iron-based pnictide superconducting system is very similar to those of the cuprate superconductors whereby a high temperature antiferromagnetic state is suppressed upon doping to reveal superconductivity.[27,28] However, there are a number of key difference between the iron-based pnictide systems and the cuprates: 1) the undoped parent compounds are magnetic metals, 2) electronic correlations within the iron layers are moderate[29,30] in comparison to the strong correlation in the cuprate systems,[31] 3) the electronic structure in the cuprates is single band[32,33] and multi-band in the iron-based systems.[34–36] The combination of all these has made iron-based superconductors one of the most widely studied

topics in condensed matter physics in the past 10+ years.

The multiband nature of iron-based superconductors and the corresponding physics has been met with an abundance of theoretical work to describe the system. This has led to the coinage of the term “Hund metal" to describe the electronics structure and correlations in the system.[37] Unlike the single band nature of the cuprates and the description of Mott insulator physics leading to superconductivity,[31–33] the multiband nature of the iron-based system requires a new description. This “Hund metal" description is characterized by enhanced electron correlations, high spin configuration, and orbital character selectivity.[38,39] In summary, the correlations arise from local Coulomb interactions and Hund’s rules which allows another paradigm to access strong correlations in condensed matter systems. Hund’s rules is the energy scale which dictates intra-atomic exchange (i.e. lowering the cost of placing two electrons in different orbitals as opposed to in the same orbital). Thus, from theoretical approaches, it becomes clear the when the energy scale of Hund’s rules becomes meaningful, electronic correlations can become significant and give rise to very exotic physics, such as high temperature superconductivity.[40,41]

The iron-based and the cuprate superconducting systems both exhibit a similar structural motif whereby two-dimensional lattices are stacked to form layered materials. In the iron pnictide and chalcogenide systems, square iron layers are the basic building blocks of the iron-based superconductors which stack to form more complicated layered structures as shown in Figure 1.1. The largest structural difference between the pnictide and chalcogenide families is that the pnictide family is built of anionic $(\mathrm{Fe}Pn)^{-}$ (Pn = pnictide) layers whereas the chalcogenides are built from neutral $\mathrm{Fe}Ch$ (Ch = chalcogenide) layers. This means that the pnictide family requires cationic interlayer species to

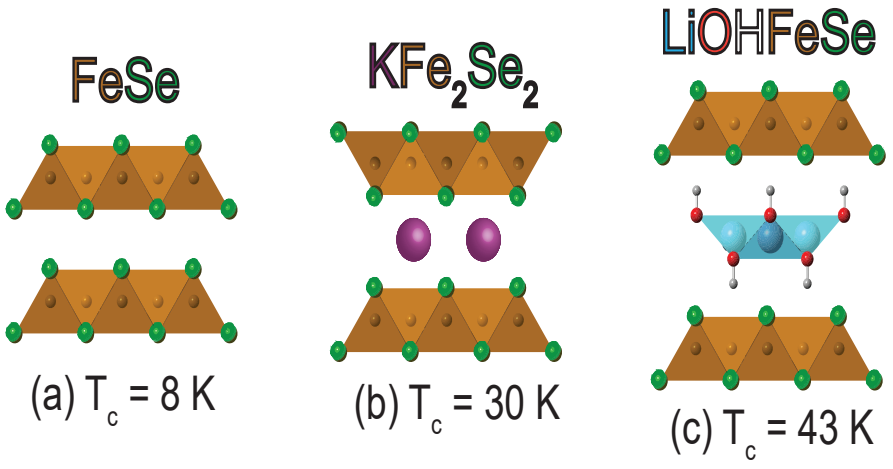

Fig. 1.1: Crystal structures of FeSe (left) and KFe_2Se_2 (center), and LiOHFeSe (right), and their respective critical temperatures, which all demonstrate the stacking of tetrahedral FeSe layers as the basic building block of the iron-based chalcogenide superconductors.

stabilize the structure, but the chalcogenide family can be made as a simple binary and expanded from that simple building block. The most structurally simple iron chalcogenide superconductor is FeSe which crystallizes in the anti-PbO structure (*P4/nmm*, Figure 1.1, left) and exhibits superconductivity at 8 K.[42–45] The T_c of FeSe can be improved significantly to 42-46 K from 8 K after intercalation,[46–48] 37 K with applied pressure[49] or 65 K in the monolayer limit.[50] Our group's research has focused on the chalcogenide family for two important reasons. To start, the neutral building block of FeSe and FeS layers is a perfect candidate for chemical manipulation through intercalation and doping due to its two-dimensional van der Waals structure and neutral charge. Also, unlike the related iron pnictide phases, FeSe is a superconductor without required doping and exhibits no parent magnetic phase.[42,51] Although no parent magnetically ordered phase exists, strong magnetic fluctuations have been observed in a wide range of temperatures in FeSe through neutron and NMR spectroscopy experiments.[51–54]

The use of FeSe as a building block (and the underlying structure-property relationships associated with the FeSe building block) and its subsequent chemical manipulation is the dominant motivation for the work described in this thesis. FeSe is the only tetrahedral transition metal chalcogenide material (TTMC), with the anti-PbO structure, that is known to be thermodynamically stable and can be synthesized through a number of methods, such as: direct elemental reaction and chemical vapor transport.[55–57] The FeS analogue is metastable and cannot be made through a traditional high temperature solid-state method. However, in 2015 a new hydrothermal synthetic scheme was devised to form FeS and found superconductivity at 4 K in powder samples.[58] More recently, another reaction scheme was devised to form single crystals of tetragonal FeS through topochemical de-intercalation of $K_xFe_{2-y}S_2$, which supported the previous work with FeS formed through this method exhibiting superconductivity at 4 K.[59] Thus, my work attempts to expand the class of TTMC materials beyond iron to understand how the TTMC structure leads to different properties for different electron filling and expand the chemical manipulations possible on the FeSe and FeS building blocks to tune the superconducting and magnetic properties of the iron-based chalcogenide superconducting family through topotactic synthetic routes.

1.2 Tetrahedral transition metal chalcogenides

The study of iron-based chalcogenide superconductors is motivated largely by their structure which is built upon neutral Fe*Ch* layers with a square transition metal sublattice; it is this fundamental structure that gives rise to the exotic physical phenomena observed

in these materials. Thus, it is useful to take a deeper look from a structural point of view to understand the nuances of the structure and bonding in this class of materials. the fundamental unit of tetrahedral transition metal chalcogenides (TTMCs) are edge-sharing MCh_4 (M = Fe, Co, Ni, Cu, Zn; Ch = S, Se, Te) tetrahedron which condense together in the plane to form extended two-dimensional layers of the MCh species. In the simplest case, these two-dimensional layers are then stacked together and held through van der Waals forces to form the anti-PbO type structure; to date only the iron and cobalt versions of these binaries have been synthesized.[60–62] This main building block highlights the most important features of this structure: 1) tetrahedral chalcogenide bonding of the transition metal, 2) square transition metal sublattice, and 3) neutral two-dimensional layers held together by van der Waals forces. A representative crystal structure illustrating the stacked layers held together by van der Waals forces, square metal sublattice, and tetrahedral coordination is shown in Figure 1.2. There are many different structures which use this building block or similar building blocks which can fall into the category of TTMCs which are cataloged in the review work by Zhou and Rodriguez,[63] but the remainder of the discussion will focus on the simple binary building block.

In a cubic close-packing arrangement of chalcogenide ions, there are tetrahedral and octahedral interstitial holes which can hold cations. In general, octahedral sites require the cation radius to be $> 41\%$ of the anion radius ($r_c/r_a = 0.414$) and tetrahedral sites requires the cation radius to be between 41% - 23% of the anion radius ($r_c/r_a = 0.225$). If we consider the sulfide S^{2-} anion which has an ionic radius of 1.84 Å, this means that cations with ionic radii between 0.75 - 0.42 Å may be able to order within the tetrahedral interstices. This means that larger transition metal cations are unlikely to be incorporated

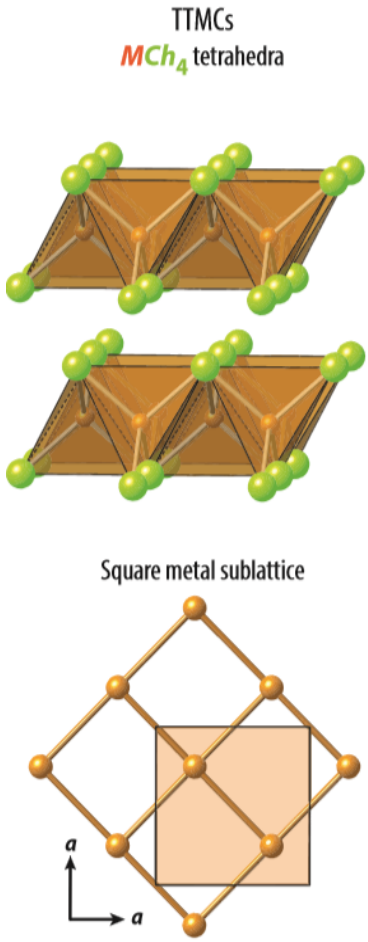

Fig. 1.2: Representative crystal structure of tetrahedral transition metal chalcogenides illustrating the stacked layers held together by van der Waals forces, square metal sublattice, and tetrahedral coordination adapted from Rodriguez.[63]

into this crystal structure. Another consideration must be taken into account as well due to the 2- charge on the sulfide ion. In order to maintain a neutral layer, which is key for our desired building block, a cationic charge is needed to yield a neutral metal chalcogenide layer. Since the *MCh* layers are only two layers of close-packed chalcogenide anions in the (AB)-(AB) sequence (the third layer C is empty in this structure), only one tetrahedral interstice exists which requires transition metal to be in a low valent 2+ cationic state. Thus, we can assume that low-valent transition metals with small cationic radii in the case of tetrahedral coordination will preferentially form this structural building block.

The tetrahedral bonding also leads to other benefits with regards to the electronic structure of the *MCh* layers themselves. The bonding between the transition metal and chalcogenide is covalent in nature and its impact is fully discussed in a some seminal works by Roald Hoffmann and more recently by our group.[63–65] The translation of the chemical bond's impact to electronic structure is very difficult as one is a real space concept while the other is best viewed in reciprocal space; fortunately two very important works have helped bridge that gap in thinking.[66,67] Another key feature, is that tetrahedral interstitial sites are closer together than octahedral sites within the cubic close packing array which means that interactions between the cations can be stronger and metal-metal bonding can be significant. This metal-metal bonding leads to a delocalized or wide-band description for the orbitals with character from the metal cations. Since the bands at the Fermi level are primarily metallic in character in these compounds,[63] the metal-metal interaction plays a significant role in determining the electronic structure and properties in these compounds.

Beyond the tetrahedral bonding of the transition metal, the square metallic sublattice itself is one of the main features of the TTMC class of materials. As previously stated, the metal-metal interactions caused by the proximity of the tetrahedral interstices in the cubic close packing of chalcogenide anions leads to bands with metallic character becoming delocalized and dispersed. The square metallic sublattice has been shown through a variety of works to be susceptible to electronic instabilities depending on electron filling.[68,69] These instabilities drive exotic physics and observable properties from charge density waves to superconductivity. Up until now, we have only considered the electronic effects of the transition metal sublattice, however; since the low-valent late

transition metals have unfilled *d*-orbitals, the effects of magnetism must be considered as well. To that end, there has been a significant amount of theoretical work on describing the magnetic interaction of the square lattice for configurations that would lead to magnetic frustration and possible exotic manetic ground states. This work has been done for local moment systems[70–74] and needs to be expanded to consider itinerant systems which includes metallic character with delocalized moments.

Finally, the last important piece of structural makeup of the TTMC class of materials is that the neutral *MCh* layers are held together by van der Waals forces which makes these materials perfect candidates for chemical manipulation. With FeSe and FeS displaying superconductivity at 8 K[42] and 4 K,[58] respectively, there has been substantial research on intercalation chemistry within the system to probe how intercalated species will affect the physical properties. This is because intercalating interlayer species can achieve two main goals: 1) increased interlayer spacing between adjacent *MCh* layers leads to increasingly two-dimensional electronic structure and 2) interlayer species can charge dope the *MCh* layers to tune the electron filling. Although the cobalt analogues to Fe*Ch* have been synthesized,[61,75] reported intercalation chemistry has been limited due to the phase stability of those compounds. Currently the list of successful intercalated species is fairly extensive including simple alkali metal cations,[76–78] which are typically able to be synthesized from a traditional solid state route such as self-flux or salt flux reactions. Other intercalates can be partially charged hydroxide or amine layers[46,79–86] that typically require low temperature or *chimie douce* techniques to synthesize. After these different intercalation schemes, the T_c of FeSe can be improved significantly to 43-46 K from 8 K. Although both hydroxide or amine intercalation can increase the T_c of FeSe,

only LiOH intercalation is known to increase the T_c of FeS from 4 to 8 K.[87]

Almost all of these intercalation chemistry methods are done at low temperatures and exploit the stability of chalcogenide anions in basic solution as well as the ability of basic aqueous and other basic solutions to oxidize iron metal to form soluble iron cations. As a note of caution: this chemistry must be done in basic conditions as acidic conditions may give rise to the evolution of toxic hydrogen chalcogenide gases. In any case, the means by which low temperature reaction schemes have been employed to modify TTMCs is the focus second main focus of this thesis work.

1.3 Topotactic chemistry and hydrothermal synthesis

The field of solid-state chemistry and physics is dominated by materials and synthetic routes which employ high temperatures in order to stabilize the formation of thermodynamically stable phases. This is for good reason, high temperatures typically allows for the formation of single crystals through dissolution of constituents in some flux and precipitation slowly through very precise temperature control. Single crystals are essential for in-depth physical property characterizations including resistivity, magnetic anisotropy, crystal structure determination, etc. Beyond that, traditional solid-state synthetic routes are often dubbed (often times with a negative connotation) “shake-and-bake" reactions for their ease of setup and lack of sophistication. In these reactions, mechanisms are typically not considered and there is often no control over the formation of intermediates. From a solid-state chemist’s point of view, this is in stark contrast to the organic chemist’s approach to the synthesis of a new compound or molecule. There, every step

of the reaction is considered and intermediates of complex reactions can be isolated and changed throughout the synthetic scheme to guide the reactions in new ways. The extension of a similar, albeit less dramatic, approach to the synthesis of solid-state materials offers a window into the synthesis of a wide-range of new compounds. Here, we consider the formation of metastable phases which are typically synthesized at low temperature as to limit the effects of thermodynamics and trap the desired metastable phases kinetically. Metastable phases are niche but are widely used for a variety of important applications.[88–91]

As mentioned, the stabilization of metastable phases is often done at low temperatures in order to avoid the effect of thermodynamics which will dictate the formation of the lowest energy phase if the thermodynamic energy barrier is overcome. However, temperature control is not the only tool we have to employ, we can also consider other chemical factors such as reaction time, pressure, concentrations, redox chemistry, etc. Thus, thinking about the synthesis of metastable phases can be approached by two ways: 1) changing the thermodynamic landscape of the chemical reaction by adjusting the chemical environment such as solvent, pH etc, or 2) using thermodynamically stable phases as a starting point to convert to metastable phases. As imagined, the approach of 1) can be extremely difficult and time-intensive as the number of variables which can be considered and adjusted in a reaction scheme is very large. This is not to say it can't be done, a great example of this is the synthesis of metastable tetragonal FeS, mackinawite, which can be done through a number of methods.[92–94] One caveat of this example is that mackinawite was known to exist from geological mineral samples, so a synthetic route could be rationalized from Mother Nature. In its mineral form, mackinawite is typically stabilized

by nickel impurities on the iron site and found in low temperature aqueous environments, such as marine sediments. However, in its synthetic form FeS is stabilized by a low temperature kinetically controlled route as to avoid the formation of more stable phases like gregite and pyrite.[92–94] Although mackinawite cannot be synthesized by direct solid-state reaction, it can be afforded using hydrothermal reaction under basic conditions. The compound itself converts to the more stable hexagonal phase when heated above 100 °C, but is stabilized above that temperature with high pH. This demonstrates that the thermodynamic landscape can be changed by tuning the synthetic environment. However, for the synthesis of materials which do not exists in nature, a successful synthetic route can, and often times is, be much more difficult to determine.

This brings us to 2), the conversion of one thermodynamically stable product to a metastable state through some chemical conversion method. This has been dubbed topotactic chemistry and is defined as a reaction scheme which retains some structural building blocks of the reactant in the product. Topotactic chemistry is essential in intercalation/de-intercalation/ion-exchange routes where a guest species is added, removed, or exchanged between host layers in order to tune the structure and physical properties. These reaction schemes often require low temperature and are often called *chimie douce* or “soft chemistry" routes in literature.[89,90,95–97] They are dubbed so as they offer a contrast to the high temperature approaches of traditional solid-state chemists. The field is not new and *chimie douce* reaction schemes have been used extensively in intercalation chemistry in the past 40 - 50 years to great effect.[98–103] With that being said, it is still considered a niche field as it straddles the fence between the worlds of the organic chemist and that of the solid-state chemist. The future outlook of topotactic chemistry and *chimie douce*

methods is very high especially with the current emphasis on rational material design as this synthetic paradigm allows for a guided design of extended solids - much like the thinking from the organic chemistry world.

When considering topotactic chemistry and *chimie douce* methods, the application to the work motivated in this thesis is readily apparent. As materials or solid-state chemists/physicists, we are intimately concerned with structure-property relationships - how does the crystal structure and bonding directly affect the manifestation of physical properties? The easiest example to consider is that of graphite and diamond, both made up of carbon but each have incredibly different properties due to structure and bonding within each material. We have already emphasized how TTMCs exhibit a structural motif for which we are interested: tetrahedral chalcogenide bonding to a transition metal, square transition metal sublattice, and van der Waals layers. Thus, this topotactic or *chimie douce* paradigm is an excellent lens to approach this problem. We are directly targeting one specific building blocks, and as such, we can use topotactic reaction schemes to change the overall structure without affecting that building block. All three chapters of this thesis utilize topotactic or *chimie douce* methods in order to synthesize new materials.

The chemistry of topotactic schemes can vary depending on the building blocks which are meant to be retained. For oxides and chalcogenides, a main tool for topotactic chemistry and *chimie douce* methods is the hydrothermal technique. Low temperature topotactic or*chimie douce* hydrothermal techniques can be used to synthesis a wide range of materials.[89,90,104–109] Hydrothermal reactions are used to mimic Nature's own hydrothermal reactions which exists at hydrothermal vents where typically insoluble minerals are heated in water by volcanic activity to dissolve before being released into sur-

rounding cold waters to form new species.[110,111] Due to the amazing chemistry present at these natural sites, there have also been intensely studied for their possible role in the origin of life.[112,113] In this research, hydrothermal conditions are defined as any reaction carried out above 100 °C and above 1 atm of pressure. Typical growths and reactions require the use of hydrothermal autoclaves which are used to maintain high temperature and pressure for the reaction media.

The theory of hydrothermal growth, the growth methods, equipment, growth parameters, etc are cataloged very well in the following sources;[114–117] we will focus on a brief discussion of how hydrothermal synthesis is done in this research and its relationship to topotactic chemistry and TTMCs. The low temperatures often used in hydrothermal reactions fits perfectly into the paradigm of topotactic chemistry for the synthesis of new TTMC materials. To reiterate, the low temperature allows for the stabilization of kinetic phases as thermodynamic effects are limited and phases for which kinetic pathways exists can be trapped and isolated. Another benefit of hydrothermal reactions is that the redox chemistry which occurs in water is highly desirable for chalcogenides, especially for iron chalcogenides. In particular, this is true for highly alkaline hydrothermal reactions. To that end, we can consult a Pourbaix diagram which shows which species will exist in solution as a function of pH and electrochemical potential. Pourbaix diagrams for any system are well tabulated but can be calculated from electrochemical potentials for all species which should exist in aqueous solution. An example Pourbaix diagram for the speciation of Fe in H_2O is shown in Figure 1.3.

From these Pourbaix diagrams, it is discovered that under reducing conditions at high pH, chalcogenide ions can be stabilized as HCh^- species which can act as the anion

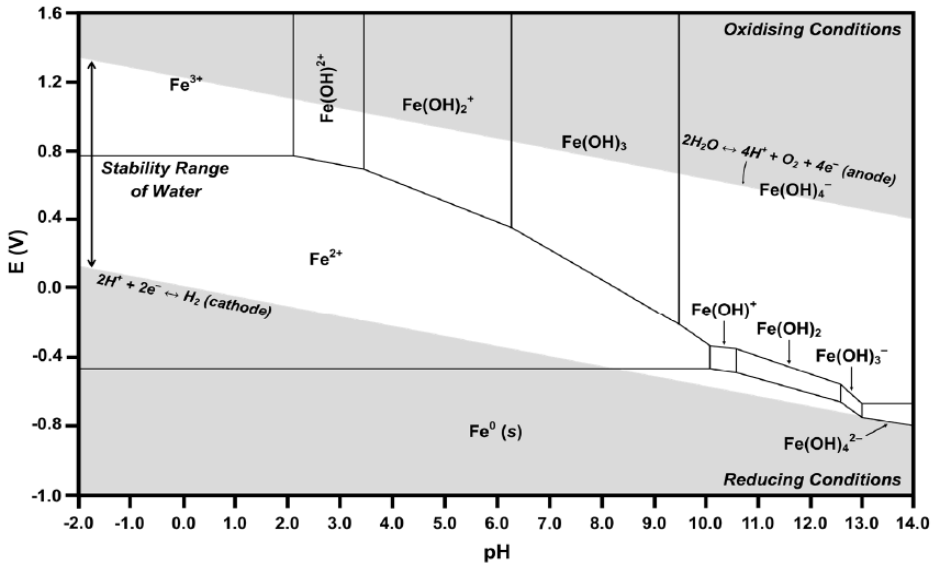

Fig. 1.3: Pourbaix diagram of iron calculated at standard temperature and pressure adapted from Channei.[118]

building block for the desired building block. For the cation, iron, the Pourbaix diagrams shows that iron oxidizes in reducing alkaline solution to yield Fe^{2+} species in solution. The combination of these two species in solution under reducing and high pH conditions has been shown to cause the formation of Fe-H*Ch*$^{-}$ clusters in aqueous and non-aqueous solutions with tetrahedral Fe-*Ch* coordination[119,120] which likely condense to form the extended layers in iron-based TTMCs. The special consideration in these reactions is that under anaerobic hydrothermal conditions, water plays the role of solvent and cathode for electrochemical reactions. In this case, we can consider the simple electrochemical reaction whereby iron powder is oxidized:

$$\mathrm{Fe(s) + 2\,OH^-(aq) \rightleftharpoons Fe(OH)_2(s) + 2\,e^-} \qquad E^\ominus = 0.89\ \mathrm{V} \tag{1.1}$$

$$\mathrm{2\,H_2O(l) + 2\,e^- \rightleftharpoons H_2(g) + 2\,OH^-(aq)} \qquad E^\ominus = -0.828\ \mathrm{V} \tag{1.2}$$

$$\mathrm{Fe(s) + 2\,H_2O(l) \rightleftharpoons Fe(OH)_2(s) + H_2(g)} \qquad E^\ominus = 0.062\ \mathrm{V} \tag{1.3}$$

This formulation shows that iron is oxidized in solution to form Fe^{2+} species with a small but positive driving force which can be increased as a function of temperature. This Fe^{2+} species then reacts with SH^- or SeH^- in solution to form the Fe-HCh^- clusters as the starting point for extended layers of iron chalcogenides. However, in the case where the SH^- or SeH^- species is not in solution, the Fe^{2+} species will all continue to oxidize to Fe^{3+} species.[121] Thus, we can push the reaction toward the formation of new products by utilizing the formation of the intermediate oxidized species. This harkens back to point 1) of how to stabilize metastable phases by changing the thermodynamic landscape of the chemical reaction by adjusting the chemical environment such as solvent, pH etc. The electrochemical considerations show that intermediate species can form due to redox potentials which can then be converted. As before, this is assuming the effects of thermodynamics are limited at low temperatures as thermodynamics will decide which phases forms at higher temperatures. Although this thesis focuses mainly on the topotactic approach to the formation of metastable phases, this other view point offers to bring another platform for future exploration. In particular, the exploitation of the associated hydrothermal redox chemistry with regards to the formation of desirable intermediate species that can be converted and trapped as metastable phases is underexplored.

1.4 Objectives and Outline

The previous sections have helped illustrate the motivation leading up to this thesis work. This work is highly interdisciplinary and lies directly in between the realms of solid state chemistry and condensed matter physics. In this thesis, we describe the synthesis and characterization of three different topotactically modified transition metal chalcogenide systems and their corresponding physical properties.

In Chapter 2, we discuss the synthetic techniques and characterization techniques employed throughout this work. In order to fully characterize crystal structure, elemental composition and physical/chemical properties, many different instruments and techniques were utilized.

Each Chapter 3-5 focuses on a different family of materials. In Chapter 3, we discuss the synthesis and characterization of tetragonal CoSe which is isostructural to superconducting FeSe. This material requires a topotactic de-intercalation synthetic route and we can successfully synthesize powders and single crystals. Physical property measurements displays metallic spin glass type behavior below 10 K which we attribute to magnetic frustration due to competing interactions of the square metal sublattice.

Chapter 4 focuses on the synthesis of transition metal doped (LiOH)FeSe. In previous work, (LiOH)FeSe was shown to display magnetic order below the superconducting critical temperature. We have used transition metal doping and a topotactic hydrothermal synthetic route to increase the magnetic signal of the system and have been able to observe the formation of long range magnetic order in nominally 20% Mn-doped (LiOH)FeSe. The majority of the work focuses on the characterization of this nominally 20% Mn-

doped sample family, however; we are able to synthesize other transition metal doped samples from Mn - Zn with varying results due to the chemistry and properties of the other transition metals.

In Chapter 5, we focus on synthesis and characterization of an ethylenediamine-intercalated iron chalcogenide family. This work echoes other work in the field on similar intercalation with one large difference. Other reaction schemes requires the addition of an alkali metal to the ethylenediamine neat solvent in order to stabilize the formation of the intercalated species. This has the detrimental effect of making the true doping level achieved by intercalation hard to identify due to the formation of other charged intercalated species with the alkali metal. Thus, we have developed a hydrothermal method which does not require the addition of an alkali metal to stabilize the intercalation of ethylenediamine into FeSe and FeS. This work shows that the hydrothermal method may be a more universal means to intercalate other adducts as it does not require liquid or low melting temperature adducts or the co-intercalation of alkali metals.

Chapter 6 summarizes the main findings of this work and discusses the future directions related to the work which can be explored.

Chapter 2: Methods

2.1 Synthetic Methods

The synthetic methods discussed here are more general with regards to the synthesis of a wide range of layered transition metal chalcogenides. More in-depth synthetic methods and discussion of those routes are cataloged in their respective chapters.

2.1.1 Self-flux synthesis of $ThCr_2Si_2$-type transition metal chalcogenides

The synthesis of single crystals of new intercalated and de-intercalated transition metal chalcogenides starts with the self-flux synthesis of the $ThCr_2Si_2$-type $K_xM_2Ch_2$ (M = Fe, Co, Ni; Ch = S, Se) single crystals. The main benefit of this approach is that many different compositions of the $ThCr_2Si_2$ exist even beyond chalcogenides and these phases can be usually be formed as relatively large single crystals. These single crystals offer a great base for post synthetic modification to form new layered transition metal chalcogenides.

A typical growth of $K_xM_2Ch_2$ (M = Fe, Co, Ni;Ch = S, Se) single crystals uses approximately 0.25 g K chunks and the required molar ratios of metal powder and chalco-

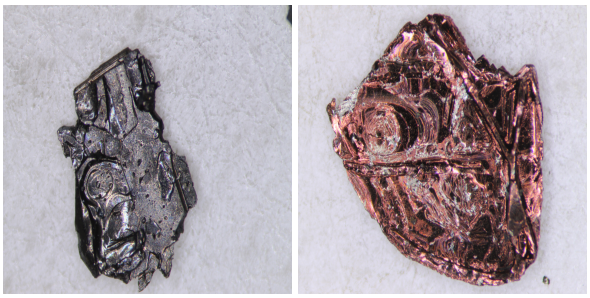

Fig. 2.1: As recovered single crystals of KCo_2Se_2 (left), KNi_2Se_2 (right) grown via the double ampoule method.

genide powder is calculated from the measured potassium amount. The amount of potassium has to be limited as potassium vapors attack the quartz tube which can cause them to break during the growth process. In general, this can be avoided if reaction vessels which are inert to alkali metal vapors such as niobium or tantalum tubes are used. The potassium, metal powders, and chalcogenide powders are loaded in a quartz ampoule within a inert atmosphere glovebox. As a note of safety, the reaction of potassium with chalcogenides can be extremely exothermic so these growths are usually done so that the loaded potassium does not come in contact with the chalcogenide powders. One way around this issue is to pre-react the transition metal and chalcogenide to form a stable binary; however, we have found that better quality single crystals are formed through a reaction of direct elements.

Once the reaction mixture has been removed from the glovebox, it is sealed under vacuum using a natural gas flame torch at a typical vacuum of $\sim 10^{-3}$ Torr. In the case of direct element reactions, the reaction mixture is usually frozen in liquid nitrogen before sealing to ensure that any possible reaction between the potassium and chalcogenides is limited. Once sealed, the smaller quartz ampoule is loaded inside a larger quartz ampoule and vacuum sealed again. This is done so that if the inner quartz ampoule breaks due to

potassium vapor attack or other factors, the reaction mixture is not fully compromised; inner quartz tube failure occurs in about 20% of growths. These double-sealed quartz ampoule reaction mixtures are loaded into a box furnace, heated to 1050 °C at a rate of 10 °C/hr and held at 1050 °C for 12 hours to ensure reaction homogeneity. The very slow heating is done to ensure the melting of potassium occurs slowly to react with the chalcogenide to form a potassium polychalcogenide flux. As the reaction slowly heats the potassium polychalcogenide flux react with the transition metal to form the $K_xM_2Ch_2$ (M = Fe, Co, Ni; Ch = S, Se) product as the potassium polychalcogenide flux oxidizes the transition metal.

The reaction mixture is slow cooled from 1050 °C to 550 °C at a rate of 2 °C/hr which assures slow crystallization. Once 550 °C is reached, the reaction mixture is cooled the room temperature naturally by turning off the furnace. These crystals are typically recovered in air but is done in an inert gas glovebox when required. Crystals are typically 5 x 5 x 0.5 mm platelike shiny crystals of different colors depending on what transition metal was used in the reaction mixture shown in Figure 2.1. The crystals are usually air stable on the order of a day or so but are stored in an inert gas atmosphere for long term storage.

2.1.2 Soft chemical reductive de-intercalation

The class of materials of tetrahedral transition metal chalcogenides with the described layered structure was previously limited to the FeSe. This is because the layered structure is not thermodynamically stable for other combinations of transition metal

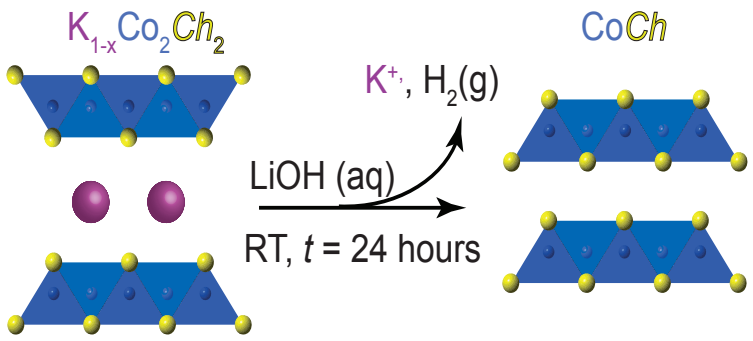

Fig. 2.2: Soft chemical reductive de-intercalation at room temperature in saturated LiOH solution of KCo_2Ch_2 single crystals and powders to form CoCh powders and single crystals.

and chalcogenides, even for FeS. Previous work in our group showed that single crystals of FeS would be synthesized by hydrothermal reductive de-intercalation of KFe_2S_2 single crystals to form FeS single crystals.[59] Similar work had also been attempted to de-intercalate the KNi_2Se_2 compound to form the layered NiSe binary, isotructural to FeSe, but was not successful.[122] My work has expanded the available TTMC's beyond FeSe and FeS to the isostructural cobalt analogues.[61]

Two methods are used to form layered tetragonal Co*Ch* (*Ch* = S and Se) compounds shown in Figure 2.2. KCo_2Ch_2 powders and/or single crystals were placed in approximately 10 mL of saturated LiOH solution made by dissolving $LiOH{\cdot}H_2O$ in de-ionized water. The reaction mixture was purged with argon and placed in an ultrasonic bath for an hour. The reaction mixture was then recovered via centrifuge and washed up to five times with water and ethanol which yielded black shiny powders of Co*Ch*. Another method was employed to ensure starting crystals of KCo_2Se_2 were not destroyed in the ultrasonic method; at the current time single crystals of KCo_2S_2 could not be made. Single crystals

of KCo_2Se_2 were placed in 20 mL saturated LiOH solution in a round-bottom flask on a Schlenk line under inert gas flow for 1 day. Shiny silver crystals were recovered after 1 day after water and ethanol washes and dried under vacuum. In these reaction scheme one important note of safety must be acknowledged. Highly basic solutions must be used for chalcogenide reactions in water in order to prevent the formation of highly toxic H_2S and H_2Se gases.

This room temperature reductive de-intercalation was found to work for the cobalt analogue whereas the iron versions, FeSe and FeS, requires hydrothermal conditions to achieve the de-intercalation. Preliminary attempts with the cobalt system under hydrothermal conditions gave different polymorphs depending on the temperature used.[61] Some work has been done to employ room temperature and hydrothermal schemes to the KNi_2Ch_2 system to form NiSe, isostructural to FeSe, with no success. It has been found that room temperature reactions in saturated basic solutions leave the starting KNi_2Ch_2 unreacted and higher temperature achieved in hydrothermal reactions give different NiCh polymorphs. The expansion of soft chemical techniques to expand the TTMC class of materials is promising avenure for future research.

2.1.3 Hydrothermal ion exchange

Much like the soft chemical reductive de-intercalation reaction scheme, we can also expand the synthetic routes to include ion exchange starting with the $K_xM_2Ch_2$ (M = Fe, Co, Ni; Ch = S, Se) single crystals from the self-flux synthesis. As a note, for some desired products, it is possible to complete a two-step reaction whereby the $K_xM_2Ch_2$

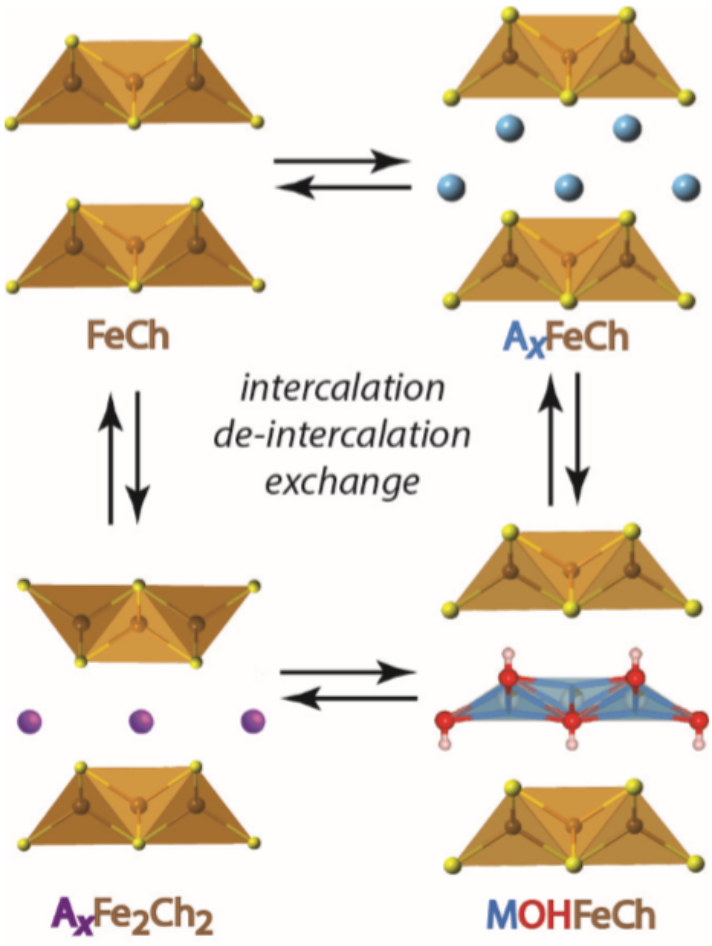

Fig. 2.3: Possible hydrothermal cation exchange routes for iron chalcogenides which includes the intercalation of extended hydroxide layers and various cations.[123]

crystals are de-intercalated and then intercalated with another species, but this does not work for all desired intercalants. A summary of possible reaction schemes is shown in Figure 2.3

With regards to our research, the predominate use of this reaction scheme is for the synthesis of single crystals of the $(Li_{1-x}Fe_xOH)FeSe$. In this compound, FeSe layers are intercalated with an extended hydroxide layer of LiOH. It has been found through multiple works that some of the Li in the LiOH layers is substituted with Fe which gives the LiOH layer a partial positive charge. This partial positive charge helps stabilize the inter-

calation as well as charge doping the FeSe layers - increasing the superconducting critical temperature to 45 K from 8 K in FeSe.[48,79,82,124] This compound can also be made from a “bottom-up" route whereby Fe metal and a selenium source are added to a hydrothermal autoclave with excess LiOH to build the FeSe layers in the reaction although this reaction scheme only yields powders.

To remedy this, we have developed a hydrothermal cation exchange method to start with single crystals of $K_xM_2Ch_2$ and exchange the interlayer potassium ions for LiOH. The extreme benefit of this reaction scheme is that single crystals of $(Li_{1-x}Fe_xOH)FeSe$ are afforded which enables much for expansive physical property characterization. In a typical synthesis, selected single crystals of $K_xM_2Ch_2$ are added to 15 mmols Fe granules/powders, 1.2 mmol selenourea, 1.2 mmol tin granules, 0.30 moles LiOH, and 40 mL H_2O or D_2O (required for neutron experiments). All components were added to a Teflon cup and the head space was purged with argon for 2 minutes before being tightly sealed. The autoclave was placed into an oven for 72 hrs at 120 °C before being recovered in air and dried under vacuum.

The addition of additional Fe granules/powders and selenourea in the reaction scheme is to ensure the product is not selenium or iron deficient. Often time, the starting $K_xM_2Ch_2$ crystals are iron deficient;[125] thus the addition of extra Fe ions in solution acts to replace vacancies as superconductivity in these compound is very dependent on stoichiometry. Single crystals produced from the self-flux method $K_xM_2Ch_2$ are frequently on the size 3 x 3 mm^2 or larger and the thickness can be controlled by cleaving from the growth boule. After the hydrothermal cation exchange it is often noted that the starting crystals will have flaked apart to form much thinner crystals. This method is used heavily for the

production of very high quality ($Li_{1-x}Fe_xOH$)FeSe single crystals, but can be expanded for the intercalation of other species are future work.

2.1.4 Alkali metal-free ethylenediamine intercalation of iron chalcogenides

The previously mentioned “bottom-up" synthetic route has the downside of only producing powders, but the large benefit is that the ability to synthesis new compounds is more robust. This is attributed to the fact that instead of actively having to exchange one cation for another, as in the hydrothermal cation exchange method, Fe*Ch* layers are built $in-situ$ from Fe and a chalcogenide source which form around the desired intercalated species. This allows the intercalation of much larger species between the Fe*Ch* layers. One such growth is the hydrothermal intercalation of Fe*Ch* with ethylenediamine. This reaction can be done starting with pre-reacted tetragonal Fe*Ch*, but that reaction scheme must be done solvothermally which limits desired intercalate adducts to ones that have melting points in the low temperature regime. Thus, we have developed a hydrothermal route whereby the desired adduct, ethylenediamine in this case, is mixed with water and other constituents to form the intercalated species. Again, the benefit of this scheme is its generality, where by many adducts which are miscible or soluble in water can be used as possible intercalants.

For a typical growth, 4 mmol of Fe powder, 10 mmol thiourea or 5 mmol selenourea, 7 mmols KOH, 10 mL H_2O and 3 mL ethylenediamine were added to a Teflon cup, purged with argon for 2-5 minutes and sealed in a hydrothermal autoclave. The reac-

tion mixture was placed in a convection oven for 2- 6 days at 120 - 160 °C before recovery via centrifuge in air and drying under vacuum. The recovery of this reaction yielded shiny black powders and excess unreacted Fe granules or powders could easily be removed via magnet.

The benefits of this reaction scheme are twofold: 1) the $in-situ$ formation of FeCh layers should allow for a wider range of intercalated species and is the only way to synthesize the intercalated species of the metastable sulfide analogue, 2) the addition of water allows for a wider range of intercalated adducts as long as the adduct is miscible or soluble in water. The extension of this work to include other adducts is a promising avenue for future work.

2.2 Characterization Methods

Synthesis of new compounds takes the bulk of one's research time as it can take many, many trials to achieve success in forming new compounds. However, the most important steps come next in the characterization of the structure and properties of the synthesized compounds. This section details the numerous methods used in this thesis for structure determination, elemental composition, physical property measurements, and theoretical calculations. Each section catalogues typical usage and important notes. Technical and theoretical references are added to each section for more in-depth reading as required.

2.2.1 Laboratory powder x-ray diffraction

The X-ray Crystallographic Center at the University of Maryland is extremely well-equipped for research activity and Dr. Peter Zavalij has been incredibly helpful in discussion and helping conduct various x-ray experiments. As recovered samples were ground in a mortar and pestle for approximately 10 minutes until the sample crystallite size was uniform and grinding yielded smooth motion. Since our growths are usually small in recoverable product, the ground powders were typically mounted on a very small or flat sample plate and pressed down with a glass slide to ensure the surface as flat. Powder x-ray diffraction measurements for quick phase identification were done on a Bruker D8 X-ray diffractometer with Cu Kα radiation (λ = 1.5406Å) in Bragg-Brentano geometry from 5° - 90° 2θ with a step-size of 0.020° and total counting time of 20 minutes. Extended measurements for Rietveld analysis were altered to a step-size of 0.010° and a total counting time of 1 - 3 hours depending on how much powder was available for the measurement.

All crystallographic analysis was done using the Bruker software suite. Bruker Diffrac.EVA was used for analyzing collected diffraction patterns and often times for quick search-and-match phase identifications to quickly identify all phase (products and impurities) in a reaction mixture. Bruker Diffrac.Suite TOPAS was used for all Lebail/Pawley and Rietveld refinements.[126,127] Laboratory x-ray diffraction and subsequent Rietveld refinement was usually paired with synchrotron x-ray diffraction, neutron powder diffraction, electron diffraction and/or other elemental analysis techniques to fully understand the crystal structure and chemical composition.

The most frequently used references for x-ray diffraction and Rietveld refinements are collected here.[128] The website curated by John Evans at Durham University is tremendous is explaining usage of TOPAS for all types of x-ray and neutron refinements, peak indexing, and more complex techniques (`http://community.dur.ac.uk/john.evans/topas_academic/topas_main.htm`). Crystallographic databases were often time extremely useful to identify new compounds via similar structural motifs and/or by matching catalogued data - the ones most frequently used for the Inorganic Crystal Structure Database (ICSD) (`https://icsd.fiz-karlsruhe.de/index.xhtml;jsessionid=AA35F9A5641C059D4D0AA0C29791ACC2`) and the Cambridge Structural Database (CSD) (`https://www.ccdc.cam.ac.uk/structures/`). The ICSD is most widely used in inorganic research, but the CSD adds the ability to search for organic, organometallic, and organic-inorganic hybrid compounds.

2.2.2 Synchrotron powder x-ray diffraction

In many cases, we used synchrotron x-ray diffraction techniques to supplemental in-house laboratory x-ray diffraction. For work in this thesis, the mail-in program at 11-BM at the Argonne National Laboratory Advanced Photon Source was used exclusively, however; our group has done a series of experiments at 17-BM at Argonne National Laboratory Advanced Photon Source for *in – situ* x-ray diffraction of hydrothermal reactions. The mail-in program offers access to the 11-BM instrument which offers the highest resolution powder diffraction instrumentation in the Americas ($< 1.4 \times 10^{-4}$ $\Delta Q/Q$) with extremely fast collection times (< 1 hour collection). The constant wavelength from the

synchrotron beam is determined by the beamline cycle, typically between 15 - 30 keV. Diffraction data is collected from 1° to 45° 2θ with a step size of 0.001° and total collection time of about 1 hour.

Synchrotron x-ray diffraction allows for higher resolution x-ray diffraction patterns which aids in the analysis of crystallographic structure and elemental composition. This is especially true in complex systems with complicated crystal structures or high amounts of disorder with regards to elemental composition. The wesbite for 11-BM is quite useful in describing how to obtain mail-in time as well as user guidance for sample preparation and experimental questions (`https://11bm.xray.aps.anl.gov/users.html`).

2.2.3 Neutron powder x-ray diffraction

Neutron powder diffraction is a very powerful complementary technique to x-ray powder diffraction for two main reasons. To start, neutrons are used instead of x-rays which means since neutrons have a magnetic moment, the magnetic order of your sample may be determined as well as the crystallographic structure. Secondly, the x-ray scattering form factor scales with number of electrons so elements close to each other on the periodic table are hard to identify whereas neutron scattering is determined by the nucleus of the scattering atom which may be appreciably different for nearby elements and especially useful for light elements.

One important note about neutron diffraction is that neutron flux is much less than typical x-ray flux. For example, a neutron flux of 1.1 $\times 10^6$ n/s/cm^2 is achievable at BT-1 at the NIST Center for Neutron Research (NCNR) whereas the flux on the sample

at a synchrotron x-ray source 5 $\times 10^{11}$ p/s/mm^2, many orders of magnitude larger. For neutron diffraction experiments, this means two things: 1) more sample is often required for neutron powder diffraction (> 1g pure sample) and 2) longer collection times are required to obtain desirable statistics.

The research cataloged here has made use of three different instruments for neutron powder diffraction. The main instrument used was BT-1 and the NCNR with help and collaboration with Dr. Craig Brown. BT-1 is a instrument designed specifically for high-resolution neutron powder diffraction. Ground powder samples were loaded in vanadium cans in a helium glovebox and sealed with pressed indium wire. The use of vanadium can is important as vanadium nuclei has a very small coherent scattering length and is essentially transparent to incoming neutrons. Helium is used when low temperature experiments are required to avoid freezing other gases. Loaded vanadium cans were typically mounted on closed-cycle refrigerators (CCRs) and cooled to base temperature, usually about 3 - 6 K.

Diffraction measurements were conducted using either a Ge(311) monochromator (λ = 2.0709 Å) or Cu(311) monochromator (λ = 1.540 Å) depending on the desired outcome of experiment. The Ge(311) monochromator offers the highest total flux on the sample which is often needed if the total amount of sample is small and it has the best resolution at low angles which may be required for crystal structures with large units cells and for magnetic phase identification. Cu(311) is a more universal choice with high resolution at all angles. A typical diffraction pattern is measured from 15° to 145° 2θ with a step size of 0.05° at multiple temperature, typically above and below the observed magnetic transition temperature from other experimental methods. Col-

lection times have varied depending on the amount of sample but average 8-10 hours at each temperature. The BT-1 website has a lot of useful information regarding instrument capabilities and how to acquire beamtime (https://www.nist.gov/ncnr/high-resolution-powder-diffractometer-bt-1).

Additional neutron powder diffraction experiments were conducted at BT-7 at the NCNR. This research was done in collaboration with Dr. Jeffery Lynn and his team at BT-7. BT-7 is a triple-axis spectrometer which is typically used for inelastic neutron spectroscopy. However, the instrument at BT-7 has a position sensitive dectector system (PSD) which is available for use as needed. On the typical setup at BT-7, a point detector is used which would make the collection of diffraction patterns very time-consuming. The PSD setup allows a 5° 2θ range to be collected at once which is very useful for diffraction patterns of one or more diffraction peaks in close proximity. The setup here is very similar to BT-1 where ground powders were loaded in a vanadium can under helium atmosphere and cooled to base temperature on a CCR. In the case of the transition metal doped (LiOH)FeSe work, one diffraction peak in question was measured as a function of changing the temperature on the CCR setup. For this, the sample was cooled to the desired temperature and a diffraction pattern using the 5° 2θ range of the PSD was collected for approximately 1 hour using a pyrolytic graphite monochromator (λ = 2.359 Å) at each temperature. The BT-7 website has more information regarding the more traditional use of the triple-axis instrument for inelastic measurements (https://www.ncnr.nist.gov/instruments/bt7_new/).

Finally, additional neutron powder diffraction measurements were completed at Oak Ridge National Lab High Flux Isotope Reactor (HFIR) at the HB-2A instrument.

This work was done in collaboration with Dr. Simon A.J. Kimber and Dr. Keith Taddei. The sample setup and experiment at HB-2A is very similar to BT-1. Powder samples were loaded in vanadium cans and sealed under He atmosphere. The sample environment at HB-2A uses a multiple sample changer and an open ILL orange cryostat which requires frequent refills of liquid nitrogen, but the multiple sample changer enables less sample changes. HB-2A uses a Ge(115) monochromator (λ = 1.54Å) and has higher flux at the sample than BT-1 so typical collection times were approximately 2 hours so more samples can be scanned during experimental time. The HB-2A website catalogs the instruments capabilities, how to request time on the instrument, and how diffraction data is obtained, manipulated and analyzed (`https://neutrons.ornl.gov/powder`).

Neutron powder diffraction is very useful but much different with regards to magnetic diffraction and experimental setup than x-ray diffraction. Since neutron production usually requires a nuclear reaction as at NCNR and HFIR, neutron experiments are only done at national facilities which require proposals, approval and training. The most used references for neutron diffraction were the beamline website as well as the texts listed here.[129,130]

2.2.4 DC magnetic susceptibility and magnetization

Magnetic susceptibility is a measure of a materials response to an external field. These measurements are done on both single crystals and powder samples. Powder samples are typically loaded in a gel capsule, which has very small parasitic magnetic background, and then loaded into a straw to fit onto the sample holder on the instrument. The

straw has very minimal background signal as well which can be measured separately and subtracted from the sample measurements in the case that the straw signal is contaminating the signal of the material. Single crystal samples are typically mounted on a quartz paddle or brass rod which both offer very minimal background. Single crystal measurements must be carefully planned as to measure the sample along desired crystallographic axes as the magnetic field in the instruments are fixed with regards to direction. Magnetic susceptibility of the sample is determined by applying a known excitation field and measuring the magnetization through different techniques. Magnetic susceptibility per unit volume is defined as: $\chi = \frac{\mu_0 M}{B}$, where M is the magnetization of the sample, and B is the macroscopic magnetic field intensity, χ itself is a dimensionless quantity. Magnetic susceptibility can be converted to a molar quantity if the mass, molar mass and magnetic ions per unit cell is known.

DC magnetization is used to observe two different phenomena in a sample. Typically, the first experiment done is a measure of the temperature dependent magnetic susceptibility. This is used to determine if the sample undergoes any magnetic phase transition at a certain temperature which can be used to identify what type of magnetic order exists in the sample. This experiment consists of the collection of two temperature sweeps at the same applied field. The first is called the zero field cooled (ZFC) curve, where the sample is cooled without any applied field down to base temperature. Once base temperature is reached, an applied excitation field is applied and then the magnetization of the sample is measured as the temperature is heated to room temperature. For the second curve, field cooled (FC) magnetization data is collected from room temperature as the system is cooled to base temperature. The difference between ZFC and FC curves

is that in the ZFC curve the sample is allowed to cool down to base temperature without an external applied field and the sample's magnetization will align based on its own energetics. However, in the FC curve, the directionality of the applied field in the instrument will cause the sample's magnetization to align with the applied field.

This is very important to understand ferromagnetic, ferrimagnetic and antiferromagnetic ordering. In ferromagnetic order, at some critical temperature called the Curie temperature, the magnetic spins in the sample will all co-align. So, in the ZFC curve the magnitude of magnetization below the transition temperature will be different than in the FC mode. This depends on the strength of the applied excitation field in proportion to the internal field generated by the alignment of the spins. In a strong ferromagnetic material, the ZFC and FC mode will clearly and abruptly bifurcate at the transition temperature. In an antiferromagnetic or ferrimagnetic material, the spins will anti-align at a transition temperature called the Neél temperature. Antiferromagnetic and ferrimagnetic order can exist with many different possible arrangements and are often very difficult to solve the magnetic ordering structure. Ferrimagnetic ordering is similar to antiferromagnetic but instead of perfect anti-alignment, one set of spins will be weaker than the other. In these classes of materials, since the spins are anti-aligned and the net moment is zero or very low, the bifurcation of the ZFC and FC curves is very weak or non-existent. This type of measurement can help determine the magnetic ordering of the system.[131,132]

Superconductivity exhibits distinct behavior in the temperature dependent magnetic susceptibility curve. In the introduction, we discussed how superconductors exhibit the Meissner effect which is the exhibition of perfect diamagnetic behavior. Thus, in magnetic susceptibility, a transition to diamagnetic behavior is observed at the superconducting

critical temperature. As a note, for superconductors, magnetic susceptibility is typically reported as dimensionless ($4\pi\chi$) which requires that the density of the sample is known which is typically determined from Rietveld refinements. The use of ($4\pi\chi$) is done to show the shielding fraction of the sample at base temperature of the superconducting material as a perfect diamagnetic signal will yield a value of -1 at the measured temperature. In this scale, shielding fraction is just the percentage of the ($4\pi\chi$) value from 0 to -1. This is used to determine if the sample is a bulk superconductor, which should show high shielding fraction, or filamentary, which typically shows very low shielding fraction. The behavior of magnetic susceptibility of superconductors can be very complex and a more detailed description can be found here.[4]

The other experiment usually performed is called isothermal magnetization. In this experiment, the magnetization of the sample is measured at fixed temperature as a function of applied field up to the max field available on the instrument. This is also very useful for determining the magnetic order of the system. Ferromagnetic systems, and sometimes ferrimagnetic systems, with a net moment can exhibit magnetic hysteresis as the field is sweeped where the measured magnetization depends on the magnetic history of the sample. Antiferromagnetic materials do not exhibit this behavior in the simplest case. When considering superconductors, they exhibit Meissner shielding up to a certain field, called the upper critical field, where the magnetization becomes non-zero. Isothermal magnetization curves are typically performed at many temperature, above and below the magnetic transition temperature in order to understand how the ordering and behavior changes with temperature.[4,131,132]

Throughout my work, DC magnetic susceptibility was measured by two different

techniques: 1) superconducting quantum interference device (SQUID) magnetometry and vibrating sample magnetometry (VSM). SQUID magnetometry measurements were completed on two instruments, Quantum Design MPMS-XL and MPMS3, both of which are equipped with a 7 T magnet. SQUID magnetometry is the most widely used technique because it is incredibly sensitive to small magnetic fields on the order of 10^{-8} - 10^{-9} emu.[133] In this technique, the sample is moved through a SQUID device which is two connected branches of Josephson junctions which form a closed loop. As the magnetized sample moves through the SQUID loop, the magnetic flux inside the loop changes so that the voltage across the SQUID loop will begin to change depending on the magnetic flux. The change in voltage is measured as a function of sample position inside the sample space which is then converted to magnetization by converting the measured voltage across the SQUID coil into magnetization. This is a simplified explanation and more in-depth references can be found here.[133–135]

The other technique used is VSM. VSM is typically used in our labs when higher fields are required as the VSM option is accessible of the Dynacool system which is equipped with a 14 T magnet. The use of a stronger external magnet can be needed in some systems with high superconducting upper critical fields or in systems with interesting magnetic ordering at higher fields. The one downside of VSM usage is that the VSM is less sensitive and usually on the order of 10^{-5} emu.[136] The VSM technique uses Faraday's law of induction to measure the magnetization of the sample. The sample is placed inside a conducting coil, a magnetic field is applied to the sample, and the sample is then oscillated inside the conducting coil. If the sample is magnetized by the applied magnetic field, the oscillating sample will cause swiftly changing flux within the coil which

will then induce a AC voltage through the coil. The amplitude of the induced voltage is directly proportional to the magnetization of the sample.

2.2.5 AC magnetic susceptibility

AC magnetic susceptibility is very similar to VSM measurements except that instead of oscillating the sample through a conducting coil, a oscillating magnetic field is applied to the sample. Since the applied excitation field is oscillatory, this will induce an oscillatory voltage in the pick-up coil of the AC measurement. The big difference between the VSM measurement and the AC magnetic susceptibility measurement is that the induced AC voltage in the AC magnetic susceptibility measurement comes from the changing magnetization of the sample due to the applied field. This means that the time dynamics of the induced voltage are intrinsic to the system and describe the time dynamics of the magnetization in the sample.

This is very useful in the study of systems where the magnetization changes in time. This is true in spin glass systems, ferromagnetic domain formation and even superconductors inside the superconducting state.[4,137–139] In our lab, the AC magnetic susceptibility is performed on the Quantum Design PPMS 14 T.[140] The measurement can be done on powders or single crystals. Typically, powders are loaded into a Teflon bucket with an attached sample rod which seal the bucket and fits into the pick-up and drive coils which are all then loaded into the PPMS system for atmosphere and temperature control. With this setup, the lowest achievable temperature is 1.8 K on the PPMS 14 T, but members of Dr. Johnpierre Paglione's group have designed and implemented many AC magnetic

susceptibility instruments for use in systems below 1.8 K in the milliKelvin regime.

2.2.6 Longitudinal electrical resistivity

Longitudinal electrical resistivity is a useful technique for the measurement of the electronic properties of a material especially down to low temperature. Electrical resistivity measurements were performed on Quantum Design PPMS 9 T, PPMS 14 T and Dynacool 14 T systems. For a typical measurement, single crystals of the material were wired up by attaching four gold wires with DuPont 4929N silver paste. The DuPont 4929N silver paste must be mixed with a small amount of 2-butoxylethyl acetate in order to dissolve the silver paste in such a way that it is workable for wiring up the sample. The four wire setup is used to eliminate the contamination of wire resistance, although gold wire is very low, as well as contact resistances from the silver paste connection to the sample. In this setup, a known current is applied to the two outer wires and then voltage in measured across the two inner wires as shown in Figure 2.4. In this case, no current should pass through voltage wires and thus the voltage measured across the two voltage terminals should only be dependent on the material itself.

Thus, longitudinal resistance can be determined by the measured voltage across the voltage lead since the applied current is known. This is then converted to resistivity, which is intrinsic to the sample and does not depend on the sample size, by dividing out geometrical components. $\rho_{xx} = R_{xx} \cdot \frac{tw}{l} = \frac{V_{xx}}{I} \cdot \frac{tw}{l}$. Here, ρ_{xx} describes the longitudinal resistivity along the x-direction which can be changed as long as the crystallographic axes are well-known, R_{xx} describes the resistance along the x-direction, t, w, l are geometric

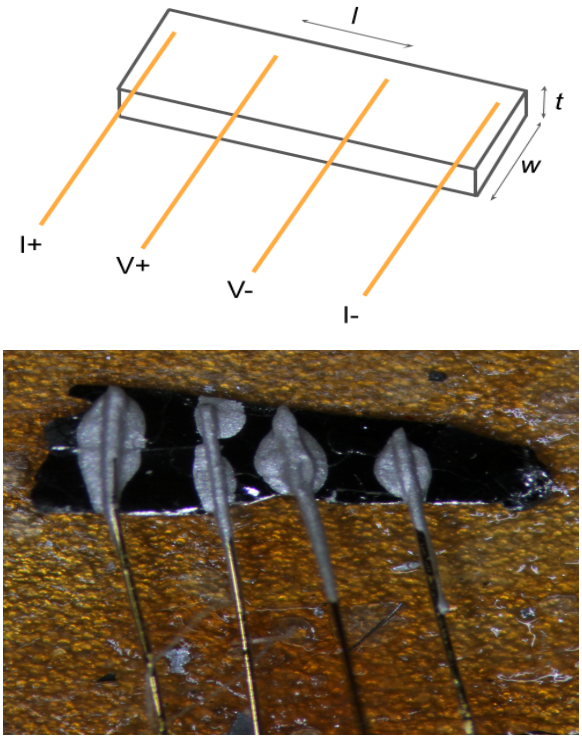

Fig. 2.4: Schematic representation of longitudinal resistivity measurement technique and example of wired CoSe single crystal on the PPMS DC puck.

parameters of the crystal which are typically measured using a microscope and attached camera, and V_{xx} is the measured voltage across the voltage leads in the x-direction. The samples are typically wired and then the other ends of the wires are attached to solder pads on the Quantum Design PPMS DC resistivity pucks. The puck is then loaded in the PPMS 9 T, PPMS 14 T, or Dynacool 14 T and resistivity is measured as both a function of temperature and field.

Measurements done as a function of temperature are done to determine phase transitions which may occur at low temperature such as a superconducting transition or the onset of a charge density wave. Measurements done as a function of field, called magnetoresistance, are done in a similar vain to understand how the material behaves at high

magnetic field, such as the suppression of a superconducting transition. A systematic study of resistivity in materials can be found here.[134,141]

One key caveat to longitudinal resistivity measurements is that it is not a bulk characterization technique. Electrical transport will occur on the path of least resistance which means the sample technique as a whole is highly susceptible to sample inhomogenity and other confounding effects. This means that a result from a single experiment may be misleading. To that end, electrical resistivity measurements are always done in at least triplicate on the same sample or from the same sample batch. If interesting phenomena is observed in resistivity measurements, these are always corroborated with a bulk characterization technique such as magnetic susceptibility or heat capacity measurements.

2.2.7 Low temperature specific heat

As mentioned, electrical resistivity measurements are often paired with specific heat measurements in order to match observed phenomena. Specific heat is a bulk characterization technique which relates a known heat applied to a material to the resulting change of temperature of the material itself. Because the specific heat is related to the change in entropy of a material with respect to temperature, specific heat measurements are susceptible to any change in entropy of the system. Specific heat was measured on single crystals and pressed powders of samples on the PPMS 14 T system[142] using the two-tau technique.[143]

In this technique, the sample is placed atop a heating platform which is specially designed by Quantum Design on top of a traditional measurement puck. The sample

is placed onto the heating platform with low temperature Apiezon N grease to allow optimal thermal contact between the sample and the heating platform. The sample puck is then loaded into the PPMS 14 T which is set to high vaccum ($< 10^{-4}$ Torr) which is required for heat capacity measurements as the sample must be as thermally isolated from the environment as possible. For the measurement, a known constant heat is applied to the heating platform for a fixed amount of time and then the cooling of the system is measured as a function of time. The cooling of the system behaves according to the differential equation: $C_{total}\frac{dT}{dt} = -K_w(T - T_B) + P(t)$ where C_{total} is the total heat capacity of the system, K_w is the thermal conductance of the system, T and T_B are measured temperatures of the system and $P(t)$ is the applied power to the heating platform. This is a first order differential equation with an exponential solution which is used to model the growth and decay of the sample temperature as a function of time through the Quantum Design software to extract the total heat capacity.

This setup only measures the total heat capacity of the system: puck, grease, and sample. This means that in order to extract just the component of heat capacity of the sample, a preliminary measurement of the puck and grease must be done, called an addenda. Addenda measurements are typically done with less temperature intervals, in order to save time, and data points are interpolated as required to match the experimental data for the sample. Heat capacity measurements are typically done at low temperature but will be done at any temperature where a phase transition has been observed. One caveat of this is that at higher temperature, the growth and decay of the temperature of the system can take very long to achieve so measurement times for a complete measurement may take on the order of days. Addenda heat capacity values are subtracted from the total heat

capacity values to yield the heat capacity of the sample itself which can be converted to specific heat if the mass and molar mass of the sample are known.

Another complication which may arise in these measurements is that the exponential solution assumes a perfect coupling between the sample platform and the sample itself. This is not always the case and poor coupling can cause the modeling from the software to be very poor. The Quantum Design software does allow for the case where there is thermal link from the stage and the sample and modeling using this fitting procedure is employed when data modeled using the previously mentioned functional dependence is poor. In many case, poor sample coupling can be fixed by added more grease to the sample stage to ensure there is thermal contact between the sample stage and the sample. In one instance, a pressed pellet of a material was used as opposed to a single crystal as single crystals of the material was unable to achieve appropriate thermal coupling.

2.2.8 Electron microscopy

Electron microscopy is a catch-all term for any imaging and diffraction technique which uses electrons as the source of illumination in contrast to traditional microscopy which uses light as the source of illumination. All electron microscopy characterizations were carried out in the Advanced Imaging and Microscopy Laboratory (AIM) Lab at the University of Maryland Nanocenter through collaboration with Dr. Sz-Chian Liou. Two main techniques were used scanning electron microscopy (SEM) and transmission electron microscopy (TEM).

Scanning electron microscopy was performed on a Hitachi SU-70 field emission

scanning electron microscope and energy dispersive X-ray spectroscopy (EDS) was done using a Bruker EDS detector. Typically, an image is produced by secondary electrons which are emitted from the sample by excitation from the incoming electrons. SEM images can typically achieve resolution on the nanometer scale which is useful for determining sample morphology. Most importantly, SEM techniques are used for elemental analysis using EDS techniques. In the EDS method, X-rays are produced by the sample as the high energy electrons cause the atoms of the sample to lose inner core electrons. Those inner core electrons are then replaced by outer core electrons which radiate down in energy by releasing an X-ray. These X-rays are characteristic for each element and are well-cataloged. Thus, the atomic composition of the sample can be determined by measuring which characteristic X-rays are produced. In general, EDS techniques are sensitive on the order of 2-5% atomic composition. In some cases, characteristic X-rays of two elements may have strong overlap in energy which can cause large errors in evaluating the elemental composition of a sample. Another issue which may arise from EDS analysis is that the measurement can easily be contaminated by impurities which will yield confusing elemental compositions. In the case where a sample may have impurities, the sample morphology is easily shown via SEM images and EDS is only performed on crystallites with the correct morphology. In typical usage, elemental analysis from EDS is used to corroborate Rietveld refinement data from X-ray or neutron diffraction in order to determine the elemental composition of the sample.

Transmission electron microscopy was performed on a JEM 2100 LaB_6 transmission electron microscope with an acceleration voltage of 200 KeV. The main difference between SEM and TEM is that TEM uses transmitted electrons for imaging as opposed

to reflected electrons as in SEM images. The main benefit of this is TEM is not strictly limited to surface characterization as SEM is typically used for surface morphology and imaging. For our research, the TEM is employed to produce electron diffraction images of a powder sample. Electron diffraction has been useful for systems with very complicated crystal structures. The main reason is that the wavelength of the electrons used are 0.25 Å whereas typical X-ray diffractometers using Cu Kα radiation has a wavelength of 1.54 Å and neutrons are typically even longer wavelength. A shorter wavelength means that the Ewald sphere for meeting Bragg conditions in the reciprocal lattice is much larger which means many more Bragg reflections can be identified.

Another huge benefit of TEM electron diffraction is that because electrons can be focused down to a very small size, this allows for nanometer size crystallites to be individually used for diffraction experiments. For our research, using hydrothermal reaction often times produces very small crystallites on the nanometer scale. Thus, electron diffraction offers the ability to do diffraction on a single crystallite in order to help determine the crystal structure. Albeit, electron diffraction patterns alone are typically not enough to accurately determine a crystal structure or lattice parameters and are often used as a complementary technique to traditional X-ray or neutron diffraction techniques. Another caveat, is that small crystallites are typically required for TEM and electron diffraction as the sample must be thin enough to allow electrons to transmit without significant absorption and reflection.

On the whole, electron microscopy is a very useful set of techniques to be used when single crystal samples are not able to be synthesized. SEM imaging allows for sample morphology to be determined which is extremely useful in determining different im-

purities phases. This is especially true in our research where our desired products are layered phases which are usually very easily identified in SEM images. TEM has also been particularly useful to determine the symmetry present in our intercalated sample using electron diffraction. In particular, in systems with complex intercalated species, electron diffraction is useful to image the four fold symmetry of the transition metal chalcogenide layers to show they remain intact through intercalation.

2.2.9 Inductively coupled plasma - atomic emission spectroscopy

Inductively coupled plasma - atomic emission spectroscopy (ICP-AES) is a elemental composition technique which is done to determine metal concentrations in a product to extremely high levels of accuracy. This work was done in collaboration with Dr. Marya Anderson and the Environmental Engineering Laboratories in the Department of Civil and Environmental Engineering at the University of Maryland. Data was collected using a Shimadzu ICPE-9000 spectrometer which utilizes an argon plasma source to ionize sample solutions. For ICP-AES analysis, a sample solution is ionized using an argon plasma and characteristic emission lines are collected using a spectrometer within the instrument depending on which elements were ionized in the argon plasma. The intensity of each characteristic emission for each element is then matched with a known calibration of standards.

The standard and sample preparation is the most difficult part of ICP-AES analysis. Standard preparation requires the preparation of typically 5-7 standards of known concentration made from commercially purchased elemental solutions (purchased from

FLUKA). These standards are acquired at a concentration of 100 ppm and must be diluted down to form a calibration curve, typically in the range of 0.2, 0.5, 1, 2, 5, 10, 20, 100 ppm. This full range of a standards allows for samples of a wide variety of concentrations to be properly characterized. Sample preparation is done through the dissolution or digestion of a bulk sample and dilution down to concentrations within the calibration curve are required. To start, a bulk sample, crystal or powder, is massed and then dissolved in concentrated nitric acid until the entire sample is fully solvated; this is done in a hood for safety. One important note, ICP-AES is known as a destructive method whereby the sample must be dissolved and cannot be recovered for the analysis. Thus, it is only done when completely necessary to accurately determine the elemental composition when other techniques such as SEM-EDS and Rietveld refinement of powder diffraction data is not sufficient. The sample solution is now diluted to 2% nitric acid which is required for proper ionization in the argon plasma for this particular instrument. The initial mass of the bulk sample and the dissolution is used to determine the approximate concentration of each element in the solution to ensure it falls within the range of the calibration curve.

This process is done for each standard and each sample and at least 15 mL of each sample solution is required for proper usage on the instrument. This is because each measurement is done in triplicate as the instrument takes 5 mL aliquots from the sample solution and feeds them into the argon plasma torch for spectroscopic analysis. The instrument automatically runs through each sample up to a total of 60 samples. Once data has been collected, the software requires the user to select which characteristic emission wavelengths are chosen for each element and to ensure the calibration curve is accurate. Once those are chosen, the software matches each emission intensity for each element in

each sample to the calibration curve and determines the concentration of each element in the sample. This data can then be used to determine the relative atomic percents of each element in a sample to determine the stoichiometry. For ICP-AES analysis typically errors are in the < 0.1 ppm which equates to 0.00001 atomic percent. However, larger errors typically arise from weighing the bulk sample and determining the dilution of each sample which typically puts an error bar of < 0.01 atomic percentage depending on accuracy of the balance used and volumetric glassware for serial dilutions.

One caveat of the ICP-AES technique is that it is not able to determine the concentration of non metallic elements such as nitrogen, oxygen, halides and noble gases within the sample. This is even true for some metalloid elements depending on the digestion method used. All together, ICP-AES analysis is typically used for very accurate metal concentration determination in a sample and is used in conjunction with SEM-EDS and Rietveld analysis techniques to understand the stoichiometry and elemental composition of a material.

2.2.10 Thermal stability and characterization

Thermal stability measurements on samples were performed using two different techniques: thermogravimetric analysis (TGA) and differential scanning calorimetry (DSC). Both techniques are used to determine how thermally stable a material is with regards to heating in different environments. For our research, this has implications for determining the composition of a material as well as understanding how a material may be used in future research. Thermogravimetric analysis and differential scanning calorimetry was

conducted on a Mettler-Toledo TGA/DSC 3+ with high temperature furnace; typically samples were heated from room temperature to 800 °C in both an air and inert gas atmosphere to see how they behaved in different environments.

Thermogravimetric analysis measures the mass of a sample very accurately as a function of time as a heating profile is applied to the sample. The change of mass as a function of time and temperature describes different thermal phenomena in the sample such as phase transformations and decomposition. One piece of very useful information which can be gleaned from TGA analysis with regards to our research is to show how intercalated species behave in a compound. This is especially true for organic intercalates which will decompose at relatively low temperatures, which can be shown as an abrupt and significant mass change in a sample at some characteristic temperature which describes the temperature at which the sample de-intercalates the organic molecule and the organic molecule decomposes through oxidation.

Differential scanning calorimetry is a similar technique but is used specifically to determine the phase transformation of a material. In this technique, the sample and a reference sample are heated at the same rate. The temperature of each sample is monitored as a function of time as the sample will allow heat to flow differently than the reference sample. At some temperature, the heat flow will change abruptly which indicates the sample is going through a phase transformation. We use this information to understand the thermal stability of new compounds and this informs us about what possible chemical manipulations and post synthetic modifications are available for a particular material.

2.2.11 Density functional theory calculations

Density functional theory (DFT) calculations are performed by our group in order to match experimental results to theoretical calculations. Through density functional theory caculation code, we are able to predict the stability of a compound depending on its crystal structure and lattice parameters.

All density functional theory (DFT)[144,145] calculations were performed by using the Vienna Ab-initio Simulation Package (VASP)[146–149] software package with potentials using the projector augmented wave (PAW)[150] method. The exchange and correlation functional were treated by the generalized gradient approximation (PBE-GGA).[151] The cut-off energy, 450 eV, was applied to the valance electronic wave functions expanded in a plane-wave basis set. A Monkhorst-Pack[152] generated 23×23×17 k-point grid was used for the Brillouin-zone integration to obtain accurate electronic structures. I would like to thank University of Maryland supercomputing resources (http://www.it.umd.edu/hpcc) made available for conducting DFT calculations in this thesis.

A typical workflow for our group with regards to DFT calculations is as follows. A new material is synthesized and the structure and properties are measured through the long list of characterization techniques listed above. We then will complete density functional theory calculations on the compound in order to determine how well our results match those predicted by theory. It must be noted that density functional theory, especially those performed by VASP, which is a pseudopotential method, are not exact solutions. They are always approximations; structural properties and dynamics are typically fairly close to experimental values, but electronic and magnetic properties may vary greatly

between experiment and theory. This is because, especially in our research, the hardest aspects of the physical system to account for is the electron-electron correlations which are typically non-negligible and significant.

To start, a measured crystal structure is arranged in the VASP software and a preliminary calculation is done in order to determine the optimal lattice parameters for the system using a series of fixed lattice calculations. These calculations yield some energy for the system as calculated, and that energy is then plotted as a function of lattice parameters or volume of the unit cell. These energy values as a function of volume is then fit with an equation of state to determine the optimal lattice parameters for the system. As a last step for structural calculations, the optimal lattice parameters are used for a structural calculations where the ions in the unit cell are allowed to relax which as a whole allows the lattice parameters to change as well as atomic coordinates. Once this calculation is done, the optimal structure has been calculated for the system at hand. This structure is then used for all electronic property calculations.

The first step for electronic property calculations is to perform a self-consistent field calculation. Here, the optimal fixed structure is used iteratively to determine optimal description of the electron density functional for the system. Once this is optimized, the fixed structure and fixed electron density functional is used to calculate density of states as well as band structure. VASP software allows for angular momentum decomposition within the calculations so that each orbital contribution can be determined in the density of state and band structure calculations. This is particularly useful for our materials as transition metal d-orbitals are the most significantly contributing at the Fermi level. Throughout these processes, the effect of electron spin degree of freedom can be consid-

ered or not which equates to considering if the system should have magnetic order or not. As a caveat, due to the way the calculations are done starting with structure, complex magnetic order of the antiferromagnetic or ferrimagnetic type require the construction of a supercell of the original unit cell. This is a more advanced technique and in cases where magnetic order is the direct aim of the calculations collaborations are usually required.

In conclusion, our group uses DFT calculations as a method to confirm experimental findings in our materials. It is a very powerful technique which allows the user to understand the ground state properties of a material. As noted, the theory has many approximations which means the technique can be used with appreciable accuracy for structural properties but electronic and magnetic properties may vary between experiment and theory. Another note of caution, all calculations begin with an accurate description of the structure of the material; any error in the structure will lead to huge errors in the electronic property calculations. There are many references which describe how to use VASP and related software listed here.[153,154] In particular, VASP software page `https://www.vasp.at/wiki/index.php/The_VASP_Manual` and the materials explorer function on the Materials Project `https://materialsproject.org/` offers a wide-range of functionality and starting points for DFT calculations.

Chapter 3: Topochemical synthesis and frustrated magnetism in CoSe - analog of superconducting FeSe

The work described within this chapter was published in *Journal of the American Chemical Society* **2016**, *138*, pg. 16432. Xiuquan Zhou, Hector Vivanco, Johnpierre Paglione, Craig M. Brown, and Efrain Rodriguez were contributing authors of the manuscript. B.W., X.Z. and H.V. prepared the samples, X.Z. performed MPMS measurements and DFT calculations, B.W. collected resistivity data, X.Z., B.W., and C.M.B. collected the neutron data. as well as *Physical Review B* **2018**, *97*, pg. 104408. Xiuquan Zhou, Hector Vivanco, Daniel J. Campbell, Kefeng Wang, Dave Graf, Johnpierre Paglione and Efrain Rodriguez were contributing authors for the manuscript. B.W., X.Z., and H.V. contributed to crystal growth, B.W. collected MPMS measurements, AC susceptibility measurements, and heat capacity measurements, X.Z. performed DFT calculations, and D.J.C., K.W. and D.G. collected the high field resistivity data.

3.1 Prologue

The majority of the work described in this chapter was enabled by preceding work on the synthesis of the metastable CoSe which is isostructural to FeSe in the iron chalcogenide superconducting family. Superconductivity is very sensitive to doping and chem-

ical effects so from an experimental point of view, the next step would be to substitute iron for other transition metals in order to investigate how these dopants affect superconductivity in the system. It was found that the all transition metal substitutions are limited to ~ 10% substitution on the iron site due to phase transformation or the appearance of multiple competing phases and all the dopants except manganese were shown to destroy superconductivity with minimal doping.[155–158] As mentioned, FeSe is the only tetrahedral metal chalcogenide to crystallize in this structure type. Thus, when doping the system beyond some limit, thermodynamics will govern the formation of other phases which moves away from the desired structural motif. This is where the requirement for a new reaction pathways, kinetically controlled, is needed in order to overcome thermodynamics and stabilize the phase desired.

Superconductivity in FeSe was reported in 2008, but was not reported in the sulfide analogue, FeS, until 2015. This is because anti-PbO type FeS (mackinawite) is metastable and previous *chimie douce* synthetic methods used resulted in the observation of ferromagnetic semiconducting behavior.[159,160] However, in 2015 a new hydrothermal synthetic scheme was devised to form FeS and found superconductivity at 5 K;[58] the discrepancies in these works can be attributed to the instability of mackinawite which transforms to Fe_3S_4 under adverse conditions. More recently, another reaction scheme was devised to form single crystals of tetragonal FeS through topochemical de-intercalation of $K_xFe_{2-y}S_2$, which supported the previous work with FeS formed through this method exhibiting superconductivity at 4 K.[59] This de-intercalation of potassium ions between layers of FeS utilized the thermodynamic stability of $K_xFe_{2-y}S_2$, which can be formed through a solid-state self flux method,[161] to access the desired structural motif to form

anti-PbO mackinawite. This led to a general realization of the possibility to target other extended solids through the de-intercalation of $A_xM_2Ch_2$, where A = alkali metal, M = transition metal, and Ch = chalcogenide to form other anti-PbO type tetrahedral transition metal chalcogenide.

Here, we target the synthesis of the cobalt analogues to superconducting FeSe and FeS through a kinetically controlled topochemical de-intercalation of the thermodynamically stable $K_xCo_2Ch_2$ phases. However, in general, the ICSD lists 1865, 40 being chalcogenides, compounds that crystallize in the $ThCr_2Si_2$ structure which could offer an expansive playground for future utilization of *chimie douce* techniques to form new materials. The corresponding phases, KCo_2Se_2 and KCo_2S_2, were synthesized by Greenblatt *et al.* and their group has developed extensive methods to synthesize these ternary/quaternary chalcogenide.[162–164] Their work reported ferromagnetism in KCo_2Se_2 and KCo_2S_2 with Curie temperatures, T_C = 78 and 127 respectively. Thus, the targeting of CoSe and CoS, isostrutural to FeSe, fulfills two routes of investigation: 1) how does changing metal oxidation states and electronic configuration affect the physical properties from KCo_2Ch_2 to CoCh, and 2) how do the properties in these metastable cobalt chalcogenides relate to superconductivity in the iron-based system. So, in total, this preliminary work aims to investigate a kinetically controlled route to form metastable tetrahedral cobalt chalcogenide phases, the character of the magnetic interactions on the layered Co square lattice, and how the physical properties relate to superconductivity in the analogous iron system.

Figure 3.1 illustrates the collection of synthetic routes encountered through attempts to synthesize metastable tetragonal CoSe and CoS phases. In Figure 3.1, the successful topochemical de-intercalation process is shown.

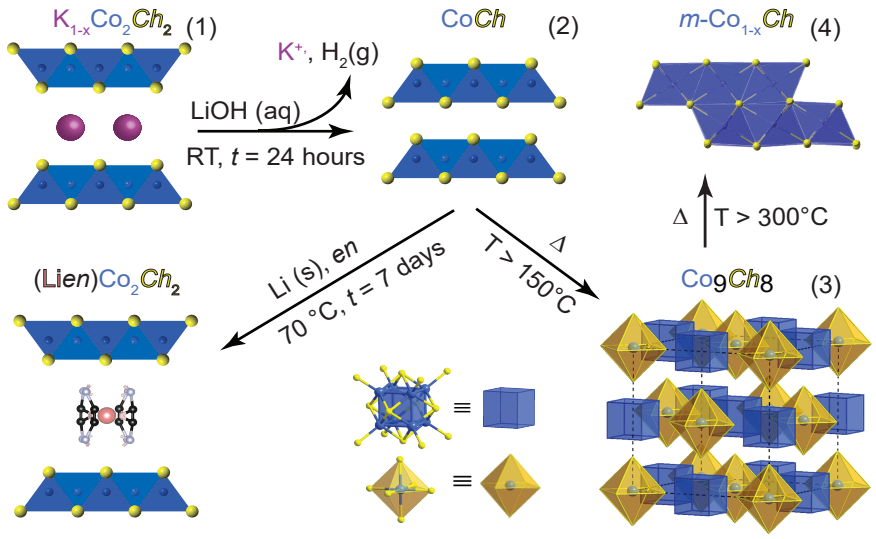

Fig. 3.1: Reaction schemes for the topochemical synthesis of cobalt chalcogenides. Thermodynamically stable KCo_2Ch_2 is converted to tetragonal Co*Ch* through a room temperature de-intercalation reaction. Higher temperature cause the formation of cobalt pentlandite and monoclinic Co*Ch*. Possible avenues for intercalation are shown so Li*en*CoSe can be formed where *en* = ethylenediamine.

In this process, KCo_2Ch_2 reacts with water to form KOH and evolve hydrogen gas through the extraction of interlayer potassium ions to form Co*Ch* depicted below:

$$KCo_2Ch_2(s) + H_2O(l) \longrightarrow 2CoCh(s) + KOH(aq) + \frac{1}{2}H_2(g) \tag{3.1}$$

Due to the observed evolution of hydrogen gas, the reaction rate could be semi-quantitatively studied to understand how the de-intercalation reaction proceeds. Analysis confirmed that the de-intercalation reaction involved the hydration of K^+ ions to form KOH accompanied by a transfer of electrons between $Co^{1.5+}$ ions and H_2O to release H_2 gas. The reaction scheme in Figure 3.1 illustrates the necessity to complete the de-intercalation under strongly basic conditions in order to ensure the formation and stability of Se^{2-} ions so that no selenium is lost to the formation of selenide compounds.[165]

Powder x-ray diffraction (PXRD) was performed in order to compare the crystal

structure of KCo_2Ch_2 and Co*Ch*; Figure 3.2 shows PXRD and neutron powder diffraction (NPD) patterns for KCo_2Se_2 and CoSe.

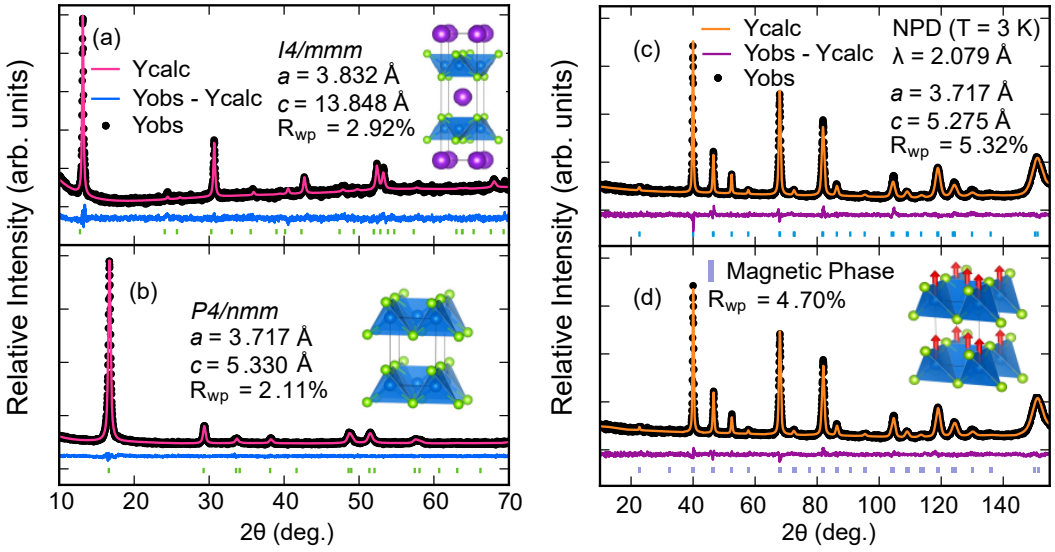

Fig. 3.2: Powder X-ray diffraction patterns of (a) KCo_2Se_2) at room temperature and (b) CoSe room temperature. (c) Neutron powder diffraction (NPD) pattern of CoSe at 3 K (d) NPD pattern with attempted magnetic refinement of the ferromagnetic contributions. Tick marks representing the phases are shown below the calculated, observed, and differences curves from Rietveld analysis.

As seen from the x-ray and neutron data (details listed in Table 3.1), de-intercalated CoSe can be matched very well with the anti-PbO structural model with neither diffraction pattern showing contributions from remaining KCo_2Se_2 phase. Elemental analysis utilizing energy dispersive spectroscopy (EDS) and inductively-coupled plasma atomic emission spectroscopy (ICP-AES) techniques illustrate a composition of $Co_{0.98\pm0.02}Se$ with no residual potassium remaining in the selenide analogue. However, for the sulfide analogue, EDS measured 4.5 at.% remaining potassium owning to slightly incomplete de-intercalation which could be remedied through longer reaction times. In total, crystallographic and elemental analysis show the successful de-intercalation of KCo_2Ch_2 to form anti-PbO type tetragonal Co*Ch* phases.

KCo_2Se_2 (298 K, PXRD), *I4/mmm*, R_{wp} = 2.917%						
a = 3.832(2) Å, c = 13.848(3) Å						
atom	Site	x	y	z	Occ.	U_{iso} (Å^2)
K1	2a	0	0	0	0.94(6)	0.109(22)
Co1	4d	0	0.5	0.25	0.96(6)	0.060(11)
Se1	4e	0	0	0.359(3)	1	0.019(4)
Co-Se (Å)	Se-Co-Se (°)	Se-Co-Se (°)	Co-Co (Å)	anion height (Å)		
2.442(6)	103.4(4)	112.6(2)	2.710(3)	1.509(3)		
CoSe (298 K, PXRD) , *P4/nmm* , R_{wp} = 2.102%						
a = 3.717(3) Å, c = 5.330(3) Å						
atom	Site	x	y	z	Occ.	U_{iso} (Å^2)
Co1	2a	0	0	0	1	0.012(3)
Se1	2c	0	0.5	0.265(5)	1	0.010(3)
Co-Se (Å)	Se-Co-Se (°)	Se-Co-Se(°)	Co-Co (Å)	anion height (Å)		
2.332(2)	111.382(63)	105.8(2)	2.6284(3)	1.412(3)		
CoSe (3 K, NPD) , *P4/nmm* , R_{wp} = 5.318%						
a = 3.716(6) Å, c = 5.275(1) Å						
atom	Site	x	y	z	Occ.	U_{iso} (Å^2)
Co1	2a	0	0	0	1	0.0026(8)
Se1	2c	0	0.5	0.269(2)	1	0.0020(5)
Co-Se (Å)	Se-Co-Se (°)	Se-Co-Se(°)	Co-Co (Å)	anion height (Å)		
2.339(5)	111.632(36)	105.232(68)	2.6280	1.412(3)		

Tab. 3.1: Structural parameters for ground single crystals of KCo_2Se_2 and CoSe. Structures are for room temperature PXRD data and 3 K NPD data. All relevant bond angles and distances from the refinements are given. Standard uncertainties given in parantheses indicate one standard deviation.

To further understand the stability of these phases, extensive reaction condition experiments were executed to probe the appropriate thermal window for the formation of these phases. The remaining structures in Figure 3.1, cobalt seleno-pentlandite (Co_9Se_8: **3**) and monoclinic cobalt selenide (Co_3Se_4: **4**) illustrate the formed products through different temperature regimes. It was found that any hydrothermal reaction between 100 - 200 °C led to the co-existence of tetragonal CoSe and cobalt seleno-pentlandite with increasing formation of the monoclinic phase at elevated temperatures. To understand this in more detail, temperature-dependent x-ray diffraction was performed on ground single

crystals of tetrgonal CoSe from 27 - 600 °C in an Argon atmosphere. It was found that at 200 °C tetragonal CoSe completely transformed to the cobalt seleno-pentlandite phase. This remained the major product to 400 °C where it began to convert to the monoclinic phase which remained the major product up to 600 °C and when cooled back to room temperature. This illustrates that these tetragonal Co*Ch* phases have a limited thermal window of stability which can be exploited for future chemical manipulations. We now move on to describe the extensive physical property measurements employed in order to understand the interesting magnetism present in CoSe.

3.2 Introduction

The iron-based superconducters are composed of Fe^{2+} square lattices stacked to form layered materials. For example, the simple FeSe superconductor contains stacked layers of Fe^{2+} centers tetrahedrally-coordinated to selenide anions. Remarkably, its T_c of 8 K,[42] can be increased to 65 - 100 K when isolated as a single layer.[50] Therefore, it is the square sublattice of *d*-cations that may hold the key to understanding the physical properties of these systems. In this article, we have completely replaced the Fe^{2+} cations in FeSe with Co^{2+}, and studied its magnetization, magnetotransport and specific heat properties to further explore the physics of metal square lattices.

In addition to crystal structure, the relationship between magnetism and superconductivity is of paramount importance for these layered chalcogenides. In the iron pnictide superconductors (e.g. $BaFe_2As_2$ and LaOFeAS), suppression of the parent antiferromagnetic (AFM) phase can lead to the emergence of superconductivity.[24,166] However, no

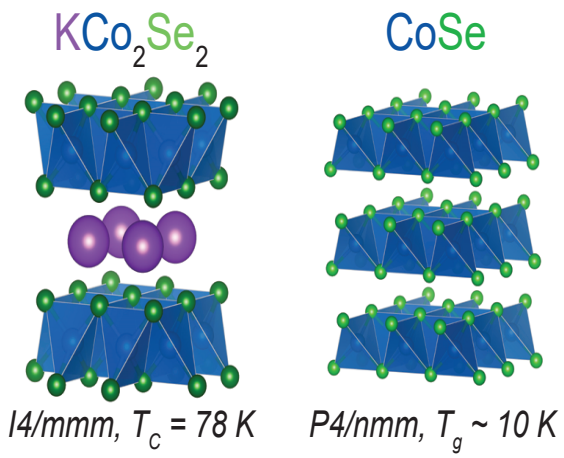

Fig. 3.3: Crystal structures of KCo_2Se_2 and CoSe.

long-range magnetic ordering has been observed in any of the FeSe or FeS superconductors. Although antiferromagnetism was found in $Fe_{1+x}Te$, the origin of its magnetism is different from that of the pnictides, and it is largely influenced by the amount of interstitial iron.[167–169] Thus, it is less clear how magnetism and superconductivity interact in the Fe*Ch* (*Ch* = chalcogenide) systems compared to their pnictide counterparts.

Currently, one key issue is that isostructural systems to Fe*Ch* are limited due to synthetic challenges. Previously, we have overcome this challenge by topochemical means to convert KFe_2S_2 to superconducting FeS.[59] Using a similar method, we successfully prepared two new Fe*Ch* analogues, tetragonal CoSe and CoS.[61] The ferromagnetic ordering from 78 K in KCo_2Se_2[164] to 10 K in CoSe[61] was suppressed by de-intercalation of potassium cations to form pure CoSe as shown in Figure 3.3. These new Co-based phases are promising for understanding the Fe-based superconductors due to their structural and electronic proximity.

Much of the work performed to understand the magnetism in iron pnictides has been done with those that adopt the $ThCr_2Si_2$ structure-type ("122"-system). This structure-

type allows for a wider range of substitutions on the metal, anion and interlayer cation sites to study doping effects.[27,82,87,170] There has been extensive work on the cobalt analogues to "122" iron pnictides, ACo$_2$$Pn_2$, with various interlayer alkali or alkali-earth cations (A).[171–178] The observed magnetism in these pnictides was largely tuned by size and electronic effects from changing the CoPn layer distances.

An intriguing question is: can CoSe be tuned into a superconductor like FeSe? By directly comparing their band structures, CoSe chould share similar electron-hole pockets with FeSe if the electron filling level is reduced.[61] Therefore, it may be possible to tune CoSe into a superconductor by increasing the Co oxidation state to form d^6 cations isoelectronic to Fe^{2+}. In order to investigate this, two fundamental factors must be understood: 1) the character of the magnetic interactions within the Co square lattice, and 2) how its magnetism compares to other FeCh based superconductors. Here, we have performed extended magnetic and transport characterizations to understand the magnetism within CoSe and its proximity to superconductivity in related FeSe.

3.3 Experimental Methods

Single crystals and powders of CoSe were synthesized following the previous method in literature.[61] Crystals of CoSe were lustrous silver with high degree of layered morphology.

Temperature dependent DC (direct current) magnetic susceptibility measurements were carried out using a Quantum Design Magnetic Susceptibility Measurement System (MPMS) on powder samples of tetragonal CoSe. Field-cooled (FC) and zero field-cooled

(ZFC) measurements were taken from 1.8 K to 300 K with various applied magnetic field strengths. Magnetic hysteresis measurements were carried out using a PPMS DynaCool utilizing a vibrating sample magnetometer (VSM) taken at a series of temperatures with applied magnetic field between $H = \pm 14$ T on single crystals of CoSe mounted on a quartz paddle via Ge 7031 varnish.

AC (alternating current) magnetic susceptibility was measured with a 14 T Quantum Design Physical Property Measurement System (PPMS-14) on powder samples of tetragonal CoSe. Zero field-cooled measurements were taken from 35 K to 1.8 K with an AC-field of 10 Oe and AC-frequencies of 10 Hz to 10 kHz. Due to the instrument setup, a residual DC field within the PPMS-14 ranged from 40 Oe to 100 Oe.

Electrical transport measurements were preformed using a 9 T Quantum Design Physical Property Measurement System (PPMS-9) with single crystals of CoSe mounted on a Quantum Design AC transport puck. Electrical resistivity was measured using the four-probe method with gold wire and contacts made with silver paste. The temperature and field dependence of longitudinal electrical resistivity was measured in a range from 300 K to 1.8 K with applied fields up to 9 T.

Electrical transport measurements at fields up to 31 T were performed at the DC Field Facility of the National High Magnetic Field Laboratory in Tallahassee, Florida. Angular dependence measurements at base temperature of the He-3 system (500-600 mK) were made by rotating the sample plane (*ab*-plane) from perpendicular (0 degrees) to parallel (90 degrees) to the applied field. Temperature dependent magnetotransport was measured for applied field both perpendicular and parallel to the sample plane between base temperature and 12 K.

Heat capacity measurements were preformed using the PPMS-14. Heat capacity measurements on tetragonal CoSe single crystals yielded poor results due to low thermal contacts arising from the micaceous nature of the CoSe flakes. Consequently, a pressed pellet of CoSe ground single crystals was used for the heat capacity measurements performed with the relaxation technique.[143,179,180]

All density functional theory (DFT)[144,145] calculations were performed by using the Vienna Ab-initio Simulation Package (VASP)[146–149] software package with potentials using the projector augmented wave (PAW)[150] method. The exchange and correlation functional were treated by the generalized gradient approximation (PBE-GGA).[151] The cut-off energy, 450 eV, was applied to the valance electronic wave functions expanded in a plane-wave basis set. A Monkhorst-Pack[152] generated 23×23×17 k-point grid was used for the Brillouin-zone integration to obtain accurate electronic structures.

3.4 Results

3.4.1 Magnetic properties

Our previous work demonstrated the suppression of ferromagentism from 78 K in KCo_2Se_2[164] to 10 K in CoSe[61]. However, due to the very low ordering moment as well as the proximity to the iron-based superconductors, a more detailed investigation of the magnetism and electronic properties has been undertaken.

Figure 3.4 shows the temperature dependence of inverse FC magnetic susceptibility for ground single crystal samples of CoSe at various applied DC fields. The inverse susceptibility was fit in the paramagnetic range from 100 K to 300 K to the Curie-Weiss

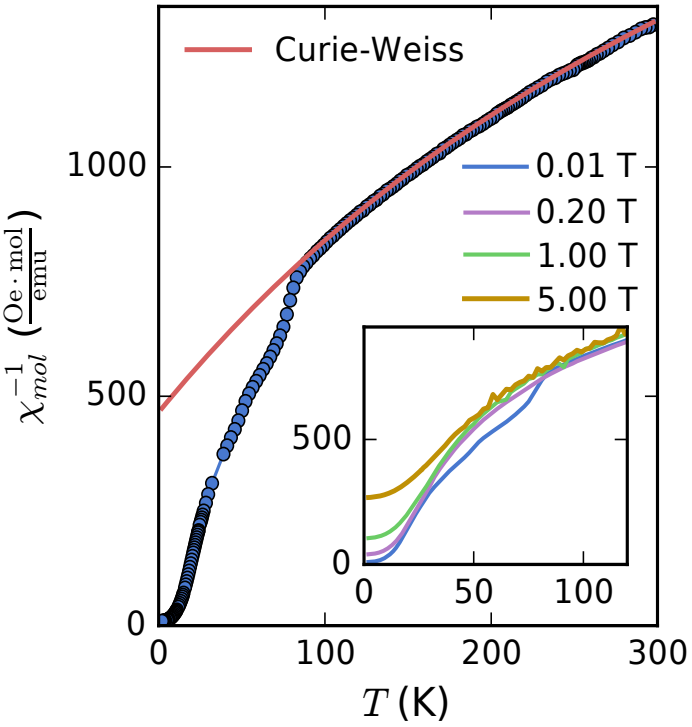

Fig. 3.4: Inverse magnetic susceptibility of CoSe *vs.* temperature measured in applied field of 100 Oe. The inverse magnetic susceptibility is fit from 100 K to 300 K to the Curie-Weiss law plus a temperature-independent term. The inset shows inverse magnetic susceptibilities for different applied DC fields (0.2 T, 1 T and 5 T) to emphasize the change in slope near 82 K.

law:

$$\chi_{mol} = \chi_0 + \frac{C}{T - \Theta_{CW}} \tag{3.2}$$

where $\chi_0 = 3.52 \times 10^{-4} \frac{emu}{Oe \cdot mol}$ accounts for parasitic paramagnetic and diamagnetic contributions, $C = 0.1579 \frac{emu \cdot K}{Oe \cdot mol}$ denotes the Curie constant, and Θ_{CW} = -87.29 K is the Weiss constant. A strongly negative Weiss constant empirically indicates predominant antiferromagnetic fluctuations.

The frustration parameter, f, for a magnetic system is defined as the ratio of the absolute value of the Weiss constant and the observed ordering temperature from magnetic

susceptibility:[181]

$$f = \frac{|\,\Theta_{CW}\,|}{T_C} \tag{3.3}$$

We obtain a frustration parameter of approximately 8.7, indicating strong suppression the magnetic ordering temperature. The inset of Figure 3.4 displays the inverse susceptibility behavior with different applied fields; it is shown that the paramagnetic regime (> 100 K) does not change, but the deviation at approximately 82 K shows differing behavior with applied DC field. Empirically, in the frustrated regime ($T_c < T < |\Theta_{CW}|$) increasing field drives the system toward increasing antiferromagnetic fluctuations as the slope of $\chi^{-1}(T)$ decreases.

Our earlier work showed that the magnetic susceptibility of CoSe exhibited a ferromagnetic transition at 10 K, but the discontinuity at 10 K was not a classic example of a ferromagnetic transition. In order to explore this, the temperature dependence of magnetic susceptibility was measured at different fields to see how the transition was altered. Insets of Figure 3.5 shows the magnetic susceptibility from 10 K to 1.8 K at various applied fields. At low fields, 0.01 T, the transition at 10 K is clear from the bifurcation of the zero-field cooled (ZFC) and field-cooled (FC). However, as the field is increased, the transition temperature is suppressed until at high fields, > 2 T, there is a complete suppression of the ZFC-FC splitting indicative of complete suppression of long-range ferromagnetic ordering.

The closing of the normal ZFC-FC splitting at the proposed ferromagnetic transition is a hallmark of spin glass behavior as opposed to classic ferromagnetism.[137] Without a

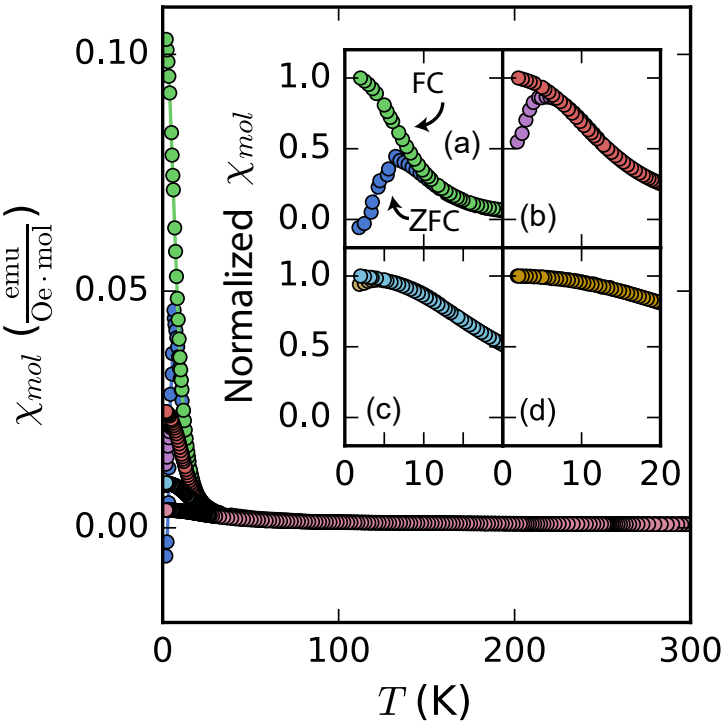

Fig. 3.5: Magnetic susceptibility of CoSe *vs.* temperature measured in various applied fields. The insets show the zoomed region close to the transition temperature; ZFC (Zero field-cooled) and FC (field-cooled) curves are shown by arrows which indicate the irreversibility of the magnetic ordering in the system at low fields. The bifurcation of ZFC-FC curves at low applied field (a) = 0.01 T and (b) = 0.2 T is destroyed with high applied fields (c) = 1 T and (d) = 5 T turning the system into a paramagnetic state with no irreversibility.

sufficiently applied field, spins are able to “freeze" in the random orientation of spin glass yielding net magnetization opposing the applied field in the ZFC process. With a stronger field, the “freezing" is destroyed as the spins are forced to align with the applied field. We can rule out superparamagnetism as a possible explanation as we have observed remanent magnetization and magnetic hysteresis for CoSe which would not occur in a superparamagnetic material.[61] In order to observe the glassy character in CoSe, we performed AC magnetic susceptibility measurements to probe the time-dependence of the magnetization around the transition temperature.

AC-susceptibility measurements use an applied field with a time-dependent wave-

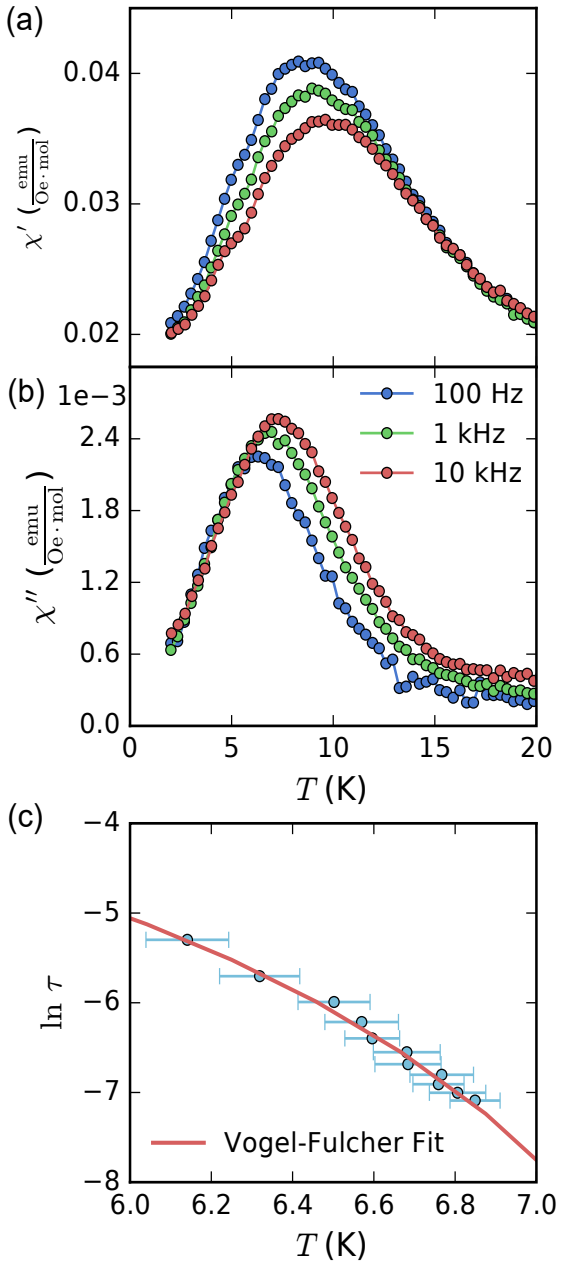

Fig. 3.6: AC magnetic susceptibility measured with various driving frequencies. The applied AC field was 10 Oe and the residual DC applied field due to internal instrumentation was 40 Oe to 100 Oe. (a) The real parts of magnetic susceptibility (χ') and (b) the imaginary parts (χ'') parts. (c) Temperature dependence of χ" peaks at various driving frequencies (100 to 1200 Hz) and a fit with the Volger-Fulcher law.

form to produce a time-dependent response in the material. It can therefore probe spins fluctuating with time such as in spin glasses or strongly frustrated systems.[137] Figure

3.6 shows the real (χ') and imaginary (χ'') parts of magnetic susceptibility as a function of temperature near the transition. Frequency dependence in χ' appears below 10 K, and accompanying non-zero peaks in χ'' indicate some out-of-phase contributions to the magnetic susceptibility. Thus, time-dependence in the magnetic domain size arises below 10 K, and any mangetic ordering appears dynamic down to base temperature.

A fit to the non-zero χ'' peaks with the Arrhenius law would be simple yet inadequate for canonical spin glasses and spin-glass-like materials. The transition into the glassy state is more than a simple thermal activation process, and magnetic moments can also be strongly interacting.[137] A more phenomenological approach that incorporates different regimes of coupling above and within the glassy state uses the Vogel-Fulcher law:[137,139]

$$\tau = \tau_0 \cdot \exp\left(\frac{E_a}{k_B(T_f - T_0)}\right) \tag{3.4}$$

where T_f is the temperature of the χ'' peaks, $\tau_0 = 1/\omega_0$ is the characteristic relaxation time, and k_B the Boltzmann constant. The added parameter, T_0, describes the 'ideal glass temperature' where the coupling of the system effectively changes to give rise to new phenomena.[137,139,182]

Our modelling of the AC susceptibility data with the Vogel-Fulcher law is shown in Figure 3.6c. The temperature values for T_f were fit by Gaussian curves in the range from 5-12 K. The fit yields parameters: $\tau_0 = 0.67 \pm 1.61$ s, $E_a = 12.75 \pm 10.47$ K, and $T_0 = 8.74 \pm 0.89$ K. The large degree of uncertainty in the relaxation time and activation energy comes from the high correlation between τ_0 and T_0 parameters and narrow temperature

range of the χ'' peaks.

The lack of meaningful values from the initial Vogel-Fulcher fit led us to perform additional analysis using a dynamical scaling model. Dynamical scaling relates the relaxation time of an observable to a correlation length that scales with a power law near the transition temperature. We consider scaling of the frequency-dependent transition temperature from the χ'' peaks such that:[183]

$$\tau = \tau^* \left(\frac{T_c - T_f}{T_f} \right)^{-zv} \tag{3.5}$$

where T_c is the critical temperature, τ^* the critical relaxation time, and zv the critical exponent. Our fit yields $\tau^* = 0.064 \pm 0.008$ and $zv = 5.47 \pm 0.21$, which fall into the general range of spin-glass and glassy-like materials[183].

Substituting the value of τ^* for the the characterstic relaxation time in the Vogel-Fulcher law, we obtain more precise values for the activation energy ($E_a^* = 14.84 \pm 0.59$ K) and ideal glass temperature ($T_0^* = 8.91 \pm 0.09$ K). The obtained critical relaxation temperature is significantly higher than canonical spin-glass materials, but compatible with Monte-Carlo modeling of a 3D Ising spin glass.[184,185]

3.4.2 Transport Properties

To further probe the dynamics of the transition within CoSe, we have employed more electronic transport measurements. Figure 3.7a shows the temperature dependence of electrical resistivity for CoSe. For a truly ordered material, one would anticipate a noticeable change in the resistivity near the critical point. However, no such anomaly

occurs in the resistivity measurements. This lack of an anomaly could be understood on the basis of weak ferromagnetism as the observed moment of CoSe via neutron diffraction is very small.[61]

We observe positive magnetoresistance for all applied field directions (Figure 3.7b), which does not occur in typical ferromagnets. The positive magnetoresistance can be interpreted in two ways: 1) the spins have no fixed direction and are randomly distributed as would be the case for a glass-like material, or 2) the spins are fixed but their associated moments are so small that their contribution to scattering is negligible.

The complete angular dependence of the resistance versus field direction at 31 T (Figure 3.7c) shows two-fold symmetry, which is due to the geometry of the four-probe longitudinal measurements. Angular measurements in other planes are not possible due to sample morphology. CoSe crystals are highly layered and micaecous so that only allow the *ab*-plane is available as the wiring surface.

We performed specific heat measurements from 1.8 - 150 K (Figure 3.9) on a pressed pellet of CoSe obtained through the potassium de-intercalation route. The micaecous nature of the single crystals caused poor thermal coupling between the sample and the heating platform, and we therefore utilized a pressed pellet of CoSe. For comparision, we also performed specific heat measurements of KCo_2Se_2 single crsytals, known from previous studies to exhibit a clear ferromagnetic transition below 80 K.[164,186] Our own heat capacity measurements of KCo_2Se_2 confirm a clear transition at 78 K shown in Figure 3.8. The temperature dependence of the specific heat for CoSe, however, shows no anomaly near 78 K.

The inset of Figure 3.9 shows a zoomed in region around the transition observed

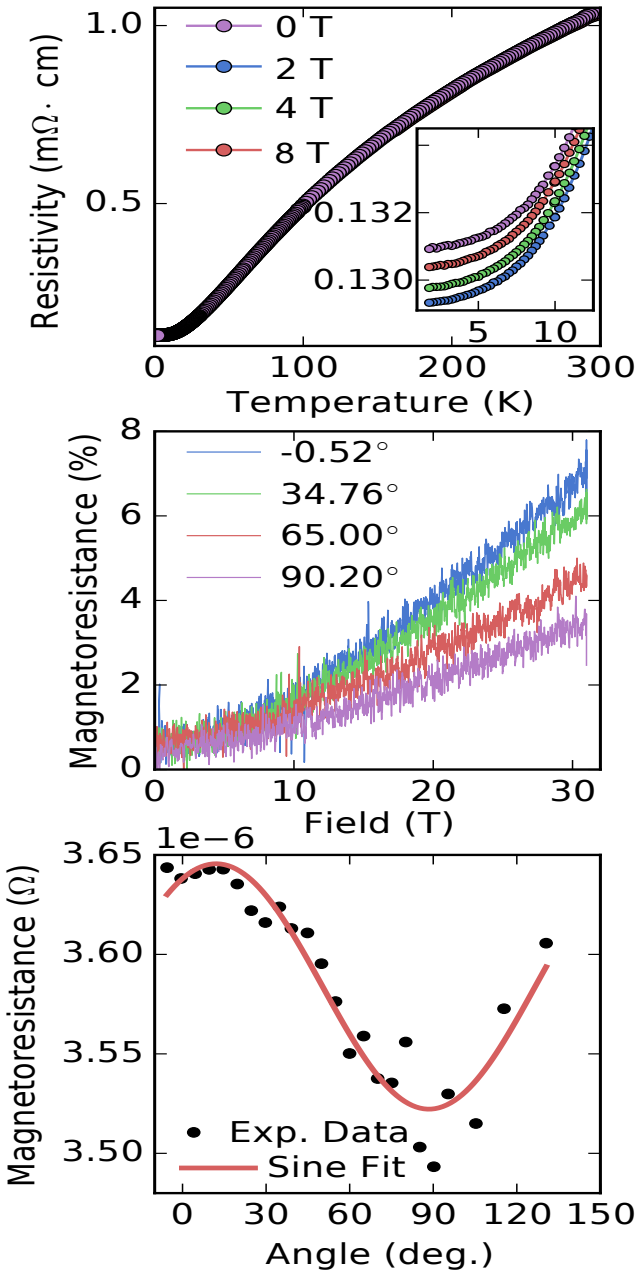

Fig. 3.7: Electrical transport measurements of CoSe single crystals obtained through de-intercalation of KCo_2Se_2. (a) Temperature dependence of longitudinal resistivity at various applied fields with inset around the transition temperature. (b) Normalized longitudinal magnetoresistance up to 31 T with different applied field directions by sample rotation. (c) Angular dependence of longitudinal magnetoresistance at an applied field of 31 T. The magnetoresistance is fit with a sinusoidal dependence to the field angle.

in magnetic susceptibility measurements with a fit to a conventional specific heat model.

There is no apparent discontinuity in the specific heat in this region, which indicates a

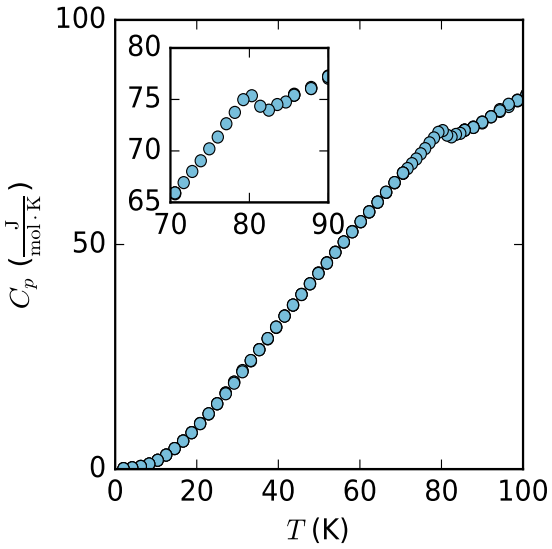

Fig. 3.8: Specific heat as a function of temperature measured on a single crystal of KCo_2Se_2 measured from 1.8 - 100 K with no applied field. Specific heat shows a distinct discontinuity at 79 K which corresponds to previous reports of the ferromagnetic transition in KCo_2Se_2; this is used to further prove the lack of KCo_2Se_2 phase within our CoSe samples signifying that complete de-intercalation is achievable for this system.

lack of a distinct phase transition. This result either supports a glass-like material,[137,139] or that the magnetic ordering does not change the energy scale due to the low ordering moment of a weak itinerant ferromagnet.[187,188]

The low temperature region of the specific heat, T < 15 K, was fit to a general model to extract electronic and vibrational contributions.[134]

$$C_p = \gamma T + \beta T^3 + cT^5 \tag{3.6}$$

where the γ-term accounts for electronic contributions and β/c-terms for vibrational contributions. The fit yields a γ = 15.7 mJ mol^{-1} K^{-2}, significantly larger than in the iron-based analogues FeSe and FeS (5.4 and 5.1 mJ mol^{-1} K^{-2}, respectively).[44,59] This could indicate stronger electron correlations in the cobalt system. However, recent angle-

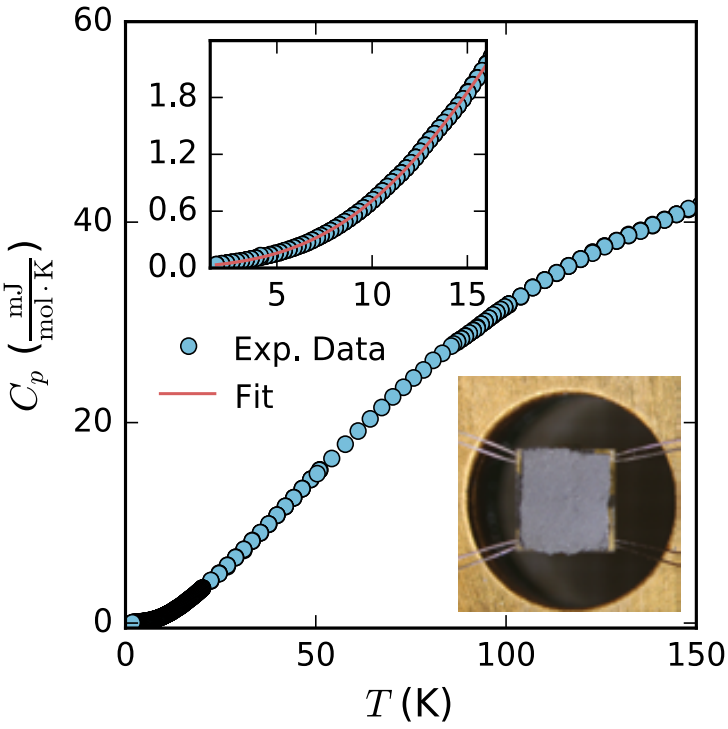

Fig. 3.9: Temperature dependent specific heat of a pressed pellet of CoSe from 150 K to base temperature. Upper inset shows the temperature dependence near the transition temperature as well as a fit to a specific heat model accounting for electronic and vibrational components in the range 1.8 K to 15 K.

resolved photoemission spectroscopy (ARPES) work on related KCo_2Se_2 indicated weaker electron correlations in the cobalt system than in the KFe_2Se_2 analogue.[189] A possible explanation for the larger γ in CoSe than in FeSe is that it arises from spin fluctuations present in a weak intinerant ferromagnet.[190,191]

We can use the parameter $\beta = 6.2 \times 10^{-4}$ mJ mol^{-1} K^{-4} to calculate the Debye temperature, Θ_D, for CoSe by the relation:[134]

$$\Theta_D = \left(\frac{12\pi^4 nR}{5\beta}\right)^{1/3} \tag{3.7}$$

where R is the universal gas constant. This fit yields a $\Theta_D = 232$ K. We added the T^5

term since the T^3 contribution is generally only applicable up to $\Theta_D/50 = 4.6$ K.[192] The resulting c is -5.9×10^{-7} mJ mol^{-1} K^{-6}, two orders of magnitude lower than the iron analogue.

3.5 Discussion

3.5.1 Ground state of CoSe

Despite the structural simplicity of CoSe, its magnetic ground state is less straightforward. Initial temperature dependence of magnetic susceptibility indicated a ferromagnetic transition at 10 K corroborated by powder neutron diffraction work.[61] When considering itinerant systems, it is often useful to evaluate Stoner's criterion for ferromagnetism in the system where the enhanced susceptibility χ_S is given by:[193]

$$\chi_S = \frac{\chi_P}{1 - F} = \frac{\chi_P}{1 - D_{band}(E_f)I_s/2} \tag{3.8}$$

where $D_{band}(E_f)$ is the density of states at the Fermi level, I_s is the Stoner factor for Co ($\sim$ 0.9 eV) divided by two to account for the two Co atoms per unit cell, and χ_P is Pauil paramagnetic susceptibility. The denominator allows us to formulate the Stoner's criterion such that $F = D_{band}(E_f)I_s/2$. We performed DFT calculations on CoSe which yielded $D_{band}(E_f) = 7.33$ states/eV for non-spin dependent calculations shown in Figure 3.10 Thus, this result leads to $F = 3.29 > 1$ which indicates that CoSe should have a ferromagnetic ground state.

The structurally related KCo_2Se_2 exhibits a ferromagnetic transition at approxi-

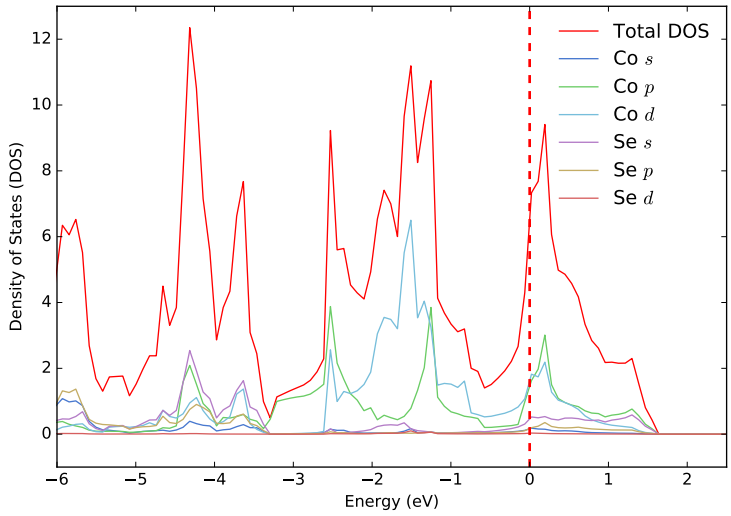

Fig. 3.10: Non-spin polarized density of states for CoSe decomposed for Co and Se atoms and their corresponding molecular orbitals.

mately 78 K measured on single crystals. The previous work used anisotropic single crystal measurements of magnetization to show that the magnetic moment resides completely in the *ab*-plane for the CoSe layers.[186] No neutron diffraction work has been reported to date on KCo_2Se_2, but the fairly large spacing between CoSe layers and anisotropic susceptibility indicates that the moment is likely in the *ab*-plane. When we remove the interlayer potassium ions and reduce the CoSe interlayer spacing from ~ 6.92 Å in KCo_2Se_2 to 5.33 Å in CoSe, we can consider how these adjacent planes may begin to interact.

Figure 3.4 showed that the magnetic susceptibility of CoSe displayed Curie-Weiss behavior above 100 K yielding a strongly negative Weiss constant, $\Theta_{CW} = -87.29$ K. Although CoSe is an itinerant electron system, we can minimally consider a square lattice Heisenberg model,[174,194] for which similar models have been applied extensively to the FeSe system,[195–198] to yield:

$$\Theta_{CW} = -\frac{(J_1 + J_2)}{k_B} \tag{3.9}$$

where J_1 and J_2 describe the nearest-neighbor and next-nearest-neighbor interactions on the square lattice, respectively. In this case we see that $J_1 + J_2 = 87.29$ K = 7.53 meV and that the exchanges should be antiferromagnetic based on the inverse susceptilibity data. At approximately 80 K, $\chi^{-1}(T)$ increases its slope so that the Weiss field changes to a positive value, possibly indicative of increasingly ferromagnetic fluctuations in this lower temperature regime.

Interestingly, specific heat, magnetization, AC susceptibility, and resistivity show no anomalous changes in near 80 K. Considering the ferromagnetic-like transition at 10 K shown in magnetic susceptibility measurements and the antiferromagnetic Weiss field at high temperature, we postulate that the ferromagnetic ordering at 78 K in KCo_2Se_2 is suppressed down to 10 K for CoSe.

The suppressed ordering may arise from geometric frustration, vacancies on the Co sites, or competing interactions between magnetic Co^{2+} ions. In the case of CoSe, we can eliminate two of these possibilities: vacancy ordering and geometric frustration. Elemental analysis from previous work showed that the percentage of Co vacancies did not exceed 2%, within error of that amount. Not enough to significantly suppress ordering. Geometric frustration occurs in systems where magnetic sublattices cannot arrange in a unique lowest energy ordered state, such as in an antiferromagnetic triangular lattice. CoSe contains a square lattice of cobalt atoms that cannot host this type of geometric frustration. Theoretical work, however, on square lattices have found frustration when

the nearest neighbor and next-nearest neighbor magnetic interactions compete. This has been termed interaction frustration.[72,199]

3.5.2 Anisotropy and Magnetic Direction

Our previous results from powder neutron diffraction indicated that the magnetic moments are aligned along the *c*-axis, contrary to the ordering in the related "122"-phase.[61] A possible reason for a difference in moment direction between the two systems could be could be due to closer CoSe layers in the CoSe than in KCo_2Se_2. To understand the anisotropy present in the system, we performed single crystal magnetization measurements similar to the work done on KCo_2Se_2 by Yang *et. al*.

In Figure 3.11a, we see that magnetic susceptibility in the *ab*-direction is about four to five times larger than the susceptibility in the *c*-direction. This suggests a fair amount of anisotropy, but not as large as in KCo_2Se_2, where there is an a order of magnitude difference between the two field directions.[186] Unexpectedly, the anisotropy in the field dependence of the magnetization for KCo_2Se_2 did not hold for CoSe (Figure 3.11b). We see that for both field directions the magnetization does not saturate up to 14 T and approaches a moment value of 0.1 μ_B. The itinerant nature of the magnetism leads to an unsaturated magnetization.

An important insight from these measurements is obtained by Arrott plot analysis. From Landau theory, we can expand the free energy, $F(H, T, M)$, of a magnetic system in the order parameter, M, corresponding to magnetization: $F = F_0 + aM^2 + bM^4$. Minimizing the free energy with respect to magnetization we arrive at:[193]

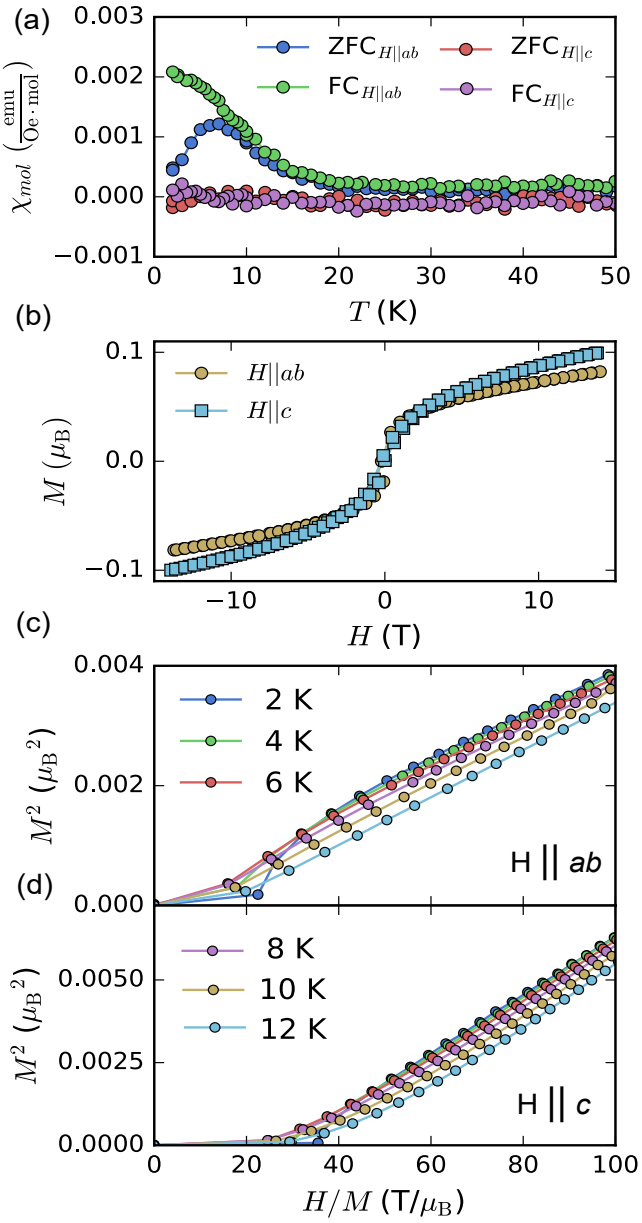

Fig. 3.11: Magnetic measurements of CoSe crystals mounted on a quartz paddle with orientations relative to the applied field direction as listed. a) Temperature dependent magnetic susceptibility for a 100 Oe field applied in two different orientations. b) Field dependent magnetization for both field orientations. c) Arrott plots constructed from $M(H)$ curves from 2 - 12 K for $H \parallel ab$, which indicate a ferromagnetic transiton within the 8 - 10 K range. d) Arrott plots constructed for $H \parallel c$-axis showing no spontaneous magnetization in the c-direction for any temperature.

$$M^2(T,H) = \frac{1}{b}\left(\frac{H}{M(T,H)}\right) - \frac{a}{b}\left(\frac{T-T_c}{T_c}\right) \tag{3.10}$$

We can plot M^2 vs. H/M, known as an Arrott plot, to obtain linear relationships between $M^2(H)$ curves at different set temperatures. From Equation 3.10, as the temperature approaches T_c, the $M^2(H)$ curves approach zero. Positive y-intercept values correspond to spontaneous magnetization at those temperatures. From Figure 3.11c for $H \parallel ab$-plane, the critical temperature appears to be in the 8 - 10 K range, as linear extrapolations of the $M^2(H)$ curves yield a zero y-intercept between 8 K and 10 K, which corresponds to transition temperature in the powder measurement. However, for $H \parallel c$-axis (Figure 3.11d), no $M^2(H)$ curves yield positive extrapolations back to the y-axis. Therefore, no spontaneous ferromagnetic moment orders along with c-axis.

The Arrott plot analysis matches previous reports for KCo_2Se_2, where the moment is claimed to lie solely in the ab-plane.[186] However, what causes the difference both the in ordering temperature and strength of the ferromagnetism between the two systems? The removal of potassium ions between the layers affects a number of factors: 1) cobalt oxidizes from $Co^{1.5+}$ in KCo_2Se_2 to Co^{2+} which means a removal of electron carriers, 2) CoSe layer distances are reduced from 6.92 Å in KCo_2Se_2 to 5.33 Å in CoSe which may cause more effective exchange between the moments in adjacent ab-planes, and 3) the Co-Co distance shrinks from 2.710(3) Å in KCo_2Se_2 to 2.6284(3) Å in CoSe, which causes more orbital overlap between Co centers.

3.5.3 FeSe vs. CoSe

Currently, Fe and Co are the only transition metals that have been able to form the anti-PbO structure which is closely related to the parent $ThCr_2Si_2$ structure. The

$ThCr_2Si_2$ hosts over 1,500 structures and a wide-range of physical phenomena. The anti-PbO phases are structurally simpler and can be used as the building blocks to systematically explore the physics within this structure type and, in general, metal square lattices.[63]

Unconventional superconductivity has emerged in the Fe*Ch* systems with the pairing mechanism for this phenomena still to be understood. With the close proximity of magnetism and superconductivity in the iron system, we need to understand the salient differences between CoSe and FeSe. Previous work directly compared the band structures of FeSe and CoSe and showed they differed by just a rigid band shift corresponding to the extra electron added by cobalt as compared to iron.[61] This shift moved the Fermi level away from the nesting of hole and electron pockets evident in the FeSe superconductor, which could to be key to realizing superconductivity in this system.

Since band structure measurements have yet to be conducted on CoSe, we can directly compare the results of recent studies on KCo_2Se_2 and AFe_ySe_2.[200,201] ARPES studies have shown that going from AFe_ySe_2 to KCo_2Se_2 (i.e. electron charge doping) changes the $3d$ orbital that contributes the most at the Fermi level. ARPES work on the AFe_ySe_2 series showed that the $3d_{xy}$ orbitals contribute the most at the Fermi level. The Se $4p_z$ orbitals also contribute to allow superexchange interactions. However, for KCo_2Se_2 the most significant orbital is the $3d_{x^2-y^2}$ which would change the interactions allowed between adjacent Co atoms.[189] This change in geometry of the d-orbital likely is the mechanism for tuning away superconductivity to frustrated magnetism in CoSe.

Extensive work has been performed to understand the magnetic fluctuations in FeSe which are integral in understanding the mechanism responsible for superconductivity in the iron-based superconductors. As previously stated, the interesting interplay of mag-

netism in this system seems to stem from the electronic instabilities that accompany the square lattice formation.[63] Recent inelastic neutron diffraction work and theoretical work has shown that within the FeSe layers there is strong frustration between different magnetic ordered states (stripe *vs.* Néel), which causes FeSe to not exhibit a true long-range magnetically order state.[52,197,198] The magnetic ordering in CoSe appears to suffer from similar frustration via the square lattice motif, although single crystal inelastic neutron spectroscopy measurements would shed further light on this hypothesis.

3.6 Conclusion

The synthesis of isostructural CoSe has allowed extensive characterization of the magnetic and transport properties of the system to understand its proximity to the iron-based superconducting analogues. Magnetic measurements have shown a transition reminiscent of ferromagnetism at 10 K with low applied fields that is fully suppressed at high fields. AC-susceptibility shows non-zero out-of-phase contributions, and such time dissipative magnetization below 10 K is indicative of a spin glass. Our more detailed analysis of the AC-susceptibility matches the behavior of CoSe to a spin glass, and we a possible explanation is the physics of interaction frustration present in square lattices.

Our Arrott plot analysis of the magnetization data reveals that the moment in CoSe lies within the *ab*-plane much like in related KCo_2Se_2. However, even if these two systems have similar anisotropy, the transition temperature is vastly different, having been suppressed from 78 K to 10 K in CoSe. Therefore, the amount of electron doping and density of states at the Fermi level can be used to tune the magnetic interactions in the Co

square sublattice.

Resistivity measurements indicate a metallic state in CoSe with no significant anisotropic magnetoresistance and no discontinuity at the 10 K transition. Heat capacity measurements indicate no observable transition at 10 K either, but low temperature analysis reveals an enhanced Sommerfeld coefficient due to strong spin fluctuations at low temperatures. The lack of a discernable transition within transport measurements further corroborates the glassy character at low temperatures due to interaction frustration. Comparing CoSe to FeSe, we now see that the nature of the *d*-orbital occupany near the Fermi level vastly tunes the ground state from a metal with weak and competing magnetic interactions (CoSe) to a superconductor (FeSe).

Future work on the CoSe system includes inelastic neutron spectroscopy to shed further light on the nature of the exchange interactions leading to interaction frustration. Chemical manipulation to charge dope CoSe would also be an important step in further expanding the phase diagram of these metal square lattices. There has been some previous cobalt doping studies on FeSe but the amount of substitution on cobalt has been limited to less than 20% due to phase stability with increased cobalt content.[157,158] However, the topochemical de-intercalation route should be able to expand the solid solution of cobalt-doped FeSe available to directly observe how superconductivity evolves into frustrated magnetism.

Chapter 4: Long-range magnetic order in transition metal doped (LiOH)FeSe by soft chemical design

The work described within this chapter was submitted to in *Physical Review Materials* Brandon Wilfong, Xiuquan Zhou, Navneeth Babra, Huafei Zheng, Johnpierre Paglione, Craig M. Brown, Jeffery Lynn, Keith M. Taddei and Efrain Rodriguez were contributing authors of the manuscript. B.W., X.Z., H.Z., and N.B. prepared the samples, B.W. and X.Z. performed MPMS measurements, B.W. collected resistivity data, X.Z., B.W., C.M.B., K.M.T, and J.W.L. collected the neutron powder diffraction data.

4.1 Introduction

The binary FeSe, with a superconducting critical temperature (T_c) of 8 K,[42] provides an excellent template to study exotic physical phenomena in iron-based superconductors due to its simple structure, ease of chemical manipulation and relatively high superconducting critical temperature. Amazingly, the T_c of FeSe can be improved significantly to 42-46 K from 8 K after intercalation,[46–48] 37 K with applied pressure,[49] or 65 K in the monolayer limit.[50] The well-studied intercalated compound ($Li_{1-x}Fe_xOH$)FeSe (T_c = 42-44 K) consists of a tetragonal layer of partially charged $Li_{1-x}Fe_xOH$ ($x \approx$ 0.1-0.2) between the FeSe layers. Such a structure is stabilized by the partial charge transfer due to

Fe doping on the Li site as well as hydrogen bonding from the LiOH layer to the Se atoms in the FeSe layers.[47,202,203] The Fe substitution in the insulating hydroxide layer not only plays a crucial role in the enhancement of T_c, but also can induce exotic physical phenomena such as coexistence of magnetic order and superconductivity.[80,81,124] Although many reports have shown signatures of magnetic order in this compound, there are no definitive signs to understand the true nature of its magnetism. The magnetic transition is intrinsic to the system with different reports attributing this transition to ferromagnetic ordering, canted antiferromagnetic ordering, and spin glassiness.[80,81,124,204,205] Despite their differences, all of these studies point toward the hydroxide layer as the source of the magnetic ordering.

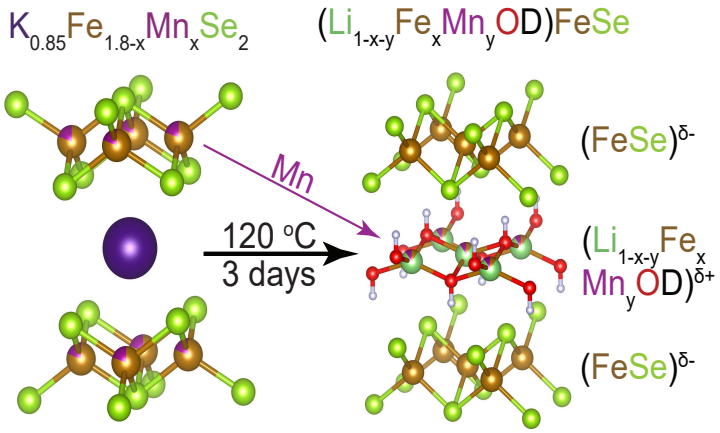

Fig. 4.1: Synthetic scheme and results of targeted $(Li_{1-x-y}Fe_xMn_yOD)FeSe$ by converting Mn-doped $KFe_{1.8-z}Mn_zSe_2$ hydrothermally.

In contrast to the uncertainties in $(Li_{1-x}Fe_xOH)FeSe$, there is a history of the observation of the coexistence of magnetism and superconductivity, mostly in rare-earth element containing compounds. The first examples of long-range magnetic order coexisting with superconductivity was observed in the ternary Chevrel phases RMo_6S_8 and RRh_4B_4

(R = lanthanide) where magnetic order arose from the lanthanide ion sublattice which was isolated from the superconducting sublattice. In these systems, both antiferromagnetism and ferromagnetism was observed coexisting with superconductivity depending on the lanthanide chosen for the magnetic sublattice.[206–209] The stabilization of magnetic order in these compounds was explained by dipolar electromagnetic interactions as the magnetic transition temperatures were below 1 K. Akin to these compounds were the later discovered borocarbides RNi_2B_2C where the magnetic ion sublattice now exhibits significant R-R exchange interactions pushing the magnetic phase transition much higher than in the Chevrel phases.[210–212] The discovery of superconductivity in the cuprate family offered a new avenue for exploration. In these compounds, magnetic ion sublattices isolated from the CuO planes show low ordering temperature similar to the previously mentioned systems which can coexist with superconductivity. However, interestingly in these compounds, Cu ions (S = 1/2) of the CuO planes exhibited antiferromagnetic insulator behavior, but this antiferromagnetic order could be suppressed to induce superconductivity upon doping.[27,213–215] The iron pnictide superconducting systems exhibit similar phenomena to the cuprate systems whereby magnetic order can coexist with superconductivity through an isolated magnetic ion sublattice and superconductivity arises from suppressing magnetic order of the iron pnictide layers through doping.[27,216–220] Unlike the related iron pnictide phases, FeSe exhibits no parent magnetic phase;[42,51] recent work has shown a high temperature nematic phase that precedes the superconducting phase.[221–223] Although no parent magnetically ordered phase exists, strong magnetic fluctuations have been observed in a wide range of temperatures in FeSe through neutron and NMR spectroscopy experiments.[51–54] Thus, the introduction of a magnetic spacer layer

between FeSe may help to further reveal the role magnetic fluctuations play in superconductivity in the Fe-chalcogenide systems.

In addition to its interesting magnetism, experimental evidence has shown that $(Li_{1-x}Fe_xOH)FeSe$ exhibits a Majorana Zero Mode (MZM) which plays a critical role in topological quantum computing applications.[224,225] Therefore, $(Li_{1-x}Fe_xOH)FeSe$ is a perfect system to study and understand the coexistence of physical phenomena for possible applications in functional materials as well as quantum computing.

Since all the aforementioned exotic phenomena emerge from the interactions between the superconducting $FeSe^{\delta-}$ and the insulating $(Li_{1-x}Fe_xOH)^{\delta+}$ layers, one may suggest to modify the hydroxide layer to induce new properties. Unfortunately, traditional solid-state reactions and methods will be insufficient to modify the solid solutions as these phases are metastable. Thus, we have developed a two-stage ion-exchange scheme to obtain $(Li_{1-x-y}Fe_xMn_yOD)FeSe$ by converting Mn-doped $K_{0.85}Fe_{1.8-z}Mn_zSe_2$ hydrothermally. We manipulate the chemistry of the hydroxide layer in $(Li_{1-x}Fe_xOD)FeSe$ through manganese doping to tune the magnetic properties without significantly altering the superconductivity in the system (Fig. 4.1). The addition of manganese to supplant Li and Fe in the tetrahedral hydroxide layer increases the effective spin and therefore the effective moment of layer to observe long range magnetic order.

4.2 Methods

4.2.1 Synthesis

The synthesis of $(Li_{1-x-y}Fe_xMn_yOD)FeSe$ (M = Mn, Co, Ni, Cu, Zn) single crystals was perfomed via a two-step ion-exchange route similar to previous works.[79,82,226] High purity metallic K (Alfa Aesar, 99.5%), M granules (Alfa Aesar, 99.98%), Fe granules (Alfa Aesar, 99.98%), and Se shots (Alfa Aesar, 99.999%) were used as raw materials.

In order to incorporate transition metal doping, single crystals of $K_{0.85}Fe_{1.8-z}Mn_zSe_2$ were synthesized through a self-flux route with elemental mixture of K:Fe:Mn:Se in two nominal ratios of 0.85:(1.62/1.44):(0.18/0.36):2 were mixed in an argon glovebox sealed under vacuum in a double quartz ampoule. The quartz tubes were slowly heated at 50 °C/hr to 1050 °C, held at 1050 °C to ensure a congruent melt, slowly cooled down to 550 °C at a rate of 5 °C/hr, and ended with natural cooling to room temperature. This method routinely produced 3 x 3 mm^2 plate-like single crystals. The hydrothermal ion-exchange were performed in 100 mL stainless steel autoclaves lined with Teflon cups. For each batch, select single crystals of $K_{0.85}Fe_{1.8-z}Mn_zSe_2$ with average total mass of approximately 2 grams, 1.2 mmol of selenourea (Sigma Aldritch, 98%), 13 mmols of iron granules (Alfa Aesar, 99.98%), 1.2 mmol of tin granules (used to regulate pH), 0.31 moles LiOH (anhydrous, Alfa Aesar, 98%), and 40 mL of D_2O (Cambridge Isotope, 99.9%) were loaded into the autoclave and purged under argon flow for 2 minutes before being tightly sealed. Each autoclave was heated to 120 °C and held for 72 hours in a convection oven. Silver plate-like single crystals were recovered by washing away excess powders

with D_2O, excess iron granules were easily recovered with a magnetic bar. Crystals were dried under vacuum overnight and stored in an Ar filled glovebox.

4.2.2 Magnetic and transport measurements

All magnetic property measurements were carried out using a Quantum Design Magnetic Susceptibility Measurement System (MPMS-3) on powders and single crystals of $(Li_{1-x-y}Fe_xMn_yOD)FeSe$ samples. Zero-field-cooled (ZFC) and field-cooled (FC) measurements were taken from 1.8 to 300 K with various applied direct current (DC) magnetic fields. Isothermal magnetization measurements were taken from H = ± 7 T at numerous temperatures to probe the magnetic and superconducting state. Electrical transport measurements were performed on a 9 T Quantum Design Physical Property Measurement System (PPMS-9T) with temperatures from 1.8 to 300 K and fields up to 9 T using a four-probe technique with current applied across the *ab*-plane due to the lamellar nature of the single crystals. Heat transport measurements were performed on a 14 T Quantum Design Physical Property Measurement System (PPMS-14T) over the range of 1.8 to 60 K using the relaxation technique.[143,179,180]

4.2.3 X-ray diffraction measurements

Laboratory powder x-ray diffraction (PXRD) was collected using a Bruker D8 X-ray diffractometer with Cu Kα radiation (λ = 1.5406 Å, step size = 0.020°, 2θ = 5 - 90°) for phase identification. In order to aid in structural refinements associated with the $(Li_{1-x-y}Fe_xMn_yOD)FeSe$ system, as three different elements occupy the same crystallo-

graphic site, high resolution synchrotron X-ray diffraction was performed on powders of ground single crystals at Beamline 11-BM at the Advanced Photon Source at Argonne National Lab. Ground powders of single crystals were packed in 0.4 mm Kapton capillary tubes and sealed with epoxy. Diffraction data was collected between 0.5° and 46° with a step size of 0.0001° using a constant wavelength λ = 0.413964 Å(30 keV) at 100 K. Rietveld refinements were performed using the TOPAS software suite.[126]

4.2.4 Neutron diffraction measurements

Neutron powder diffraction (NPD) data was collected at the NIST Center for Neutron Research (NCNR) BT-1 High Resolution Powder Diffractometer and Oak Ridge National Lab High Flux Isotope Reactor (HFIR) HB-2A.[227] Powder samples of ground single crystals of ($Li_{1-x-y}Fe_xMn_yOD$)FeSe were loaded into vanadium cans under helium exchange gas and loaded into a closed-cycle refrigerator (BT-1) or three-sample changer in 70mm Orange Cryostat (HB-2A). Low temperature diffraction data was collected at 2 K and 9 K and high temperatures at 50 K, for direct comparison in attempts to find magnetic satellite reflections, with Cu(311) (λ = 1.54 Å) at BT-1 and Ge(115) (λ = 1.54 Å) at HB-2A. Rietveld refinements were performed using the TOPAS software suite.[126] In order to search for weak magnetic reflection, high intensity but coarse resolution diffraction measurements were performed on single crystals and ground single crystal powder on the BT-7 spectrometer at the NCNR using the position sensitive detector (PSD) with PG (002) (λ = 2.359 Å) in a range of temperature from 2 - 50 K to search for magnetic transitions inside the superconducting regime.

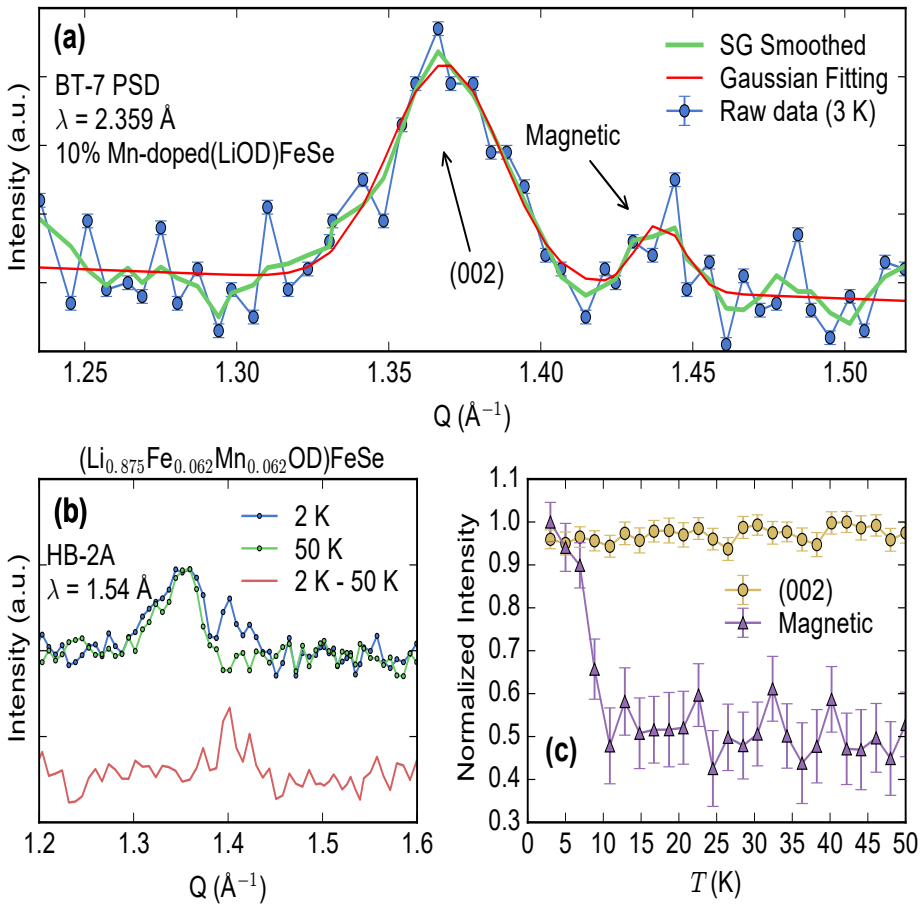

Fig. 4.2: Powder neutron diffraction data collected at BT-7 and HB-2A. a) Powder neutron diffraction data collected at 3 K at BT-7 using the PSD on a nominally 10% Mn doped LiODFeSe sample of the (002) reflection showing a clear well-resolved magnetic peak proximate to the (002) reflection. This data smoothed using a Savitzsky-Golay filter and subsequently fit using a two-Gaussian model to extract temperature dependence. b) Powder neutron diffraction data on $(Li_{0.875(2)}Fe_{0.062(3)}Mn_{0.062(3)}OD)FeSe$ at HB-2A showing the (002) reflection and magnetic peak at 2 K which is absent in the 50 K data. c) Temperature dependence on the integrated intensity of the two-Gaussian model on the data presented in a) showing a sharp decrease in the magnetic peak integrated intensity up to 10 K and temperature independence above 10 K. Uncertainties represent one standard deviation.

4.3 Evidence for long range magnetic order

To date, all previous powder neutron diffraction data on (LiOD)FeSe samples made via the bottom-up synthesis and ion-exchange method do not exhibit observable long-

range magnetic order.[48,80,82,124,228] Small angle neutron scattering did reveal a characteristic ferromagnetic scattering below 12 K with a clear vortex scattering peak observed at Q = 0.0077 Å^{-1} under a 0.4 T applied field.[81] Two more recent works on single crystals of the (LiOD)FeSe system via the ion-exchange method used inelastic neutron spectroscopy to investigate spin excitations below the superconducting temperature to reveal their importance in driving high critical temperatures in these compounds.[226,229]

We have performed neutron powder diffraction on Mn-doped (LiOD)FeSe to observe long-range magnetic order. The results are shown in Figure 4.2 which span the use of two diffraction instruments and two different compositions of the Mn-doped (LiOD)FeSe system. To start, Figure 4.2b shows the low Q data accessible from the powder neutron diffraction data collected at HB-2A on Mn-doped (LiOD)FeSe and presented in Figure 4.3b/c in full. At Q = 1.41 Å^{-1}, d = 4.45 Å, a pronounced peak is observed at 2 K which is absent at 50 K; this peak is proximate to the nuclear (002) reflection but it was well resolved. This is the first time a satellite reflection has been observed in neutron diffraction for the (LiOD)FeSe system indicating the existence of some form of long-range order. We attribute this to the larger magnetic moment of Mn^{2+} (S = 5/2) compared to Fe^{2+} (S = 2). As the magnetic peak appears distinct from the nuclear peaks, we can conclude the ordering in the system must be of the antiferromagnetic or ferrimagnetic type. Unfortunately, we observe only one magnetic peak in the data, most likely due to the small magnetic moment of the system or the small magnetic form factor in this compound. The full magnetic structure cannot be solved currently.

In order to further understand how this magnetic peak behaved as a function of temperature, additional powder neutron diffraction data was collected on ground single

crystals of nominally 10% Mn-doped (LiOD)FeSe samples at BT-7 using the PSD. For these measurements, the (002) reflection was identified and measured as a function of temperature with a ±0.2 $Å^{-1}$ window of collection using the PSD. Thus, the satellite reflection proximate to the (002) reflection observed in HB-2A data could be recorded concurrently. The raw data collected using the PSD at 3 K is shown in Figure 4.2a displayed with a two-Gaussian model fit to the smoothed data using a third-order Savitzsky-Golay filter due to the coarse resolution of the raw data. The raw data and two-Gaussian fit show two well resolved peaks, one for the (002) reflection at $Q = 1.37$ $Å^{-1}$ and one for the magnetic peak at $Q = 1.44$ $Å^{-1}$, in close agreement to the HB-2A data. The slight discrepancy is likely due to crystallographic differences in the compounds. Figure 4.2c shows the temperature evolution of the normalized integrated intensities calculated by the two-Gaussian model corresponding to the (002) reflection and magnetic peak. It is observed that the (002) reflection is temperature independent while the magnetic peak shows a sharp decrease in integrated intensity above 10 K in close agreement to the ordering temperature observed in magnetization and heat capacity data. We can conclude that the long-range magnetic ordering observed is intrinsic to the system with an ordering temperature around 9 K and has been observed for the first time by targeted design of the hydroxide layer in (LiOD)FeSe.

Futhermore, in the Mn-doped (LiOD)FeSe we have observed a high superconducting critical temperature paired with a relatively high magnetic transition temperature compared to rare-earth containing phases. This arises through similar means to the previously mentioned Chevrel, borocarbide, copper and iron-based systems whereby the magnetic sublattice and superconducting sublattice are isolated from another. However, we have

done so without the need for rare-earth ions. Interestingly, in this system the addition of transition metal doping in the hydroxide layer both induces magnetic order as well as charge dopes the FeSe layers significantly raising the critical temperature of the compound. Thus, transition metal doped (LiOH)FeSe offers a tremendous platform for exploration of the role magnetism plays in stabilizing high temperature superconducitivity in the iron chalcogenides and for potential use in next generation devices.

4.4 Hydrothermal synthesis and crystallographic results

As shown in Fig.4.1, we first prepare precursors of $K_{0.85}Fe_{1.8-z}Mn_zSe_2$ with 10% and 20% nominal Mn doping level using direct elemental reactions from high-temperature. Our XRD analysis of $K_{0.85}Fe_{1.8-z}Mn_zSe_2$ show significant different lattice constants compared to $K_{0.85}Fe_{1.8}Se_2$, indicating replacement of Fe in the FeSe layer, presented in Table 4.1

	10% Nominal Doping		20% Nominal Doping	
Transition Metal	a lattice parameter (Å)	c lattice parameter (Å)	a lattice parameter (Å)	c lattice parameter (Å)
Mn	3.8963	14.1434	3.8937	14.1513
Fe	3.8341	14.2360	3.8341	14.2360
Co	3.8814	14.1640	3.8892	14.1088
Ni	3.8817	14.0735	3.8790	14.1187
Cu	3.9001	14.0957	3.9091	14.1177
Zn	3.8939	14.0932	3.9061	14.0323

Tab. 4.1: Refined lattice parameters of $K_{0.85}Fe_{1.8-x}M_xSe_2$ M = (Mn, Co, Ni, Cu, Zn) starting materials made via a high temperature self flux reactions from the corresponding elements. The 10% and 20% nominal doping come from the stoichiometric additons of each element to the growth. The reported lattice parameters for the Fe (un-doped) version come from a similarly targeted stoichiometric compound of $K_{0.85}Fe_{1.9}Se_2$ via Shoemaker, D.P., *et al* Phys. Rev. B 86.18 (2012): 184511.

Obtained small single crystals of these precursors are used to exchange K with LiOH hydrothermally as described in our earlier work[82] For such conversion, it is crucial to include additional Fe powders and Sn metal plates in the autoclave to avoid formation

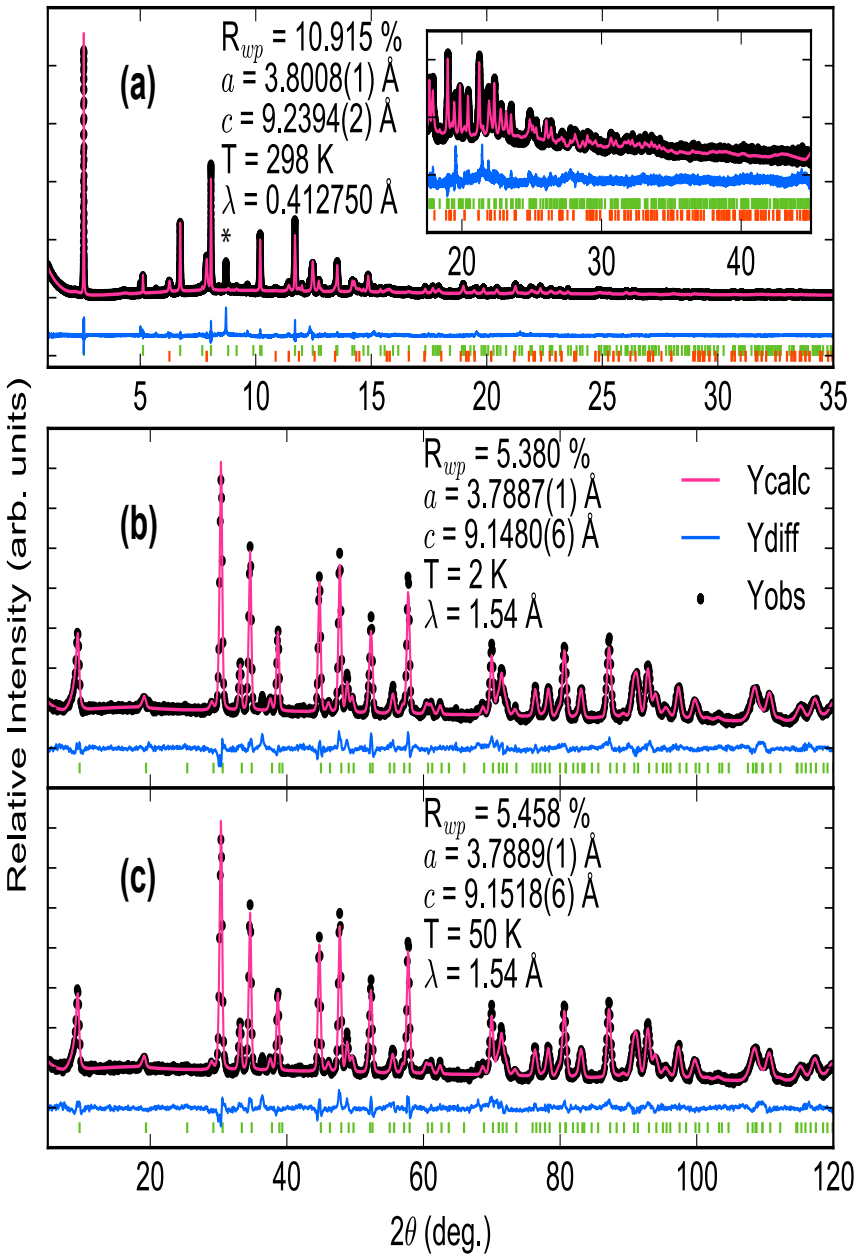

Fig. 4.3: a) High resolution synchrotron PXRD patterns for ($Li_{1-x-y}Fe_xMn_yOD$)FeSe collected at room temperature, b) and c) show NPD data for ($Li_{1-x-y}Fe_xMn_yOD$)FeSe at 2 K and 50 K respectively. Green tick marks represent the targeted tetragonal layered phase and orange tick marks represent impurity selenium. These are shown below the calculated, observed, and differences curves from Rietveld analysis. The asterisk represent a single observable impurity peak that does not match any observable peak in the NPD data.

of iron oxides and complete destruction of superconductivity. In this scheme, because the transition metal dopant, M, prefers covalent coordination with OH^- group, they are driven from the FeSe layer of the $K_{0.85}Fe_{1.8-z}M_zSe_2$ to replace Li in the LiOH layer.[48,230] This is because the hard Lewis acid, Mn^{2+}, prefers coordination with the hard Lewis base of OH^- as opposed to the soft base S^{2-}; this prevents the formation of impurity manganese sulfides. The vacancies in the FeSe layer are then supplemented by Fe^{2+} from the solution. After the hydrothermal conversion, we obtain the products in both powder and single crystal forms.

After synthesis, we needed to determine the precise composition and crystallographic occupancy of all dopants. There has been multiple works to date on similar transition metal doping in the (LiOH)FeSe system, but none have been able to quantify the crystallographic location of the transition metal dopant.[231–234] The location of the transition metal dopant is incredibly important in the realization of different physical properties as superconductivity in the iron chalcogenide systems is very sensitive to doping.[44,48,230] To identify the crystallographic location of the Mn doping, we use extensive x-ray and neutron diffraction. Since, X-ray form factors of Mn are very close to Fe, it is extremely difficult to obtain their site occupancy using regular X-ray diffraction whereas elemental analysis methods are not able to tell where Mn is located nor whether they are from impurities. Therefore, high-resolution synchrotron powder x-ray diffraction (PXRD) has been paired with neutron powder diffraction (NPD) to fully understand the composition of these materials. Fig. 4.3 shows powder x-ray diffraction and powder neutron diffraction data for $(Li_{1-x-y}Fe_xMn_yOD)FeSe$. High resolution synchrotron PXRD allows for high quality Rietveld refinements of crystallographic structural parameters, Fe

vacancies in the FeSe layer and total transition metal (M^* = Fe + Mn) occupancies in the LiOH layer; however it does not allow for discrimination of transition metal dopants on the same crystallographic site. Thus, NPD complements synchrotron PXRD for high contrast between Fe and other transition metals occupying the same site.

Figure 4.3a shows powder x-ray diffraction data and corresponding Rietveld fit for $(Li_{1-x-y}Fe_xMn_yOD)FeSe$. Refinements with PXRD were limited to occupation of total transition metal (M^*) doping in the hydroxide layer as well as total transition metal in the FeSe layer yielding a formula: $(Li_{1-x}M^*_xOD)M_ySe$. Rietveld refinements of the powder x-ray diffraction yielded a composition of $(Li_{0.875(2)}M^*_{0.125(2)}OD)MSe$ with lattice parameters a = 3.8008(1) Å and c = 9.2394(2) Å which is in close agreement with previous works.[47,48,81,82]

$(Li_{0.875(2)}Fe_{0.062(3)}Mn_{0.062(3)}OD)FeSe$ (298 K, PXRD), *P4/nmm*, R_{wp} = 8.506%						
a = 3.8008(1) Å,c = 9.23949(2) Å						
atom	Site	x	y	z	Occ.	U_{iso} (Å^2)
Li/Fe1/Mn1	2b	0	0.5	0	0.875(2)/0.062(3)/0.062(3)	0.0246(2)
Fe2	2a	0.5	0.5	0	0.993(4)	0.0252(2)
Se1	2c	0	0.5	0.1603(1)	1	0.011(4)
O1	2c	0.5	0	0.4249(4)	1	0.002(6)
Fe-Se (Å)	Se-Fe-Se (°)	Se-Fe-Se (°)	Fe-Fe (Å)			
2.409(8)	112.21(6)	104.11(1)	2.687(8)			
$(Li_{0.875(2)}Fe_{0.062(3)}Mn_{0.062(3)}OD)FeSe$ (2 K, NPD), *P4/nmm*, R_{wp} = 5.380%						
a = 3.7887(1) Å,c = 9.1480(6) Å						
atom	Site	x	y	z	Occ.	U_{iso} (Å^2)
Li/Fe1/Mn1	2b	0	0.5	0	0.875(2)/0.062(3)/0.062(3)	0.012(3)
Fe2	2a	0.5	0.5	0	0.993(4)	0.0041(4)
Se1	2c	0	0.5	0.1624(2)	1	0.0031(5)
O1	2c	0.5	0	0.4271(4)	1	0.0147(9)
D1	2c	0.5	0	0.3267(8)	1	0.004(1)
Fe-Se (Å)	Se-Fe-Se (°)	Se-Fe-Se (°)	Fe-Fe (Å)			
2.407(5)	112.38(6)	103.78(6)	2.679(1)			

Tab. 4.2: Structural parameters for ground single crystals of $(Li_{0.875(2)}Fe_{0.062(3)}Mn_{0.062(3)}OD)FeSe$. Structures are for room temperature PXRD data and 3 K NPD data. All relevant bond angles and distances from the refinements are given. Standard uncertainties given in parantheses indicate one standard deviation.

These refined structural and occupation values were then used as the starting model for the NPD. As mentioned, NPD was pivotal in determining the different transition metal dopants in the hydroxide layer and FeSe layers. Figure 4.3b,c show the NPD and corresponding Rietveld analysis for $(Li_{0.875(2)}M_{0.125(2)}OD)MSe$ at 2 and 50 K respectively. Subsequent Rietveld analysis yielded a composition of $(Li_{0.875(2)}Fe_{0.062(3)}Mn_{0.062(3)}OD)FeSe$, full results shown in Table 4.2. Interestingly, it was found that all the manganese dopant migrates to the hydroxide layer with no refineable amount of manganese in the FeSe layer. It is understood that dopants in the FeSe layer destroys superconductivity,[48,82] so this reaction scheme allows for the superconductivity to be marginally altered while the magnetic layer can be manipulated.

4.5 Magnetic and transport properties

We have measured magnetic susceptibility at various applied fields and isothermal magnetization at 2 K and 50 K on a single crystal of $(Li_{0.875(2)}Fe_{0.062(3)}Mn_{0.062(3)}OD)FeSe$. Figure 4.4a/b show temperature dependent magnetic susceptibility, corrected for demagnetization factors of a two-dimensional plate,[235] with applied field applied parallel to the crystallographic *ab*-plane and *c*-axis respectively. Interestingly, the superconducting onset temperature is 25 K which is significantly lower than in the un-doped system. The highest observed shielding fraction after correction for demagnetization factors is $\sim 25\%$ which may indicate non-bulk superconductivity in this system. Within the (LiOH)FeSe system, many factors that affect the observable superconducting temperature: lattice parameters, transition metal concentration in the hydroxide and selenide layers, and struc-

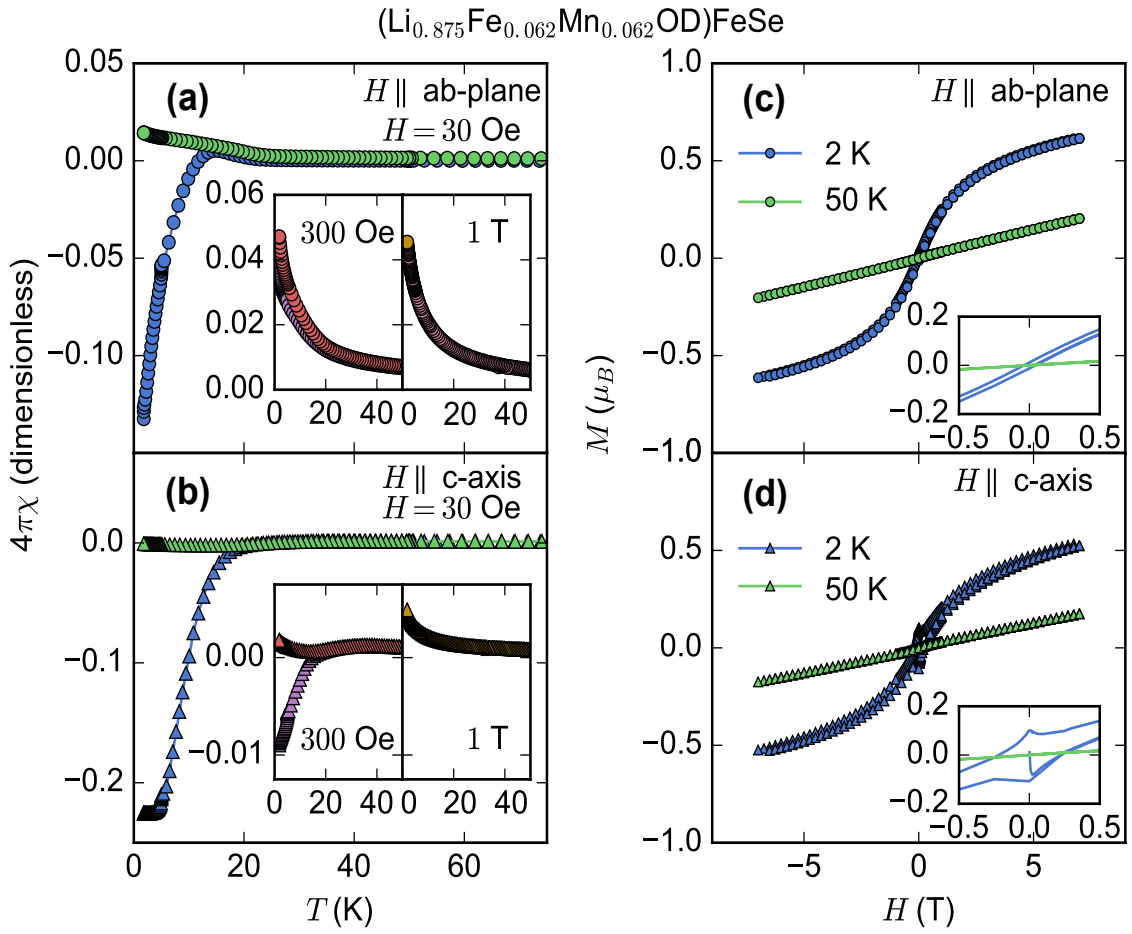

Fig. 4.4: Magnetic property measurements on an aligned single crystal of $(Li_{0.875(2)}Fe_{0.062(3)}Mn_{0.062(3)}OD)FeSe$. a)/b) Magnetic susceptibility data at various applied fields, aligned parallel to the crystallographic *ab*-plane and *c*-axis respectively, showing a superconducting transition at 25 K but no second magnetic transition at lower temperature. c)/d) Isothermal magnetization at 2 K and 50 K, with the same orientation convention, showing magnetic hysteretic behavior superimposed on a superconducting signal at 2 K and paramagnetic behavior at 50 K. Note: (1 Oe = (1000/4π) A/m)

tural homogeneity.[48,82,203]

Unlike previous reports,[80,124] no magnetic transition is observed in the magnetic susceptibility even at higher applied fields. Interestingly, the only reports to show a transition in magnetic susceptibility below the superconducting transition are on powder samples via hydrothermal method.[80,82,124,236] Single crystals samples from the ion-exchange hydrothermal method fail to show the secondary magnetic transition below the observed

superconducting transition.[82,203,237–240] We hypothesize that sample uniformity in doping and structure caused by the different reaction conditions is likely the cause of these property differences. In the bottom-up synthesis, FeSe and LiOH layers are formed in-situ contrary to the ion-exchange method which requires the removal of interlayer ions before replacing with LiOH extended solid which would lead to more structural and compositional variation.

We observe strong anisostropy in the magnetic susceptibility. Fields applied parallel to the crystallographic *ab*-plane have a much stronger effect on suppressing the superconducting transition than fields applied parallel to the *c*-axis as shown in the insets of Figure 4.4a/b. This is consistent with previous reports.[79,203] and the observed transition is suppressed at relatively low fields, 300 Oe. The supression is due to the superconducting irreversibility temperature which is unique in these samples due to the very large vortex liquid region caused by extremely high anisotropy and two-dimensionality.[238]

We see an effect of underlying magnetic order is observable in isothermal magnetization measurements shown in Figure 4.4c/d at 2 K and 50 K. For both field orientations, magnetization as a function of fields shows a superconducting signal superimposed on a weak magnetic background. Mirroring the behavior of magnetic susceptibility, the Meissner shielding is more clearly observable at low fields for the field applied parallel to the *c*-axis as compared to field applied parallel to the *ab*-plane. Again, this fast suppression of Meissner shielding could be due to true anisotropy, the filamentary nature of the superconductivity, or the effects of vortex dynamics in the sample. At higher temperatures, 50 K, the magnetic and superconducting signals are absent and paramagnetic behavior is observed. This paired with x-ray and neutron diffraction data shows that the magnetic

signal is intrinsic to the system.

Electrical and thermal transport measurements shed more light on the superconducting and magnetic order in this system. Temperature dependence of electrical resistivity on a single crystal of $(Li_{0.875(2)}Fe_{0.062(3)}Mn_{0.062(3)}OD)FeSe$, shown in Figure 4.5a, shows a sharp superconducting transition at 41 K in zero field. With field applied parallel to the crystallographic c-axis, it is observed that the superconducting transition onset is not changed, but the transition width in greatly increased at higher applied fields. This transition width broadening matches previous reports for this system. Specifically where this behavior has been justified by strong vortex flow as well as a wide temperature range for vortex liquid behavior due to anisotropy and two-dimensionality.[79,203,238,240–243]

The superconducting onset temperature measured by resistivity is much higher than in the same crystal measured in magnetic susceptibility. This phenomena was observed in previous works as well and can be attributed to the vortex dynamics in the system.[203,239,240,243] The residual resistivity ratio $\rho(300\text{K})/\rho(T_c)$ for the sample presented is ~ 25 which is higher than in previous reports.[203,240–242] The observed normal state behavior is non-linear which has been demonstrated in previous works.[203,240–242] and has been attributed to over-doping in the sulfide analogue.[87]

Due to the very high critical field in these samples,[79], heat capacity measurements were employed to evaluate the effect magnetic ordering has within the superconducting regime. Heat capacity measurements on this system fail to show anomalous behavior around the superconducting transition.[124,204,244] Temperature dependence of heat capacity at various applied fields shown in Figure 4.5b shows similar behavior. No anomaly is observed at the superconducting transition temperature, however; a magnetic transition

is observed at ~ 9 K in zero applied field parallel to the crystallographic c-axis. In these previous reports,[124,204,244] the magnetic transition was suppressed at high applied fields which was justified by antiferromagnetic or spin-glass ordering in the system. However, these measurements were done on samples made via the bottom-up hydrothermal synthesis, which behave differently than those produced via the ion-exchange method. To that end, the magnetic transition shown in Figure 4.5b shows slight temperature suppression at 14 T, but is still clearly observable. We can conclude that the magnetic order in this system is of an antiferromagnetic or ferrimagnetic nature when combined with the observation of satellite reflection in neutron diffraction.

To calculate the magnetic contribution to the heat capacity at low temperatures, the temperature dependent C_p/T data at zero applied field was fit to a third order polynomial above 20 K. This fitting was then extrapolated to low temperatures and subsequently subtracted from the raw data below 20 K. The remainder was then integrated to yield ΔS as shown in Figure 4.5c as a function of temperature. The change in entropy sharply increases up to 12 K before leveling off at a value of 0.38(8) J/(mol·K), which is significantly lower than the expectation for a free electron spin. The entropy change through a magnetic transition is defined as $\Delta S = cR\ln(2J + 1)$, where c is the concentration of magnetic ions in the system and R is the ideal gas constant. Our compositional analysis of single crystals of $(Li_{0.875(2)}Fe_{0.062(3)}Mn_{0.062(3)}OD)FeSe$ showed a concentration of magnetic ions in the hydroxide layer as $c = 0.125$, yielding an effective $J = 0.22(6)$ for the system and effective moment $\mu_{\text{eff}} = 1.05(2)\ \mu_B$, spin-only.

The expected spin values for Fe^{2+} and Mn^{2+} in tetrahedral coordination (quenched orbital angular momentum) are 2 and 5/2 respectively. These values are much larger than

the observed 0.22(6) from entropy measurements. Previous reports observed similar behavior and concluded that this spin underestimation was due to spin-glassy character of the magnetism in the hydroxide layer.[204] The robustness of the observed transition up to 14 T trends away from a spin-glass description for the magnetic behavior but spin glassiness cannot be ruled out.[124,139,204] In-depth analysis at the atomic level through imaging or spectroscopy would be useful to understand how the dilute magnetic ions in the hydroxide layer order to from long range correlations.

4.6 Effect of other transition metal dopants

We have been able to synthesize nominally 10 and 20% transition metal doped (LiOD)FeSe using the same two-step soft chemistry hydrothermal reaction scheme described above for the Mn-doped system. In this scheme single crystals of $K_{0.85}Fe_{1.8-z}M_zSe_2$ M = (Mn, Co, Ni, Cu, Zn) were converted to $(Li_{1-x-y}Fe_xM_yOD)Fe_{1-z}M_zSe$ where different transition metal dopants in the $K_{0.85}Fe_{1.8-z}M_zSe_2$ behaved differently when converting to the desired product. We have performed high resolution powder x-ray diffraction and neutron powder diffraction on 20% Co, Ni, Cu, and Zn samples in order to understand how the different transition metals behave in our hydrothermal reaction scheme. These results are presenting in Figures 4.6, 4.9, 4.7, 4.8. Full details of the crystallographic data is shown in Tables 4.3, 4.4, 4.5, 4.6. Based on our refinement results, it is surprising to find that only Mn and Co replace Li at the Li site as intended. For Ni (Fig. 4.6), about 2% still remains in the FeSe layer while for Cu and Zn, no doping is present in neither FeSe nor LiOH layer (Fig. 4.8, 4.7). For Cu and Zn, as a softer cations, they prefer co-

ordination to softer anions such as Se compared to O. Therefore, significant amount of starting $K_{0.85}Fe_{1.44}Cu_{0.36}Se_2$ and ZnSe impurity is present in the product for Cu and Zn doped samples respectively (Fig. 4.7 4.8). The case of Ni doping is a bit more difficult to explain - it is likely that the Ni in the starting materials converts to some stable soluble product in solution as opposed to exchanging for Li in the LiOH layer and is then removed when the product is recovered from the hydrothermal autoclave.

$(Li_{0.842(1)}Fe_{0.135(4)}Co_{0.02(3)}OD)Fe_{0.950(2)}Se$ (298 K, PXRD), *P4/nmm*, R_{wp} = 7.862%						
a = 3.7783(9) Å,c = 9.3065(2) Å						
atom	Site	x	y	z	Occ.	U_{iso} (Å^2)
Li/Fe1/Co1	2b	0	0.5	0	0.842(1)/0.135(4)/0.02(3)	0.0257(1)
Fe2	2a	0.5	0.5	0	0.950(2)	0.0130(2)
Se1	2c	0	0.5	0.1593(4)	1	0.014(5)
O1	2c	0.5	0	0.4246(1)	1	0.007(5)
Fe-Se (Å)	Se-Fe-Se (°)	Se-Fe-Se (°)	Fe-Fe (Å)			
2.401(7)	112.41(2)	103.73(7)	2.671(7)			
$(Li_{0.842(1)}Fe_{0.135(4)}Co_{0.02(3)}OD)Fe_{0.950(2)}Se$ (2 K, NPD, *P4/nmm*, R_{wp} = 4.606%						
a = 3.7887(1) Å,c = 9.1480(6) Å						
atom	Site	x	y	z	Occ.	U_{iso} (Å^2)
Li/Fe1/Co1	2b	0	0.5	0	0.842(1)/0.135(4)/0.02(3)	0.012(9)
Fe2	2a	0.5	0.5	0	0.950(2)	0.0051(1)
Se1	2c	0	0.5	0.1566(4)	1	0.0019(3)
O1	2c	0.5	0	0.4162(6)	1	0.0119(6)
D1	2c	0.5	0	0.325(1)	1	0.003(1)
Fe-Se (Å)	Se-Fe-Se (°)	Se-Fe-Se (°)	Fe-Fe (Å)			
2.372(8)	111.58(4)	105.32(3)	2.667(1)			

Tab. 4.3: Structural parameters for ground single crystals of $(Li_{0.842(1)}Fe_{0.135(4)}Co_{0.02(3)}OD)Fe_{0.950(2)}Se$. Structures are for room temperature PXRD data and 3 K NPD data. All relevant bond angles and distances from the refinements are given. Standard uncertainties given in parantheses indicate one standard deviation.

As one may expect the location of the transition metal dopant, whether it remains in the FeSe layer or migrates to the LiOH layer, has a huge effect on the superconducting and magnetic properties. We have shown that Co doping behaves similarly to Mn doping where all the Co ions migrate to the LiOH layer leaving the FeSe layer un-doped; although the ratio of Co replacement of Li compared to Fe is much smaller than in the

$(Li_{0.822(1)}Fe_{0.176(3)}OD)Fe_{0.964(3)}Ni_{0.020(1)}Se$ (298 K, PXRD), *P4/nmm*, R_{wp} = 7.778%						
a = 3.7783(9) Å,c = 9.3065(2) Å						
atom	Site	x	y	z	Occ.	U_{iso} (Å^2)
Li/Fe1	2b	0	0.5	0	0.822(1)/0.176(3)	0.0273(4)
Fe2/Ni2	2a	0.5	0.5	0	0.964(3)/0.020(1)	0.0163(2)
Se1	2c	0	0.5	0.1608(1)	1	0.011(2)
O1	2c	0.5	0	0.4253(2)	1	0.002(4)
Fe-Se (Å)	Se-Fe-Se (°)	Se-Fe-Se (°)	Fe-Fe (Å)			
2.412(6)	112.19(2)	104.15(1)	2.691(5)			
$(Li_{0.8229(1)}Fe_{0.176(3)}OD)Fe_{0.964(3)}Ni_{0.020(1)}Se$ (2 K, NPD, *P4/nmm*, R_{wp} = 3.455%						
a = 3.7887(1) Å,c = 9.1480(6) Å						
atom	Site	x	y	z	Occ.	U_{iso} (Å^2)
Li/Fe1	2b	0	0.5	0	0.822(1)/0.176(3)	0.006(5)
Fe2/Ni2	2a	0.5	0.5	0	0.964(3)/0.020(1)	0.0372(3)
Se1	2c	0	0.5	0.1623(2)	1	0.0060(3)
O1	2c	0.5	0	0.4242(4)	1	0.0118(7)
D1	2c	0.5	0	0.3229(7)	1	0.003(1)
Fe-Se (Å)	Se-Fe-Se (°)	Se-Fe-Se (°)	Fe-Fe (Å)			
2.409(1)	112.20(4)	104.13(8)	2.687(9)			

Tab. 4.4: Structural parameters for ground single crystals of $Li_{0.822(1)}Fe_{0.176(3)}OD)Fe_{0.964(3)}Ni_{0.020(1)}Se$. Structures are for room temperature PXRD data and 3 K NPD data. All relevant bond angles and distances from the refinements are given. Standard uncertainties given in parantheses indicate one standard deviation.

Mn-doped case. The retention of an undoped FeSe layer has been shown in previous works to be integral in retaining the superconducting properties of FeSe layers.[44] Interestingly though, Co doping does not result in observed long range magnetic order through neutron diffraction measurements. Magnetic susceptibility measurements and isothermal magnetization measurements presented in Figure 4.13 show a clear superconducting transition at 30 K wtih a ferromagnetic signal superimposed on Meissner shielding signal at 2 K. The saturation value of the magnetic moment at 7 T applied field is approximately 0.48 μ_B per magnetic ion in the LiOH layer which is 20% smaller than the similar Mn-doped compound; this is likely why long range magnetic order was not observed in neutron powder diffraction measurements on this system. The effect of dopant in the FeSe layer

$(Li_{0.857(1)}Fe_{0.14(4)}OD)Fe_{0.992(3)}Se$ (298 K, PXRD), *P4/nmm*, R_{wp} = 12.330%						
a = 3.8056(3) Å,c = 9.2424(1) Å						
atom	Site	x	y	z	Occ.	U_{iso} (Å^2)
Li/Fe1	2b	0	0.5	0	0.822(1)/0.14(4)	0.0247(3)
Fe2	2a	0.5	0.5	0	0.992(3)	0.0183(5)
Se1	2c	0	0.5	0.1604(1)	1	0.0169(1)
O1	2c	0.5	0	0.4293(3)	1	0.0083(3)
Fe-Se (Å)	Se-Fe-Se (°)	Se-Fe-Se (°)	Fe-Fe (Å)			
2.412(1)	112.20(1)	104.12(2)	2.690(9)			
$(Li_{0.857(1)}Fe_{0.14(4)}OD)Fe_{0.992(3)}Se$ (2 K, NPD, *P4/nmm*, R_{wp} = 6.222%						
a = 3.8375(4) Å,c = 9.040(1) Å						
atom	Site	x	y	z	Occ.	U_{iso} (Å^2)
Li/Fe1	2b	0	0.5	0	0.822(1)/0.14(4)	0.0118(2)
Fe2	2a	0.5	0.5	0	0.992(3)	0.0595(6)
Se1	2c	0	0.5	0.1651(5)	1	0.0024(7)
O1	2c	0.5	0	0.4313(8)	1	0.019(1)
D1	2c	0.5	0	0.327(1)	1	0.046(2)
Fe-Se (Å)	Se-Fe-Se (°)	Se-Fe-Se (°)	Fe-Fe (Å)			
2.431(4)	112.16(1)	104.21(6)	2.713(5)			

Tab. 4.5: Structural parameters for ground single crystals of $(Li_{0.857(1)}Fe_{0.14(4)}OD)Fe_{0.992(3)}Se$. Structures are for room temperature PXRD data and 3 K NPD data. All relevant bond angles and distances from the refinements are given. Standard uncertainties given in parantheses indicate one standard deviation.

and superconductivity is clearly observed in the nominally 20% Ni doped sample. For Ni doping, Ni does not replace Li in the LiOH layer and instead we observe 2% Ni substitution of Fe in the FeSe layer. In previous work, superconductivity in the Ni-doped FeSe system was suppressed by >5% Ni doping,[158] and we observe similar results in magnetic susceptibility of the $(Li_{0.8229(1)}Fe_{0.176(3)}OD)Fe_{0.964(3)}Ni_{0.020(1)}Se$ powder sample. Magnetic susceptibility and isothermal magnetization of the sample shows paramagnetic behavior with slight bifurication of ZFC-FC curves around 130 K which is likely due to slight amount of iron oxide impurity; superconductivity is completely suppressed. This result is somewhat expected since the FeSe layers are no longer pristine with 2% Ni substitution and 1.5% vacancies on the Fe site in the FeSe layers.

$(Li_{0.847(2)}Fe_{0.15(1)}OD)Fe_{0.995(2)}Se$ (298 K, PXRD), *P4/nmm*, R_{wp} = 12.330%						
a = 3.7837(3) Å,c = 9.281(1) Å						
atom	Site	x	y	z	Occ.	U_{iso} (Å^2)
Li/Fe1	2b	0	0.5	0	0.847(2)/0.15(1)	0.0155(6)
Fe2	2a	0.5	0.5	0	0.995(2)	0.0266(1)
Se1	2c	0	0.5	0.1591(1)	1	0.0153(2)
O1	2c	0.5	0	0.4293(5)	1	0.0015(8)
Fe-Se (Å)	Se-Fe-Se (°)	Se-Fe-Se (°)	Fe-Fe (Å)			
2.400(1)	112.25(2)	104.03(5)	2.675(5)			
$(Li_{0.847(2)}Fe_{0.15(1)}OD)Fe_{0.995(2)}Se$ (2 K, NPD, *P4/nmm*, R_{wp} = 7.750%						
a = 3.8375(4) Å,c = 9.040(1) Å						
atom	Site	x	y	z	Occ.	U_{iso} (Å^2)
Li/Fe1	2b	0	0.5	0	0.847(2)/0.15(1)	0.024(8)
Fe2	2a	0.5	0.5	0	0.995(2)	0.0032(5)
Se1	2c	0	0.5	0.1608(4)	1	0.0041(3)
O1	2c	0.5	0	0.4234(7)	1	0.0131(6)
D1	2c	0.5	0	0.322(1)	1	0.051(1)
Fe-Se (Å)	Se-Fe-Se (°)	Se-Fe-Se (°)	Fe-Fe (Å)			
2.399(1)	112.21(1)	104.12(2)	2.675(8)			

Tab. 4.6: Structural parameters for ground single crystals of $(Li_{0.847(2)}Fe_{0.15(1)}OD)Fe_{0.995(2)}Se$. Structures are for room temperature PXRD data and 3 K NPD data. All relevant bond angles and distances from the refinements are given. Standard uncertainties given in parantheses indicate one standard deviation.

The Cu and Zn-dopes samples behave very similarly. In both cases, we have observed from high resolution x-ray powder diffraction and neutron powder diffraction that Cu and Zn ions do not replace Li ions in the LiOH or Fe ions in the FeSe layers. Thus, the resulting product shows very similar behavior to previous work on the un-doped (LiOD)FeSe system where the superconducting criticial temperature is dependent on the tetragonality of the system.[82] As with other un-doped (LiOD)FeSe works, no long range magnetic order was observed in the neutron powder diffraction measurements on the Cu and Zn-doped samples. The vacancies caused by the removal of Cu and Zn ions from the starting material were filled by the additional Fe powders/granules added in the reaction scheme which cause the FeSe layers of the products in both cases to remain close to

pristine.

These results show that transition metal doping of the (LiOD)FeSe system is limited to the harder low valence transition metals (Mn, Co, and Ni). We have shown that Mn-doping can lead to the observation of long range magnetic order in the system by increasing the effective moment of the transition metal in the LiOH layers without largely effecting the superconductivity as the FeSe layers remain pristine. Co doping behaves similarly, whereby Co ions only go to the LiOH layer, but the level of Co substitution was lower than in the Mn case leading to no observable long range magnetic order. Ni doping was observed to be detrimental to superconductivity in the system as Ni replaces Fe in the FeSe layer destroying superconductivity. Thus, increased Mn and Co doping, beyond 20% as long as the starting material can be synthesized, is a viable method to stabilize single crystals of magnetic heterolayer superconductors.

4.7 Conclusions

The coexistence of superconductivity and magnetism may be the key to realize the next generation of multi-functional materials. To that end, we have successfully synthesized a series of late transition metal doped (LiOH)FeSe single crystals through a hydrothermal ion-exchange reaction has been shown to house the co-existence of superconductivity and long-range magnetic order in the case of the nominally 20% Mn-doped sample. We have fully characterized the 20% Mn-doped sample through powder x-ray and neutron diffraction yielding a stoichiometry of $(Li_{0.875(2)}Fe_{0.062(3)}Mn_{0.062(3)}OD)FeSe$ showing that the doped Mn migrates fully to the hydroxide layer. Magnetic measurements

show a superconducting transition at 25 K with shielding fraction $\sim$ 25% indicating the superconductivity in single crystal samples may be filamentary in nature with magnetization showing clear Meissner shielding and magnetic signal co-existing at low temperatures exclusively. Transport measurements show a sharp 41 K transition in resistivity with a distinct non-linear normal state with no clear anomaly detected around the superconducting transition in heat capacity. However, a clear magnetic peak was observed at $\sim$ 9K in heat capacity measurement which remains robust up to 14 T applied field parallel to the crystallographic *c*-axis. Powder neutron diffraction data reveals a satellite magnetic reflection at $Q = 1.41 - 1.44$ Å^{-1} indicating the long-range character of the magnetic order in this system observed for the first time. Additional neutron experiments would be required to elucidate the nature of the magnetic ordering in this system. This work shows that the (LiOH)FeSe system offers a platform for chemical manipulation to induce the coexistence of long range magnetic order and superconductivity for possible exploitation as multi-functional materials and for use in quantum computing.

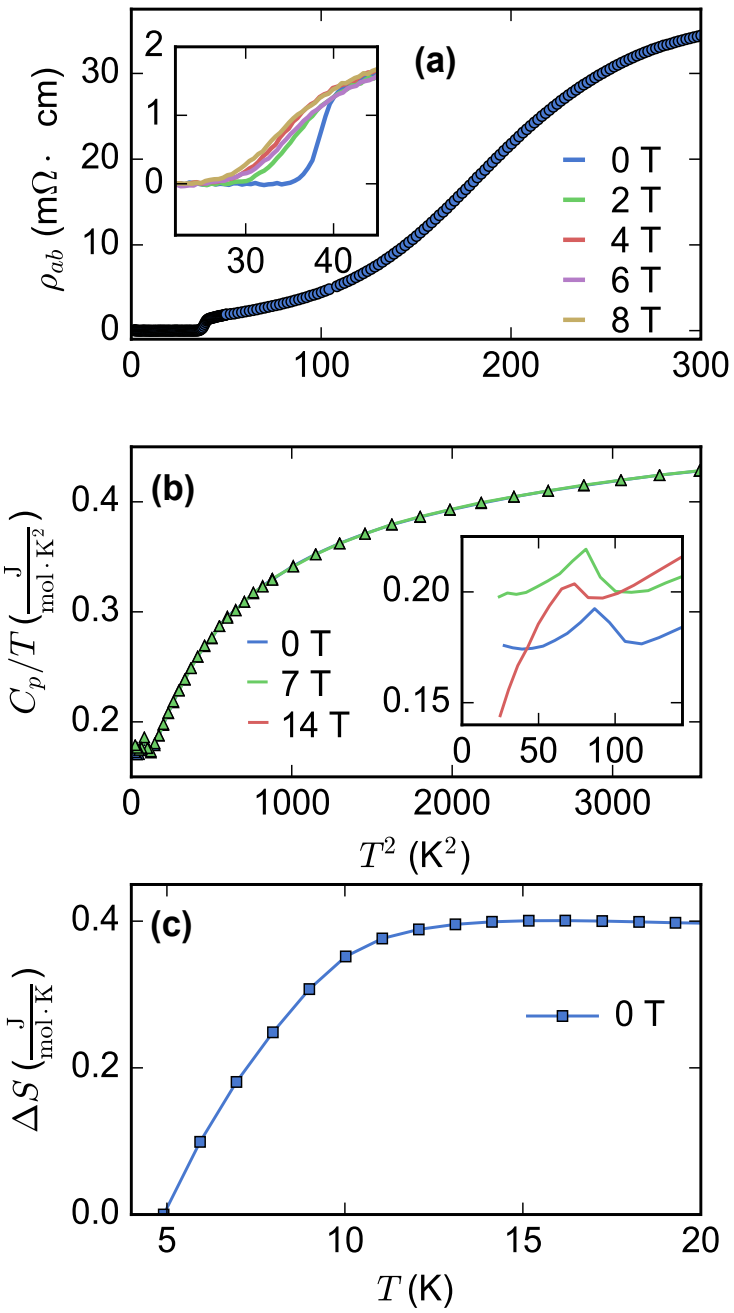

Fig. 4.5: Electronic and thermal transport measurements on a single crystal of $(Li_{0.875(2)}Fe_{0.062(3)}Mn_{0.062(3)}OD)FeSe$. a) Temperature dependence of electrical resistivity with mutiple applied fields, with the applied field parallel to the crystallographic *c*-axis, showing a sharp superconducting transition at 41 K. At higher applied fields, the transition onset does not change, but the transition width is increased drastically. b) Temperature dependence of heat capacity at various applied fields showing no observable anomaly at the superconducting transition temperature, however; a magnetic transition is observed at ~ 9 K that is weakly suppressed with high field (inset). c) The change in entropy calculated as described in main text.

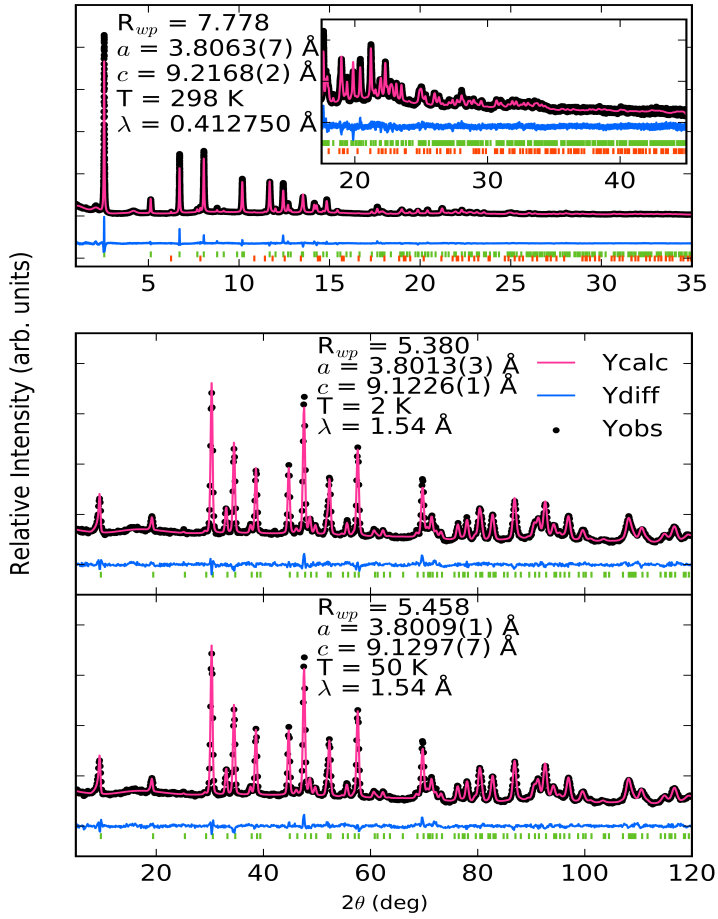

Fig. 4.6: top) High resolution synchrotron powder X-ray diffraction patterns for $(Li_{1-x-y}Fe_xNi_yOD)Fe_{1-z}Mn_zSe$ collected at room temperature, (middle and bottom) show powder neutron diffraction data for $(Li_{1-x-y}Fe_xNi_yOD)Fe_{1-z}Mn_zSe$ at 2 K and 50 K respectively. Green tick marks represent the targeted tetragonal layered phase and orange tick marks represent impurity selenium. These are shown below the calculated, observed, and differences curves from Rietveld analysis. Analysis yielded a composition of $(Li_{0.8229(1)}Fe_{0.176(3)}OD)Fe_{0.964(3)}Ni_{0.020(1)}Se$.

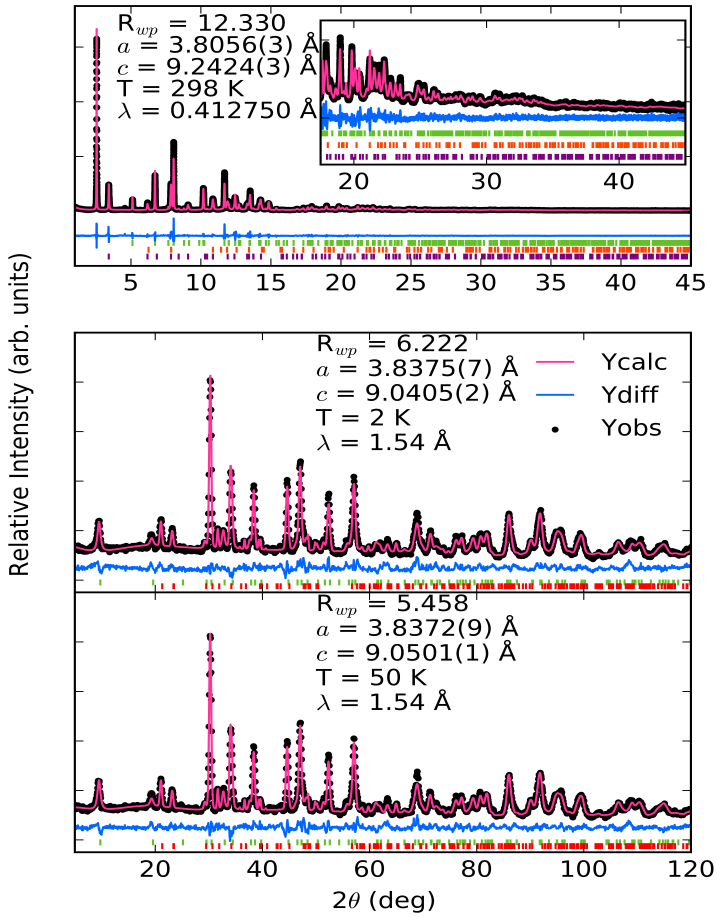

Fig. 4.7: a) High resolution synchrotron powder X-ray diffraction patterns for $(Li_{1-x-y}Fe_xCu_yOD)Fe_{1-z}Cu_zSe$ collected at room temperature, b) and c) show powder neutron diffraction data for $(Li_{1-x-y}Fe_xCu_yOD)Fe_{1-z}Cu_zSe$ at 2 K and 50 K respectively. Green tick marks represent the targeted tetragonal layered phase, orange tick marks represent impurity selenium, and purple tick marks represent impurity starting material in the x-ray data. These are shown below the calculated, observed, and differences curves from Rietveld analysis. Due to remaining starting material, the sample was reacted for 3 additional days before neutron analysis, where green tick marks represented the targeted phase and orange tick marks show impurity lithium carbonate. Analysis yielded a composition of $(Li_{0.857(1)}Fe_{0.14(4)}OD)Fe_{0.992(3)}Se$.

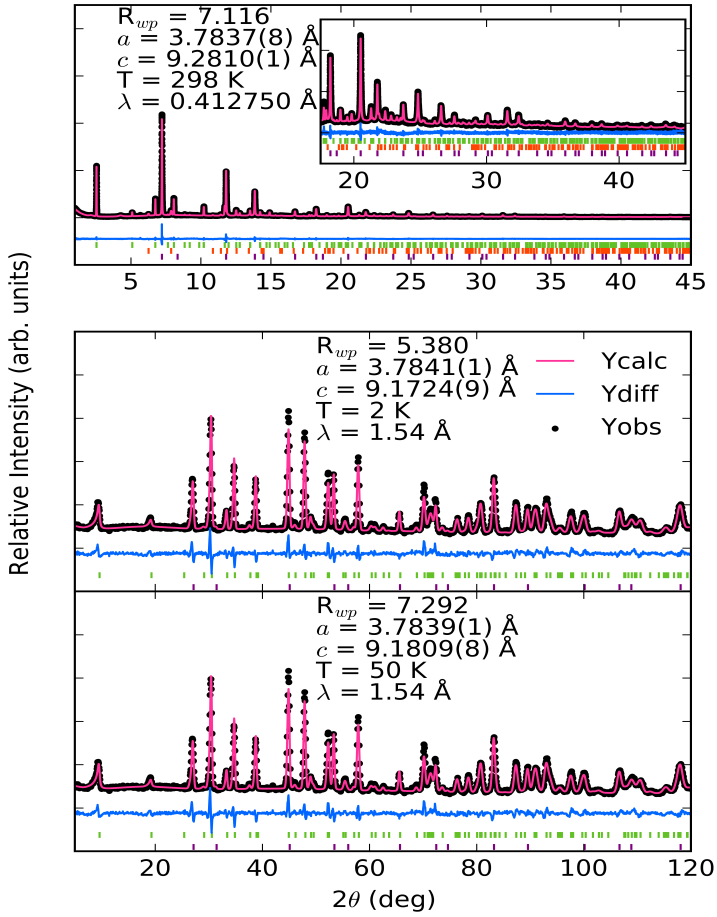

Fig. 4.8: a) High resolution synchrotron powder X-ray diffraction patterns for $(Li_{1-x-y}Fe_xZn_yOD)Fe_{1-z}Zn_zSe$ collected at room temperature, b) and c) show powder neutron diffraction data for $(Li_{1-x-y}Fe_xZn_yOD)Fe_{1-z}Zn_zSe$ at 2 K and 50 K respectively. Green tick marks represent the targeted tetragonal layered phase, orange tick marks represent impurity selenium, and purple tick marks represent impurity zinc selenide. These are shown below the calculated, observed, and differences curves from Rietveld analysis. Analysis yielded a composition of $(Li_{0.847(2)}Fe_{0.15(1)}OD)Fe_{0.995(2)}Se$.

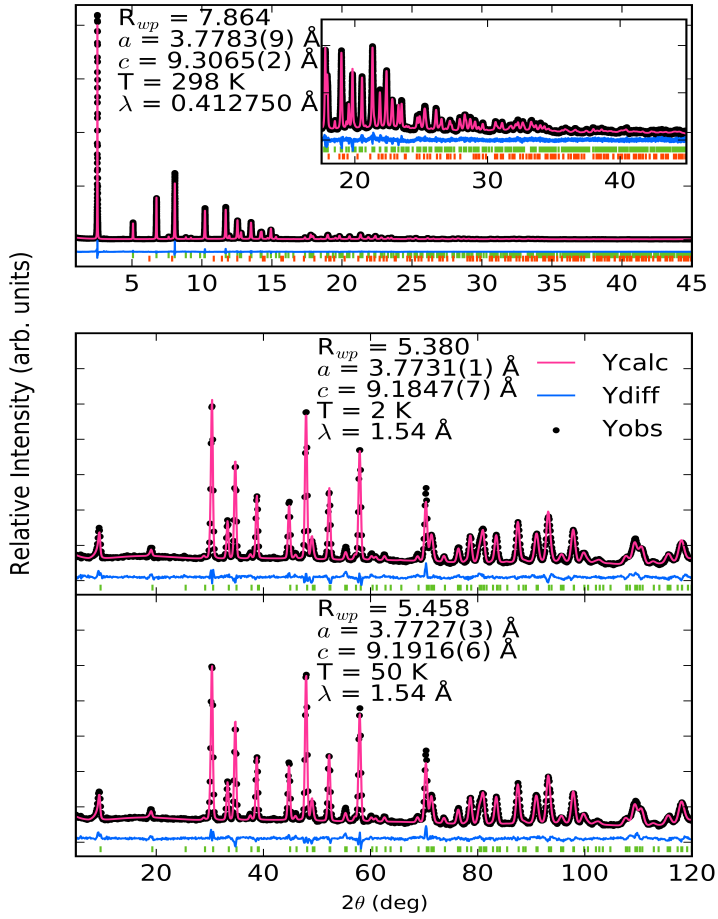

Fig. 4.9: a) High resolution synchrotron powder X-ray diffraction patterns for $(Li_{1-x-y}Fe_xCo_yOD)Fe_{1-z}Co_zSe$ collected at room temperature, b) and c) show powder neutron diffraction data for $(Li_{1-x-y}Fe_xCo_yOD)Fe_{1-z}Co_zSe$ at 2 K and 50 K respectively. Green tick marks represent the targeted tetragonal layered phase and orange tick marks represent impurity selenium. These are shown below the calculated, observed, and differences curves from Rietveld analysis. Analysis yielded a composition of $(Li_{0.842(1)}Fe_{0.135(4)}Co_{0.02(3)}OD)Fe_{0.950(2)}Se$.

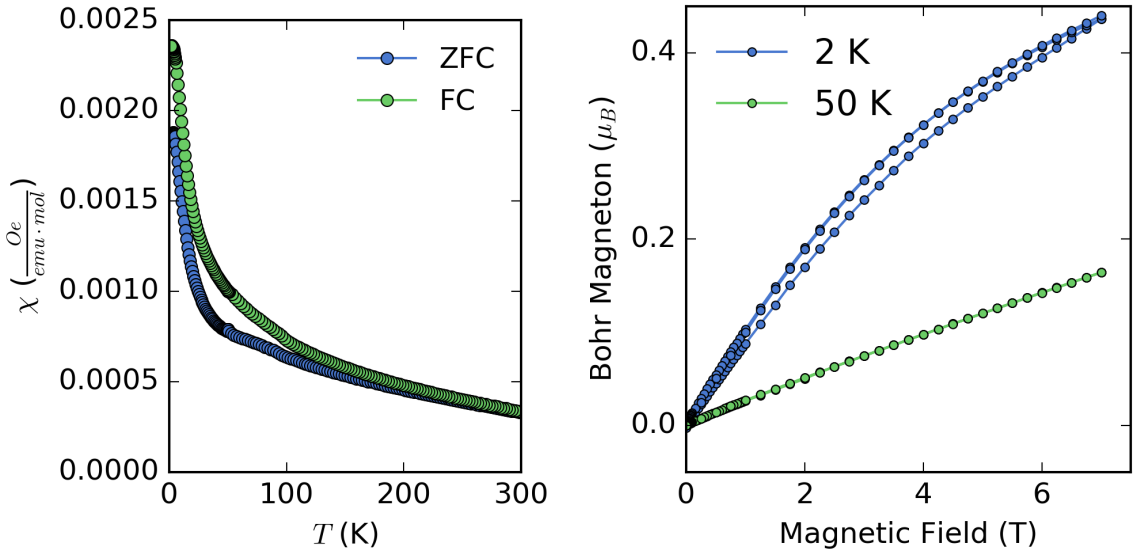

Fig. 4.10: (left) Temperature dependent magnetic susceptibility at 30 Oe and (right) Isothermal magnetization at 2 K and 50 K measured on ground single crystals of $(Li_{0.8229(1)}Fe_{0.176(3)}OD)Fe_{0.964(3)}Ni_{0.020(1)}Se$ displaying non-superconducting behavior, most likely due to Ni substitution on the Fe-site in the FeSe layers.

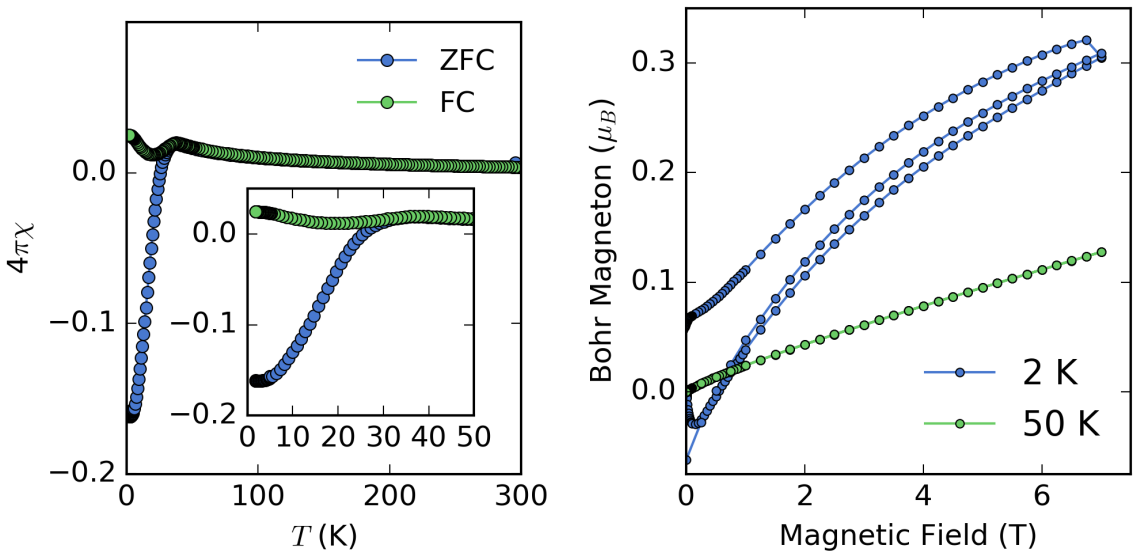

Fig. 4.11: (left) Temperature dependent magnetic susceptibility at 30 Oe and (right) Isothermal magnetization at 2 K and 50 K measured on ground single crystals of $(Li_{0.857(1)}Fe_{0.14(4)}OD)Fe_{0.992(3)}Se$ displaying superconducting behavior with a superconducting transition at 32 K.

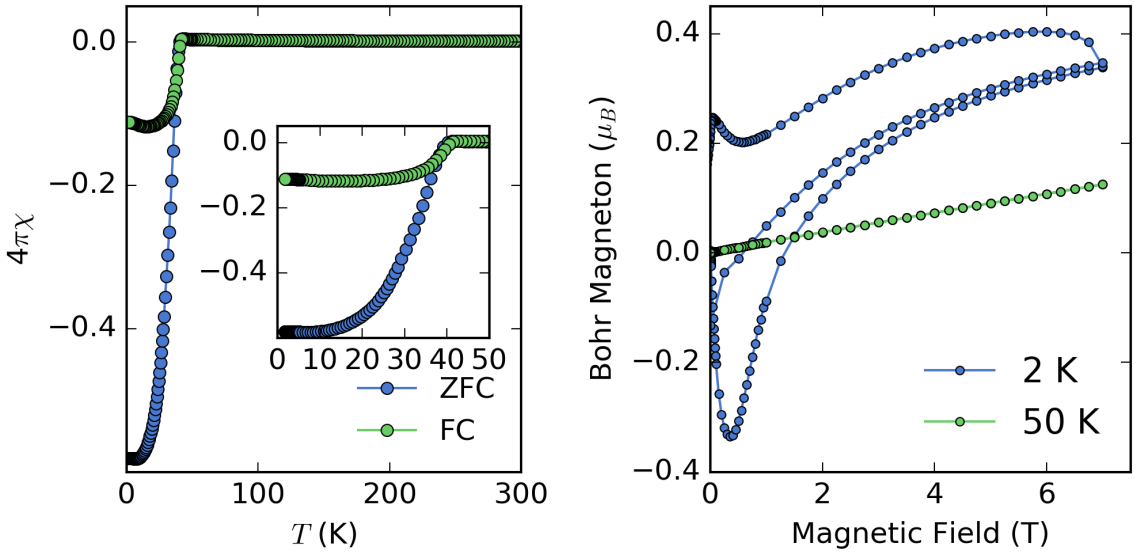

Fig. 4.12: (left) Temperature dependent magnetic susceptibility at 30 Oe and (right) Isothermal magnetization at 2 K and 50 K measured on ground single crystals of $(Li_{0.847(2)}Fe_{0.15(1)}OD)Fe_{0.995(2)}Se$ displaying superconducting behavior with a superconducting transition at 42 K.

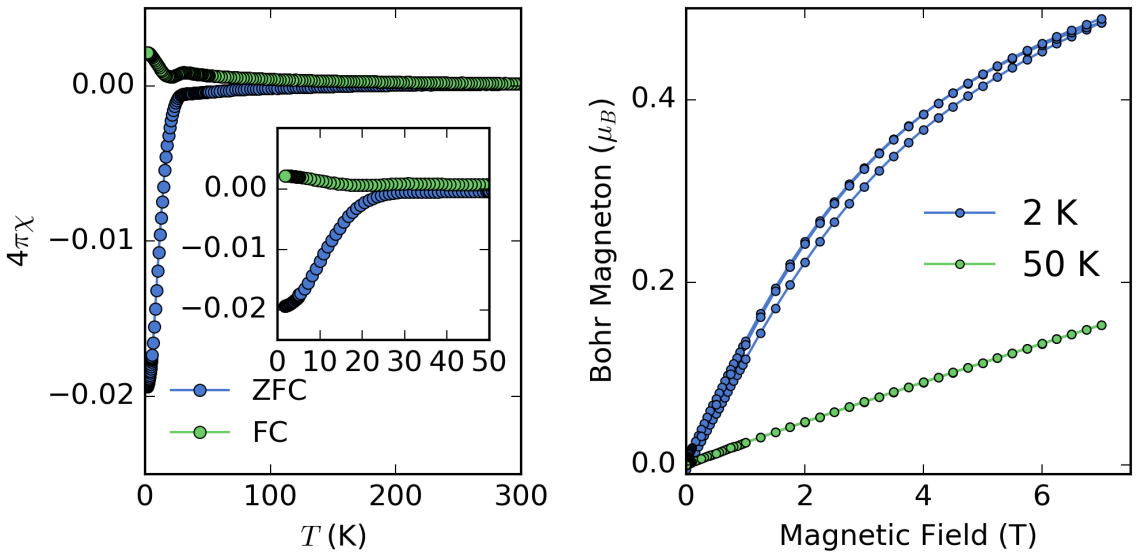

Fig. 4.13: (left) Temperature dependent magnetic susceptibility at 30 Oe and (right) Isothermal magnetization at 2 K and 50 K measured on ground single crystals of $(Li_{0.842(1)}Fe_{0.135(4)}Co_{0.02(3)}OD)Fe_{0.950(2)}Se$ displaying superconducting behavior with a superconducting transition at 30 K.

Chapter 5: Alkali metal-free hydrothermal synthesis of ethylenediamine intercalated iron chalcogenides

The work described within this chapter was submitted to *Inorganic Chemistry*. Brandon Wilfong, Xiuquan Zhou, Huafei Zheng, Johnpierre Paglione, Rishvi Jayathialake, Daniel J. Campbell, Sz-Chian Liou, and Efrain Rodriguez were contributing authors of the manuscript. B.W., X.Z., and H.Z. prepared the samples, B.W. collected X-ray diffraction data, performed MPMS measurements and collected resistivity data, B.W. and S.C.L performed TEM and ED experiments, D.J.C. collected SEM and EDS data and R.J. performed TGA analysis.

5.1 Introduction

The discovery of superconductivity in the iron-based superconductors $La(O_{1-x}F_x)FeAs$[22] and FeSe[42] spurred a surge of research activity. Much like the copper-oxygen layers which are key for superconductivity in the copper-based superconductors[245], all iron-based superconductors contain stacked layers of iron pnictides or chalcogenides.[27] In the simplest case, FeSe contains stacked tetrahedral layers of an square iron sublattice with each iron tetrahedrally coordinated to either pnictide or chalcogenide atoms.[42,45]

With FeSe and FeS displaying superconductivity at 8 K[42] and 4 K[58], respectively,

there has been substantial research on intercalation chemistry within the system to probe how intercalated species will affect the properties. Much of the work has focused on FeSe as opposed to FeS due to the metastability of FeS.[59] To date the successful intercalates of the iron chalcogenide system consists of simple cations[76–78] and/or partially charged hydroxide or amine layers.[46,79–81,83–87] After intercalation the T_c of FeSe can be raised significantly to 43-46 K from 8 K. Although both hydroxide or amine intercalation can increase the T_c of FeSe, only LiOH intercalation is known to increase the T_c of FeS.[87]

In the case of simple cations, ionic interactions between the cationic layer and the iron chalcogenide layers help stabilize the structure. However, in the partially charged amine or hydroxide case non-ionic guest-host interactions such as hydrogen bonding would also help stabilize the layered structures. In most works regarding intercalation of amines, the co-intercalation of alkali metal atoms has been required since they to coordinate with the amine molecules.[46,83–86] We demonstrate here that alkali metal cations are not required and intercalated strucutures may be stabilized by hydrogen bonding alone.

Amine intercalations are usually achieved by forming solvated electrons using alkali metal and liquid amines, which inevitably leads to co-intercalation of alkali metal ions. This makes determining the electron doping effect on the T_c of FeCh (Ch = S and Se) quite difficult due to the formation of multiple intercalated species. Two different approaches in synthesis have been pursued to understand the doping effect of these intercalated species and samples. One approach is to directly react FeCh with amines solvothermally, to form ethylenediamine(EDA)-intercalated FeSe and FeS.[246–248] However, the type of potential intercalates are limited using this method as the intercalates have to be in the form of liquid or exhibit low melting points. The other approach is to

hydro/solvothermally prepare intercalated Fe*Ch* phases through bottom-up synthesis. We pursue this approach here in order to find synthetic routes that maximize the number of different intercalates that can be inserted into Fe*Ch* superconductors without the requirement of alkali metals. In the previously mentioned synthetic approaches, alkali metals are directly reacted with amines before adding the iron chalcogenides species which results in a differently chemically active solvated alkali metal ions[249–251] as opposed to aqueous alkali metal hydroxide ions used in our synthetic route. Thus, alkali metal - amine reaction scheme, solvated alkali metals co-intercalate with amines whereas in our reaction scheme, the aqueous alkali metal does not coordinate to the amine and co-intercalate between the iron chalcogenide layers.

5.2 Experimental Methods

For a typical preparation of EDA-intercalated Fe*Ch* (*Ch* = S, Se), 4 mmol of Fe powder (Alfa Aesar, 99.5%), 10 mmol of thiourea (Sigma-Aldrich, 99%) or 5 mmol selenourea (Sigma-Aldrich, 98%), 7 mmol of KOH (Fisher, 85%) which equates to $\sim$ 0.5 M solution, 10 mL H_2O, and 3 mL ethylenediamine (Sigma-Aldrich, 99%) sealed within a Teflon cup within a stainless steel autoclave at 120 - 160 °C for 2 - 6 days. After the hydrothermal process, the contents were washed and centrifuged with de-ionized water several times until the supernatant was clear. The recovered black powders were collected, vacuum dried and stored in an Argon glovebox.

Powder X-ray diffraction (XRD) data was collected usining a Bruker D8 X-ray diffractometer utilizing Cu Kα radiation (λ = 1.5418 Å, 2θ = 5 - 70°, step size = 0.020°).

Pawley refinements were performed using the TOPAS software.[126] Microscopic images were examined on a Hitachi SU-70 SEM field emission scanning electron microscope (SEM), and their elemental compositions were determined by energy dispersive X-ray spectroscopy (EDS) using a Bruker EDS detector. Electron diffraction patterns were obtained using a JEM 2100 LaB_6 transmission electron microscope (TEM) at an acceleration voltage of 200 KeV. Thermogravimetric analysis (TGA) and differential scanning calorimetry (DSC) were performed using Mettler Toledo TGA/DSC 2 under high-purity Ar. TGA/DSC samples were placed in alumina crucibles covered with alumina lids and heated from room temperature to 600 °C at the rate of 10 °C/min.

Magnetic susceptibility and magnetization measurements were performed using a Quantum Design Magnetic Property Measurement System (MPMS3). Temperature dependence of magnetic susceptibility was performed at various applied fields and magnetization isotherms were measured up to fields of ± 7 T. Electrical resistivity measurements were performed on as-recovered and annealed samples of pressed pellets of ground powders cold-pressed into a pellet with 2000 psi of uniaxial stress. Temperature dependence of electrical resistivity was performed using the four-probe method from 2 K - 300 K with applied currents of 0.1 mA and frequencies around 17 Hz.

5.3 Results and Discussion

5.3.1 Alkali metal free hydrothermal ethylenediamine intercalation

All successful hydrothermal intercalations of EDA occurred at 120 °C; higher temperatures led to increased FeSe/FeS and Fe_3O_4 formation with no intercalation. The re-

sults of varying the reaction time are presented in Figure 5.1 and 5.2. For the sulfide analogue, we find successful intercalation after two day reaction time; however,some tetragonal FeS remained. At four days, the remaining FeS is fully intercalated by EDA. After six days, no intercalation is observed and only poorly crystalline FeS and iron powder remain. For the selenide analogue, two day reactions reveal a possible intermediate intercalated phase. This new layered phase could be indexed with the structurally related $K_xFe_ySe_2$ (122-type), although its stoichiometry could not be determined. In previous works, this phase was shown to form in the sulfide case when using KOH as the base in the reaction.[87] After a four day reaction, the 122-type structure had converted to EDA-intercalated phase and the formation of Fe_3O_4 is observed. After six days, there is no intercalated phase, all that remains is poorly crystalline FeSe, additional Fe_3O_4, and Fe powder.

Previous work on amine intercalation in Fe*Ch* species focused on the co-intercalation of alkali metal ions which would stabilize the amine intercalate through alkali metal coordination to the amide groups.[46] This method has been successful for a number of different amines and alkali metals,[77,83,85,86,252,253] but the amount of electron doping level in these systems is difficult to solve. Amines can intercalate as both neutral molecules and negatively charged amides or imides.[46] Therefore, simply determining the alkali metal content does not gave the electron doping level. However, using our hydrothermal method the formation of metal amides are prevented. Also, due to the co-intercalated alkali metal, all compounds made via the previous method are extremely air sensitive making extended characterization increasingly difficult. Thus, this work aims to use our hydrothermal method in order to remove the necessity for alkali metal coordination as the stabilizing

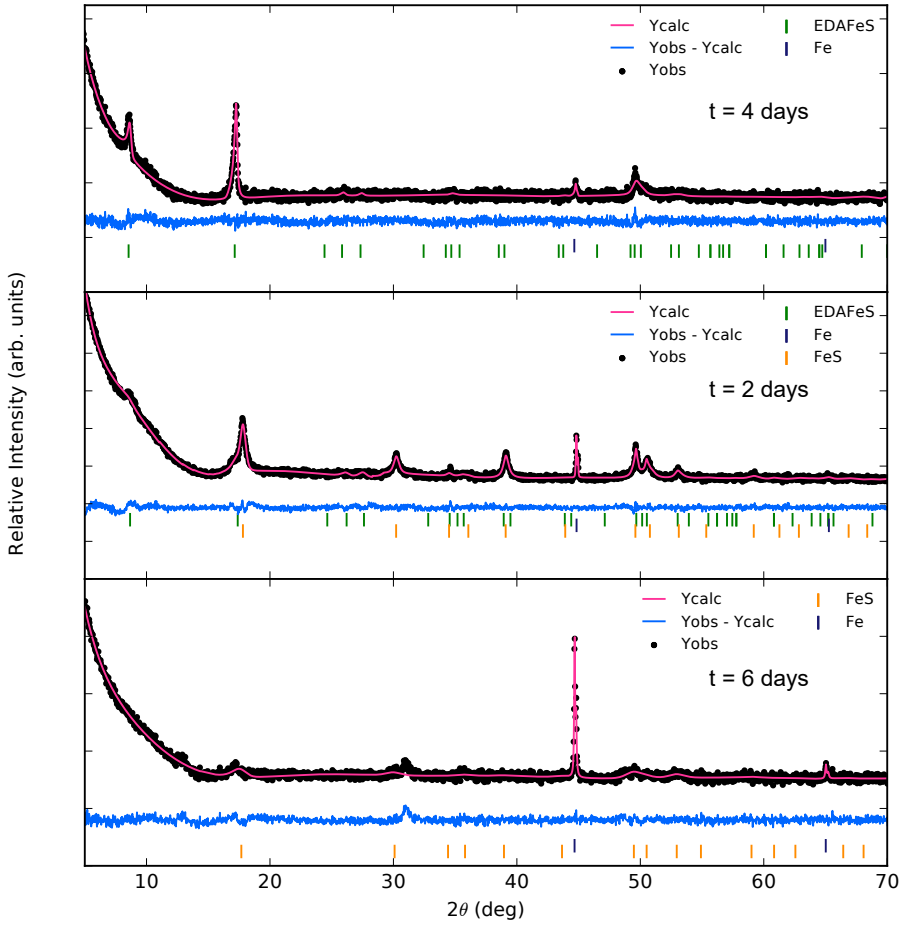

Fig. 5.1: Pawley refinements on ground powders of $(C_2H_8N_2)_xFeS$ after varying hydrothermal reaction times.

factor.

Previously, we intercalated ammonia molecules along with protons hydrothermally into Fe*Ch* layers. We resolved the structure of intercalated species through the use of neutron powder diffraction. In this analysis, the location of the hydrogen atoms and ammonia molecules were determined and the N-H$\cdots$*Ch* had clear implications for hydrogen bonding. However, this type of structural analysis is nearly impossible for ethylenediamine molecule NH_2-C_2H_4-NH_2 where all 12 atoms are in the highly disordered 16*i* site, for the *I4/m* space group.[86] Secondly, previous work showed that the proton position is at the 2b

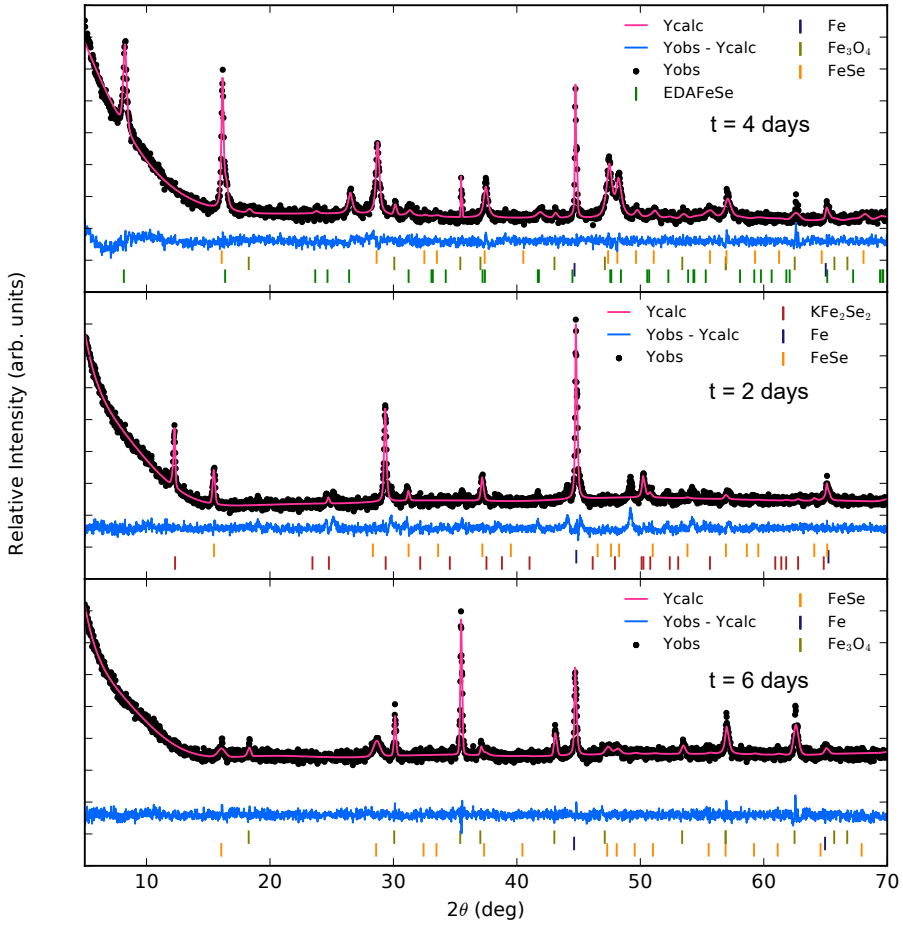

Fig. 5.2: Pawley refinements on ground powders of $(C_2H_8N_2)_yFeSe$ after varying hydrothermal reaction times.

site with about 50% of the occupancy, which allows for precise refinement from neutron diffraction and direct understanding of the doping effects within the system. Previous work[246–248] has shown this synthesis can be done solvothermally, however; this severely limits the types of intercalate adducts that can be used as they must be liquid at or below 120 °C, especially in the case of FeS due to its limited thermal stability.

The results of the SEM, EDS and TGA measurements are presented in Figure 5.3 and 5.4, which help us understand the morphology, composition, and stability. Elemental analysis from EDS is in general agreement with previous reports,[246,248] although direct

stoichiometry cannot be matched due to remaining iron and iron-containing impurities, especially showing that our samples do not show alkali metals which are present in samples grown by the alkali metal - amine method.[254,255]This confirms that our samples are alkali metal free as the aqueous alkali metals from the alkali metal hydroxides do not co-intercalate with the ethylenedimaine as solvated alkali metal ions do in the previously discussed synthetic method. This is likely due to the difference in chemical activity of solvated alkali metal ions as opposed to aqueous alkali metal ions. Elemental analysis for C/H/N cannot be performed with EDS due to their low effective charge and highly overlapping spectra. TGA analysis was performed under argon atmosphere to show that the hydrothermal intercalated phases are stable up to temperatures higher than previously reported for intercalated Fe*Ch* phases.[246,248] $(C_2H_8N_2)_x$FeS showed weight loss, owning to ethylenediamine de-intercalation, at 225 °C, while $(C_2H_8N_2)_y$FeSe did not show de-intercalation until 350 °C. Although these de-intercalation temperatures are different than the reported weight loss temperatures for the ammonia intercalated phases[256], we cannot definitely rule out that ammonia intercalated species do not exist in this compound due to the use of thiourea and selenourea as the chalcogenide sources. Weight loss before and after the de-intercalation give rough estimates of x = 0.19 and y= 0.16 ethylenediamine occupancy per unit cell for $(C_2H_8N_2)_x$FeS and $(C_2H_8N_2)_y$FeSe respectively; these values are both less than their solvothermal analogues which may mean the ethylenediamine coordination or intercalated structure may differ due to the different synthetic method.[246,248] Surprisingly, this means the ethylenediamine intercalated FeS phase is stable up to temperature comparable to the metastable FeS binary.[59]. The selenide analogue is much more stable than the solvothermal synthesized version[246] and matches the highest tem-

peratures at which alkali metal co-intercalated ethylenediamine samples were annealed.[84] Both samples do not appear to be air sensitive after exposure for a week. The large thermal range of stability for these hydrothermally prepared iron chalcogenides gives a good basis for post-modifications to alter the physical properties.

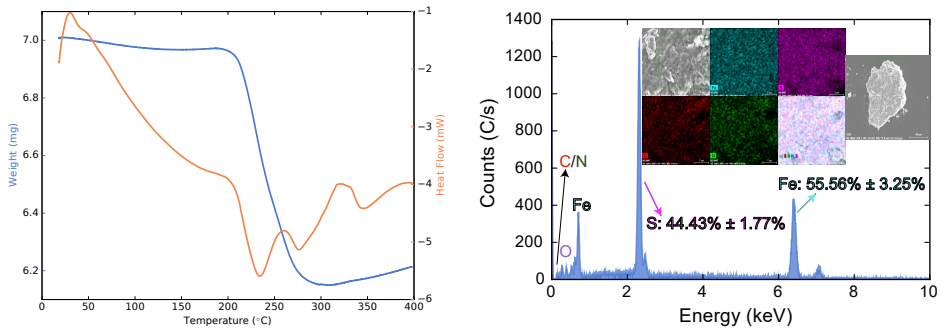

Fig. 5.3: TGA and SEM/EDS analysis of $(C_2H_8N_2)_xFeS$ ground powders.

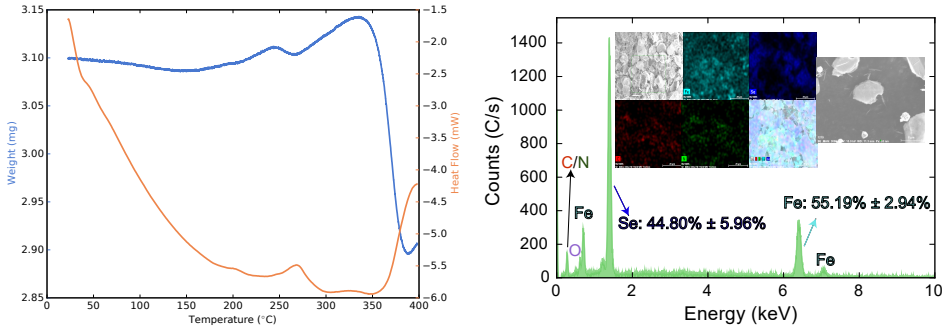

Fig. 5.4: TGA and SEM/EDS analysis of $(C_2H_8N_2)_yFeSe$ ground powders.

5.3.2 Intercalated ethylenediamine crystallography and symmetry

Figure 5.5 shows XRD patterns for $(C_2H_8N_2)_xFeS$ and $(C_2H_8N_2)_yFeSe$ as recovered from the hydrothermal autoclave. Pawley fits were used to model the diffraction data since the intercalated structure is too complex to solve by Rietveld analysis with the laboratory XRD sources. However, neutron powder diffraction (NPD) could help solve the position

of the light elements of the organic clusters. Previously Jin et al. had utilized NPD to solve the structure of a related intercalated phase $Na_{0.39(1)}(C_2N_2H_8)_{0.77(1)}Fe_{2.02(1)}Se_2$.[86]. Therefore, we used a similar model with space group $I4/m$ for our Pawley fits of the intercalated structure. Both patterns can be indexed well using this space group yielding lattice parameters close to previous reports.[248] It should be noted that in both powder patterns only the (00l) reflections are resolved due to strong preferred orientation as well as possible stacking faults along the c-axis.

For $(C_2H_8N_2)_x$FeS, Pawley fits gave lattice parameters of a = 3.700(5) Å, c = 20.67(1) Å which are in close agreement to alkali metal and alkali metal-free ethyelendiamine intercalated FeS.[77,248] In this case, the a-axis lattice parameter is slightly larger due to the $in-situ$ formation of the FeS layers as opposed to intercalating pre-formed tetragonal FeS powders. In *in-situ* formation of FeS layers may be influenced by the intercalated species through hydrogen bonding directionality and stability. Interestingly, the c-axis lattice parameter is in much closer agreement to the potassium co-intercalated ethylenediamine FeS rather than the solvothermal EDA treatment possibly due to the role of proton intercalation via the hydrothermal process. The only remaining impurity comes from excess Fe powder remaining from the $in-situ$ growth of FeS layers. To avoid excess Fe, we attempted syntheses using pre-reacted tetragonal FeS at 120 °C over 2 - 6 days, but were unsuccessful. Remaining Fe powder could be mostly removed from the recovered product by using a weak magnet. However, this recovery method significantly reduced product yield since the desired product was intergrown with unreacted Fe powders.

Pawley fits for selenide analogue yielded lattice parameters of a = 3.813(2) Å, c = 21.64(3) Å. The previous solvothermal work indexed the EDA-intercalated FeSe with

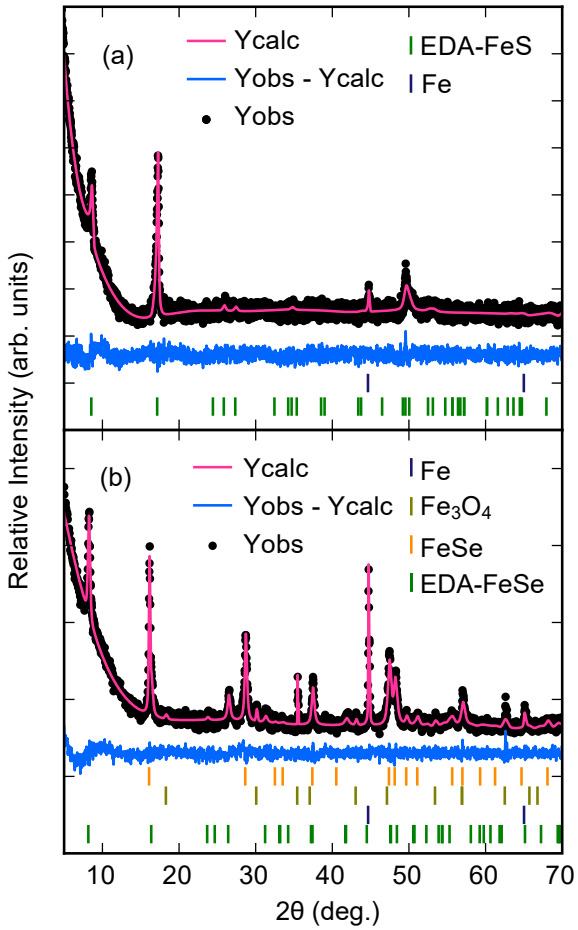

Fig. 5.5: Pawley refinements with powder XRD for the structures of $(C_2H_8N_2)_xFeS$ and $(C_2H_8N_2)_yFeSe$ as recovered from hydrothermal synthesis. (a) Refinement of $(C_2H_8N_2)_xFeS$ in the body-centered tetragonal structure (*I4/m*) at room temperature; (b) refinement of $(C_2H_8N_2)_yFeSe$ with a body-centered tetragonal structure (*I4/m*) at room temperature. Lower tick marks correspond to the tetragonal phases. Additional tick marks denote impurities present with the sample.

an orthorhombic cell, but we did not find the same result since we did not observe orthorhombic splitting of the (013) or (015) peaks. The *a*-axis and *c*-axis lattice parameters closely agree with previously reported for alkali metal co-intercalated EDA-FeSe and solvothermal EDA-FeSe.[84,86,246,247,255] The powder XRD pattern for $(C_2H_8N_2)_yFeSe$ is more complicated than the sulfide analogues due to the synthetic challenges raised by selenium. To start, additional impurities included tetragonal FeSe and iron oxide Fe_3O_4.

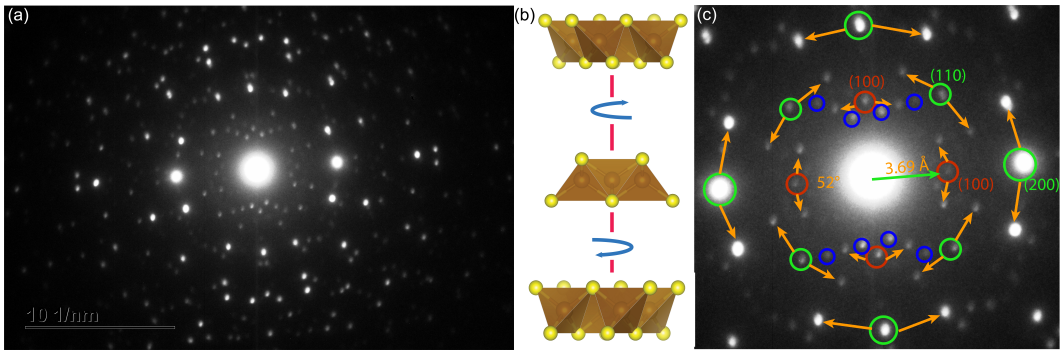

Fig. 5.6: (a) Electron diffraction pattern of ethyelenediamine-intercalated, (b) model FeS layers rotated as observed in electron diffraction images, and (c) FeS, green circles indicating allowed reflections and rotated pairs for the *I4/m* unit cell with red circles indicating forbidden reflections and blue showing possible reflections from intercated EDA molcules.

We easily identify un-intercalated FeSe by its (001) reflection (d = 5.5258 Å), which is proximate to the (004) reflection of the intercalated phase (d = 5.41 Å). We hypothesize that remaining tetragonal FeSe is due to the thermodynamic stability of FeSe compared to that of metastable FeS. The appearance of Fe_3O_4 only in the selenide analogue is due to the electrochemical potential differences of S^{2-} and Se^{2-}. Attempts to remove Fe_3O_4 using reaction times less than 4 days lead to no EDA intercalation while both longer reaction and higher temperatures lead to no intercalation and/or more impurity. Interestingly, the Fe_3O_4 would not form in the product if the reaction was carried out in D_2O instead of H_2O despite reducing the crystallinity. Similar solvent effects were observed for the synthesis of LiOD-intercalated FeSe, where the use of D_2O suppressed the formation of iron oxide impurities.[82]

Since it was not possible to resolve the structure from the powder XRD data, we have investigated their structures via electron diffraction (ED) using transmission electron microscopy (TEM). Despite poor resolution for reflections other than (00l) on their XRD patterns, we observed well-resolved (hk0) reflections by ED. This indicates that the

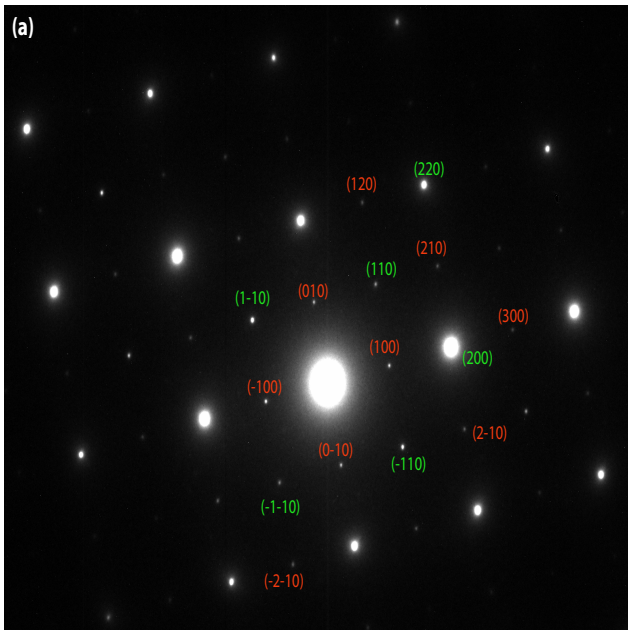

Fig. 5.7: (a) Electron diffraction pattern of ethyelenediamine-intercalated FeSe; green indexing and circles indicate allowed reflections for the *I4/m* unit cell while red indicates forbidden reflections.

seemingly poor crystallinity of the samples is a result of strong anisotropic broadening on the Bragg-Brentano geometry due to extremely short coherence lengths over the *c*-axis of the layers.

The FeS analogue exhibits complicated ED patterns. As shown in Fig. 5.6, the diffraction spots highlighted by green circles could be assigned to three different square lattices with a = 3.69 Å, which is very close to our refined value by PXRD. Interestingly, the two weaker sets of spots are placed at the positions by rotating the stronger set by 26° and -26° respectively. This suggests that the extra two sets of reflections likely do not originate from two other randomly stacked nanocrystals. Indeed, we found another set of weak reflections (highlighted in blue in Fig. 5.6c) that do not show such twin reflections at ±26°. These extra diffraction spots (blue) cannot be indexed with the tetragonal lattice. In addition, considering they are much weaker compared to the square-lattice reflections,

these spots likely originate from the EDA molecules within the sheets. Since they do not rotate with the FeS sheets, it is likely that the EDA molecules do not arrange in a commensurate fashion with the square lattice of FeS and are vertically arranged between the FeS sheets. This configuration of the EDA molecules may be a result of stronger hydrogen bonding in the sulfide over the selenide of the type N-H$\cdots$*Ch*. This hydrogen bonding may lead structure directing of subsequent FeS layers which would result in the observed *c*-axis disorder.

More structural disorder in the intercalated FeS is revealed in Figure 5.8 in Supplemental Information. These images are taken from different crystallites within the same synthetic batch. It is difficult to understand the driving force leading to varying degrees of *c*-axis disorder in this system, but it is likely caused by different degrees of hydrogen bonding or coordination with adjacent FeS sheets. This increased *c*-axis disorder and subsequent ED ''smudging" was observed in ethylenediamine intercalated SnS_2 as well.[257] Figure 5.8 also shows a TEM image of lattice fringes within the sample which display an average length of less than 10 nm indicating short coherence lengths along the c-axis due to stacking faults or possible twisting of the FeS layers due to intercalated EDA.

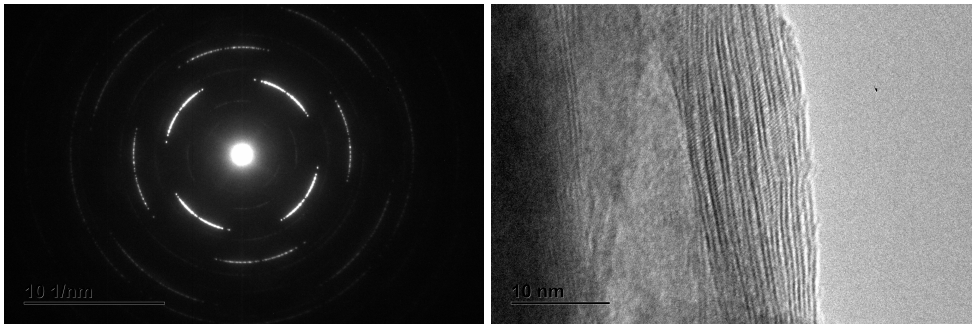

Fig. 5.8: Electron diffraction pattern of ethyelenediamine-intercalated-FeS and TEM image of lattice fringes of EDA-FeS.

For the FeSe sample, its ED pattern agrees with the XRD data as the unit cell can be indexed to a tetragonal one with a = 3.83 Å(Fig. 5.7). However, we were able to observe a set a forbidden reflections at the condition ($h + k = 2n + 1$). This could be caused by disorder or a charge density wave, which is also seen for the ammonia-intercalated FeCh.[256] More interestingly, their ED patterns are almost identical. However, unlike ammonia, whose atoms can be arranged into a nearly perfect tetrahedron, the EDA molecule is much more complex and does not exhibit 4-fold rotational symmetry. The fact that no extra reflection spot breaks the 4-fold symmetry suggests a completely disordered configuration for the EDA molecules. Therefore, all the C, H and N atoms in EDA-intercalated FeSe are likely to occupy the 16i Wyckoff position in a disordered manner. We cannot determine whether protons co-intercalate with EDA to occupy the edge-center (2b site) of the unit cell, but it is a reasonable assumption given the synthetic and structural similarities between both intercalated FeSe phases.

5.3.3 Intercalated ethylenediamine configuration and guest-host interactions

To date, much of the work on the synthesis and characterization of ethylenediamine intercalated iron selenide has focused on the increase in critical temperature observed.[84,86,246,255,258] In these intercalated iron selenide systems, increasing two dimensionality of the FeSe layers as well as charge doping due to intercalated species combine to produce the increase in superconducting critical temperature. Both of these factors are determined by the new structures which form as intercalated species exist between the

FeSe layers. Thus, fully understanding the novel structures which arise from molecular intercalation between these inorganic layers is immensely important for future guided synthesis and to understand how the superconducting properties change in these systems due to the changes in structure.

There exist two main forces which likely help stabilize the intercalation of ethylenediamine in FeSe, electrostatic forces due to charge species formed via ethylenediamine coordination to metal ions and/or hydrogen bonding from the ethleyendiamine molecules to the chalcogenides in the FeSe layers. There has been extensive work on the characterization of ammonia and ethylenediamine intercalation into various layered chalcogenide compounds. For ammonia intercalation of transition metal dichalcogenides, nuclear magnetic resonance and diffraction work has shown that the formation of ammonium ions and/or the arrangement of intercalated ammonia molecules to maximize hydrogen bonding to nearby chalcogenide ions helped stabilize the structure of these compounds.[259–269] Ethylenediamine intercalation is similar although there has been no reports thus far showing a similar homosolvation model to ammonia intercalation. Thus, ethylenediamine exhibits coordination to metal ions in solution to generate interlayer charged species to stabilize the structure, and/or the ethylenediamine molecules arrange to maximize amino-hydrogen bonding toward the chalcogenide layers. In the former case, dissolved metals in solution coordinate with the ethylenediamine molecules to form metal-ethylenediamine coordinated molecules.[270–278] Harder Lewis acid metals preferentially coordinate with the ethylenediamine to form these coordinated species whereas softer cations typically form the chalcogenide layers or chains. When no metal ion coordination is present, free ethylenediamine molecules arrange between layers so that amino-hydrogen bonding to

chalcogenide or oxide ions stabilize the structure.[257,279–283] The hydrogen bonding interaction in these inorganic/organic hybrid materials stabilizes the structure, but also directs the inorganic constituents structure since hydrogen bonding is directional in nature.

There have been three main works which discuss possible crystal structures for ethylenediamine intercalated iron selenide, shown in Figure 5.9[86,247,255] Two of these works consider akali-metal co-intercalation while the other uses an alkali-metal free solvothermal method similar to the hydrothermal method considered in this work. All three have different solutions for how ethyelendiamine intercalates between FeSe layers determined through different methods, such as neutron powder diffraction and single crystal diffraction. For the two with alkali metal co-intercalation, the coordination of the ethylenediamine molecule to the alkali metal is different. The almost ubiquitous role ethylenediamine plays in coordination chemistry is well catalogued.[284,285] With regards to the first structure Figure 5.9 (left), the coordination of the ethylenediamine molecule to the sodium ion does not go through the nitrogen atoms but instead the carbon-carbon bond is proximate to the alkali metal. This is unlikely as the nitrogen atoms in ethylenediamine are strong Lewis bases for which coordination to the alkali metal should dominate. This structure was improved upon up the same authors in Figure 5.9 (center) where now monodentate or bridging ethylenediamine molecules arrange vertically between the FeSe layers and the FeSe layers are arranged in a primitive setting. Although this makes more sense from a coordination chemistry perspective, monodentate ethyelendiamine is very rare[286–289] as the two nitrogen atoms predominately form a bidentate to the same coordination site. Even amongst similar reaction schemes, the bidentate nature of ethylenediamine is well reported.[247,276–278]. The authors report that increasing Li content leads to the

transformation of the body centered stacking of the FeSe layers to the primitive setting. This may be due to the effects of Li-ethylenediamine coordination which leads to directional hydrogen bonding which guides the FeSe layers into the primitive setting through amino-hydrogen interactions with the selenide ions of the FeSe layers.[255] The stability of both of these intercalated compounds likely comes from electrostatic forces from the introduction of interlayer charged species; however, the arrangement of amino-hydrogens in the ethylenediamine molecules exhibit possible hydrogen bonding to selenide ions in the FeSe layers. In both of these cases, these compounds exhibit high superconducting critical temperatures, likely due to charge doping the FeSe layers, but without a concrete understanding of the interlayer species, determining the exact doping leading to this increased critical temperature is impossible.

For the last case, Figure 5.9 (right), without alkali metal co-intercalation, the ethylenediamine molecule is not coordinated to anything and is free between the FeSe layers. From this work, the reaction scheme requires Fe powder to be oxidized in solution to form the FeSe layers[247], thus the lack of Fe ion centered ethylenediamine coordination complexes is questionable as the formation of Fe ion centered ethylenediamine complexes in similar hydrothermal and solvothermal syntheses has been documented.[276–278] Since, no metal ion coordination exists electrostatic forces do not exist to stabilize the intercalation, thus requiring hydrogen bonding. Previous work on ammonia intercalation of FeSe[46] showed how hydrogens bonded to the nitrogen are directed toward the selenide ions leading to a bond distance of 2.75 Å consistent with weak hydrogen bonding observed in a wide range of works.[290] The structure reported by Stahl *et. al* has a closest N-H $\cdots$ Se distance of 3.63 Å which is outside the range for hydrogen bonding. Thus,

without the electrostatic forces due to metal ion-ethylenediamine coordination and no hydrogen bonding, it is hard to understand what stabilizes the structure in this case. In relation to the alkali metal intercalated phase, since no charged species exist in this system, there is no effective charge doping to the FeSe layers and may be one cause as to why superconductivity is not observed.[247]

The current work, without powder neutron diffraction or single crystal diffraction, does not allow for complete structural analysis. However, similar previous work on hydrothermal ammonia intercalation has showed proton intercalation plays the role of electrostatic stabilization and hydrogen bonding. Hydrogen bonding from the intercalated ammonia atoms was also determined to be significant through neutron powder diffraction analysis. Thus, it is likely that the hydrothermal method for ethylenediamine intercalation may exhibit proton co-intercalation similar to the ammonia case and significant hydrogen bonding from the hydrogens attached to the nitrogen directed at the chalcogenide ions. Current ED patterns for the hydrothermal ethylenediamine synthesis exhibit clear four fold symmetry due to the Fe sublattice in the iron chalcogenide layers. This rules out the formation of iron chalcogenide chains which has been observed in similar synthetic works.[247,276–278] Interesingly, in previous works using neat ethylenediamine only iron chalcogenide chains form,[247,276–278] whereas when a hydroxide source is added, glyercol[247] or water (in the current work), iron chalocogenide layers can be formed. This hints at a fundamental role hydroxide ions play in the synthesis of extended iron chalcogenide layers as opposed to chains. Further structural analysis of organic molecule intercalation in iron chalcogenides is needed to understand the role metal ion coordination plays in structural stabilization and charge doping to enhance superconductivity. In the

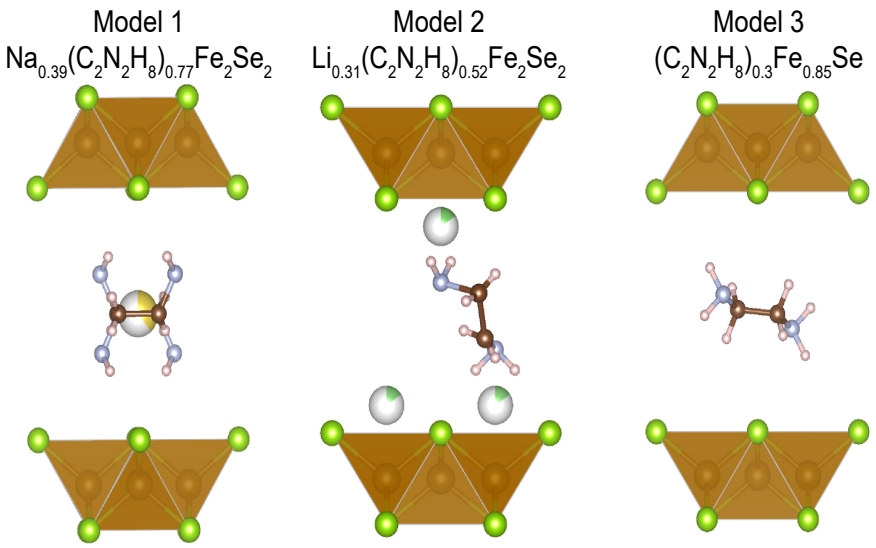

Fig. 5.9: Proposed structures for ethylenediamine intercalated FeSe from previous works.[86,247,255] Left/center depict alkali-metal stabilized ethylenediamine intercalation and right shows solvothermal alkali metal free ethylenediamine intercalated FeSe. Occupany and disorder for the ethylenediamine molecules have been simplfied for illustrative purposes.

case where metal ion coordination does not occur, hydrogen bonding must stabilize the structure which requires in-depth structural analysis through neutron and/or single crystal diffraction.

5.3.4 Magnetic and transport properties of intercalated species

Intercalation of various species between FeSe and FeS layers has shown to change the properties drastically, from enhancing superconductivity to inducing magnetic order. Previous work on alkali metal co-intercalated ethylenediamine showed an increase in critical temperature for FeSe from 8 K to 45 K[84,86,258,291] while superconductivity was suppressed in FeS displaying paramagnetic behavior.[254] For the case of intercalated FeSe species, the increase in critical temperature is understood to be a combination of effects due to an increase in adjacent FeSe layer distance as well as electron-doping from the

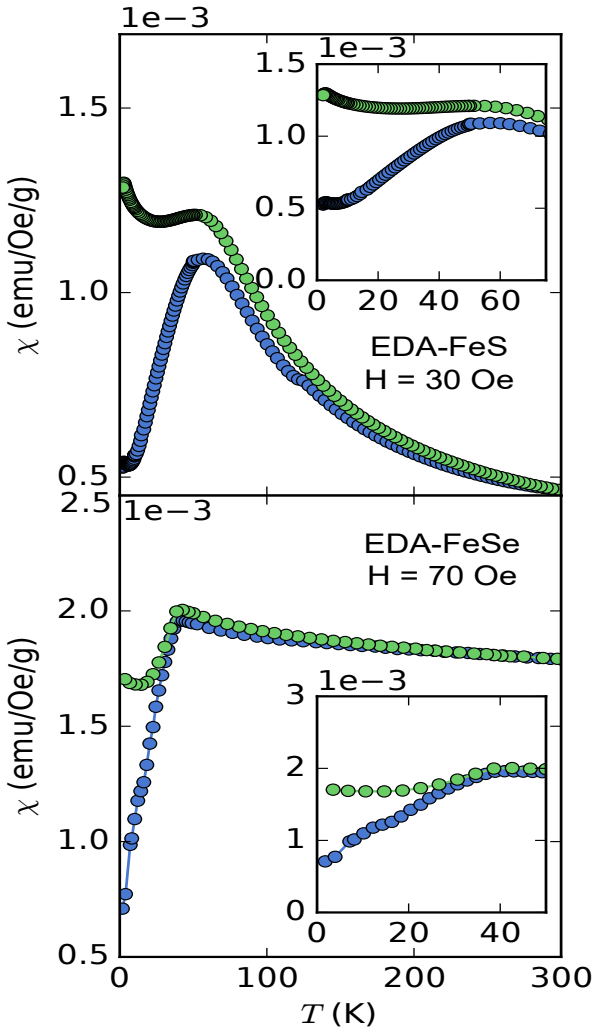

Fig. 5.10: Temperature dependence of magnetic susceptibility of $(C_2H_8N_2)_xFeS$ (top) and $(C_2H_8N_2)_yFeSe$ (bottom) at various applied fields. The insets show low temperature behavior for each species. For $(C_2H_8N_2)_xFeS$ a broad antiferromagnetic transition is shown at 55 K while for $(C_2H_8N_2)_yFeSe$ a clear transition is shown at 40 K which is superconducting-like in appearance at 70 Oe applied field.

intercalated species. Only one intercalated FeS species has been shown to increase the critical temperature[87] while the change to paramagnetic behavior is likely due to over-doping caused by the intercalated species. Figure 5.10 shows the temperature dependence of magnetic susceptibility for $(C_2H_8N_2)_xFeS$ and $(C_2H_8N_2)_yFeSe$ at various applied fields.

The magnetic susceptibility of $(C_2H_8N_2)_xFeS$ is shown in Figure 5.10 (top). At

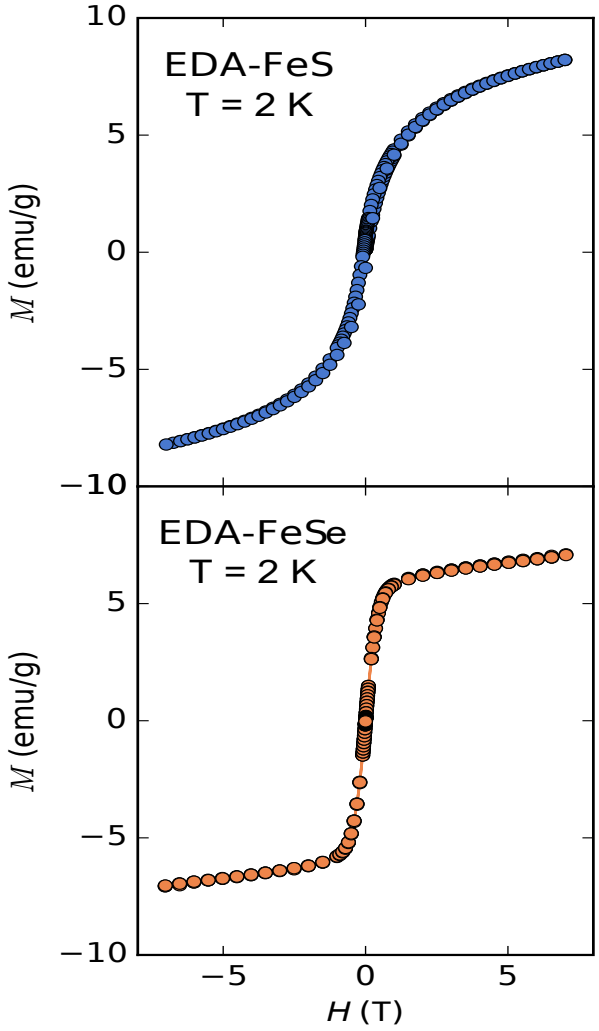

Fig. 5.11: Isothermal magnetization of $(C_2H_8N_2)_xFeS$ (top) and $(C_2H_8N_2)_yFeSe$ (bottom). $(C_2H_8N_2)_xFeS$ (top) shows weak hysteretic behavior at 2 K owning to possible canted antiferromagnetism or some remaining net moment in the sample down to base temperature. $(C_2H_8N_2)_yFeSe$ (bottom) shows antiferromagnetic behavior due to the overwhelming signal from possible impurity phases; no Meissner shielding is observed in the magnetization.

30 Oe applied field, a broad antiferromagnetic transition is observed at 55 K indicative of low-dimensional antiferromagnetic coupling. The absence of superconductivity is in agreement to other EDA intercalated FeS compounds.[248,254] The isothermal magnetization for $(C_2H_8N_2)_xFeS$ shown in Figure 5.11 (top) shows very weak hysteretic behavior likely due to ferrimagnetism or an uncompensated moment. Figure 5.10 (bottom)

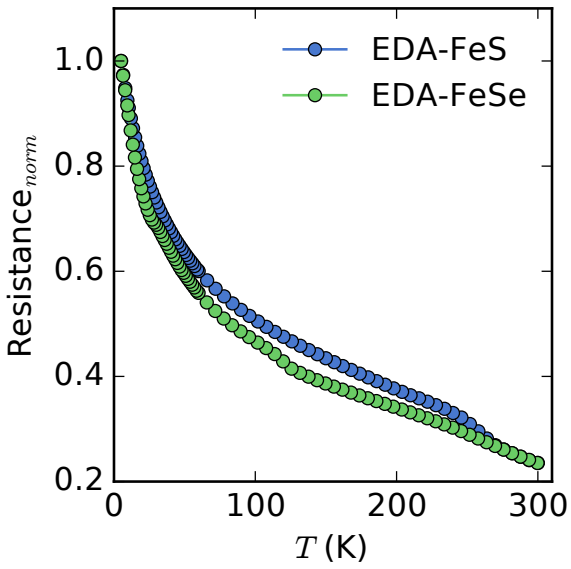

Fig. 5.12: Temperature dependence of resistance of pressed pellets of ground powders of $(C_2H_8N_2)_y$FeS and $(C_2H_8N_2)_x$FeSe. Both samples show semiconducting behavior with no features.

for $(C_2H_8N_2)_y$FeSe shows a clear transition in magnetic susceptibility at 70 Oe applied field. The transition at 40 K is highly reminiscent of a superconducting transition. Several previous studies on alkali metal and solvothermal ethylenediamine intercalated samples yielded superconducting samples with similar critical temperature.[84,86,246,258] Unfortunately, the parasitic contribution from the possible impurities does not allow us to see the true diamagnetic contribution and shielding volume fraction of the superconducting transition. Figure 5.11 shows the isothermal magnetization, which is dominated by the contribution from the impurity that masks the Meissner shielding.

Resistivity measurements were performed on pressed pellets of ground powders of $(C_2H_8N_2)_y$FeS and $(C_2H_8N_2)_x$FeSe using the standard four-probe method with silver paint as contacts. Figure 5.12 shows the temperature dependence of resistance of the samples. Both samples show semiconducting behavior with no transitions. Ethylenediamine inter-

calated into FeS by solvothermal methods showed similar behavior to our compounds, and pressed pellets of other FeS and intercalated FeS samples show semiconducting behavior even if the system is known to be metallic.[59,87,248,292] Previous solvothermal work on EDA-intercalated FeSe did not report resistance measurements, although superconducting transitions were observed in alkali metal co-intercalated FeSe samples that were metallic in the normal state.[258] Resistance measurements on pressed pellets may be highly effected by grain boundaries, surface oxidation, and high contact resistances. Annealing pressed pellets of each sample at 120 and 200 °C had no effect on the resistance measurements with both samples showing semiconducting behavior and no phase transitions.

5.4 Conclusion

We have successfully synthesized EDA-intercalated FeS and FeSe from a novel hydrothermal synthetic route. Previous solvothermal methods were only able to synthesize the selenide analogue and were not suitable for the metastable sulfide. The stabilization of the $(C_2H_8N_2)_y$FeS phase demonstrates the robustness and universality of our basic hydrothermal methods. In addition to cationic species and metal hydroxides, we have extended topotactic intercalation chemistry to small molecules (NH_3 and EDA) for Fe*Ch* using a generic facile hydrothermal route. The successful synthesis of neutral EDA-intercalated FeSe can help with precise determination of the electron doping level in comparison to alkali metal co-intercalated FeSe. The removal of the necessity of co-intercalating alkali metals to stabilize ethylenediamine intercalation in these iron chalcogenides points at the possible exploitation of hydrogen bonding as an important

factor for stabilizing and directing the structure and properties of novel organic-inorganic hybrid materials. To obtain high quality superconducting samples further optimization for the synthesis, such as D_2O, EDA and chalcogenide source concentrations, higher temperature and/or the addition of different mineralizers and solvents, is still required.

Chapter 6: Conclusions and Future Work

6.1 Conclusions

To summarize the entire dissertation, we have systematically targeted the class of materials known as tetrahedral transition metal chalcogenides (TTMCs) due to their structure and proximity to superconductivity in the iron chalcogenide family of superconductors. This class of materials offers a tremendous platform for exploration of interesting chemical and physical phenomena due to its tetrahedral coordination, square transition metal sublattice, and van der Waals layered structure. Through the use of this structure, we have explored topotactic synthetic routes through hydrothermal synthesis and other *chimie douce* techniques to synthesize metastable phases while retaining the important building block of the TTMC family.

We demonstrated that metastable layered tetragonal CoSe single crystals could be synthesized by a room temperature topochemical deintercalation of a thermodynamically stable template precursor, KCo_2Se_2, in highly basic aqueous media. In opposition to superconductivity in FeSe, CoSe displays spin glass like behavior with a signature magnetic transition at 10 K. We propose this spin glass behavior arises from magnetic frustration as opposed to conventional means due to lack of vacancies and other factors. Magnetic frustration in this compound likely arises from competing magnetic interaction of the square

transition metal sublattice as well as interlayer coupling of adjacent square lattices. Arrott plot analysis shows the moments likely lie in the *ab*-plane which is similar to the starting material KCo_2Se_2 except with a suppressed transition temperature and effective moment. Transport experiments show metallic behavior with no discernible anomoloues behavior around the transition temperature in resistivity or specific heat measurements.

When revisiting the iron chalcogenide system, we have moved past simple deintercalation and considered topochemical ion exchange through a hydrothermal synthetic route. Previous work on the (LiOH)FeSe system showed possible magnetism coexisting with superconductivity due to Fe ion substitution on the Li site in the LiOH layer of the compound. We have attempted to increase that magnetic signal by substituting other transition metal cations into the LiOH layer and in turn have developed a method for targeted doping of the LiOH layer without altering the FeSe layers. In particular, we have observed the formation of long range magnetic order in the 20% nominally doped Mn sample which is the first time long range order has been observed in this system. Neutron diffraction measurements show the onset of magnetic order is well within the superconducting state without significantly altering the superconducting properties of the system. As mentioned, we have expanded the work beyond Mn with other transition metals from Mn - Zn showing different doping behavior and physical properties depending on their chemical behavior. In total, this work shows that (LiOH)FeSe system offers a platform for guided chemical manipulation to induce the coexistence of long range magnetic order and superconductivity.

Beyond the intercalation of extended solids like LiOH, we have also expanded possible adducts to include organic molecules through a hydrothermal synthetic route.

Ethylenediamine intercalation of FeSe and FeS have been synthesized without the need for alkali metals which were required in previous works to stabilize the structure. The benefit of this is that charge doping is easier to understand as alkali metal co-intercalation often caused the formation of multiple charged species which makes the actual doping behavior of the interlayer species difficult to truly understand. Beyond that, this hydrothermal method expands the possible intercalants as long as they have some solubility in water at low temperature. The intercalation of organic molecules opens the window for hydrogen bonding as a possible mechanism for guided structure directing for how adjacent TTMC layers are stacked which could offer novel functionalities.

6.2 Future Work

The work described in this thesis only encapsulates a small piece of all the projects undertaken as a graduate student at University of Maryland. Some of the ongoing work offers a logical next step with regards to expanding the work described in this thesis and some new avenues of exploration are possible as well. One project which is currently ongoing but will require significant additional work is the expansion of the phase diagram as FeSe to changed to CoSe. Our work on the deintercalation method to form single crystals of CoSe offers a pathway for the stabilization of any concentration of $Fe_{1-x}Co_xSe$ to be formed as long as the starting material $KFe_{2-y}Co_ySe_2$ is able to be synthesized. To date, current work has been able to synthesize a number of concentrations along the phase diagram but one outstanding problem is that the starting material exhibits phase separation as true doping does not occur and KFe_2Se_2 and KCo_2Se_2 form separately as products.

This means that the deintercalated product may exhibit both FeSe and CoSe in different concentrations as opposed to doping. To start, a systematic study of the $KFe_{2-y}Co_ySe_2$ starting material would need to be employed in order to understand how to synthesize the material as a solid solution. From there, the process should be rather straightforward but the deintercalation conditions will likely need to be tuned depending on the cobalt concentration as the pure iron phase requires hydrothermal conditions and the pure cobalt case only requires room temperature conditions.

Beyond expanding the work on FeSe-CoSe, we would like to continue exploration of expanding the class of TTMC binaries to include other late transition metals. In particular, NiSe should be able to be synthesized from a reductive deintercalation reaction of KNi_2Se_2. Previous work and preliminary work in our lab has yet to find the correct conditions required to stabilize this compound. This composition would be particularly interesting because like the iron case, the KNi_2Se_2 is superconducting which means the deintercalated binary could offer a platform for additional studies of superconductivity. Along with Ni, the synthesis of any related binary or ternary phase would be interesting as the functionality of the square transition metal sublattice in incredible rich in its physical properties.

Although two of our works have been focused on the synthesis and properties of CoSe, additional works are still to be done with regards to magnetic order in the system. All magnetic and transport measurements have shown spin glass type behavior which has been corroborated by neutron diffraction. However, we do not understand why spin glass behavior develops in this system. To date, we explain this behavior as a function of interaction frustration as competing magnetic interactions on the square cobalt sublattice

and interlayer interactions compete to lead to no long range magnetic ordering. To that end, inelastic neutron spectroscopy should be employed to determine what spin fluctuations exist in this material at low temperatures which can be used to understand how these competing interactions lead to the suppression of long range order.

The current work on transition metal doping the (LiOH)FeSe system was limited to a maximum of nominally 20% for an initial investigation. However, due to the observation of long range magnetic order in the 20% Mn doped (LiOH)FeSe, a continuation of that work at higher doping level is warranted. Like the FeSe-CoSe diagram case, this requires that the formation of the $KFe_{2-y}M_ySe_2$ (M = Mn, Co, Ni, Cu, Zn) can be stabilized in the desired structure with doping rather than phase separation. The only two transition metals of particular interest would be Mn and Co which were shown to selectively dope the LiOH layer. Not included in this work is work done on the Cr-doped system. Preliminary work on Cr-doped KFe_2Se_2 shown the formation of a new layered phase at mild Cr content but we have not had the opportunity to follow up on that work. The unknown layered phase remained after hydrothermal cation exchange of the known Cr-doped KFe_2Se_2 phase.

The intercalation of organic molecules and extended hydroxide solids have opened an avenue for the exploration of the role hydrogen bonding can play on the stacking of adjacent layers. Hydrogen bonding is weak like van der Waals bonding but is not isotropic so the directionality of the hydrogen bond may be utilized to dictate the stacking of layers in this class of materials. In doing so, we may be able to show that rational design of heterolayer materials could be done through chemical means as opposed to the current paradigm of mechanical methods.

Finally, one project currently under work is the development of *in-situ* hydrothem-

ral x-ray diffraction techniques and experiments at 17-BM through collaboration with Dr. Andrey Yakovenko and Wenqian Xu. Research in our group has shown that the hydrothermal method is a tremendously powerful technique for the synthesis of iron chalcogenides and heterolayer materials. An example time-resolved x-ray diffraction powder pattern is shown in Figure 6.1 on the *in-situ* synthesis of (LiOH)FeS illustrating how the formation of products from starting materials can be shown in a time-resolved manner.

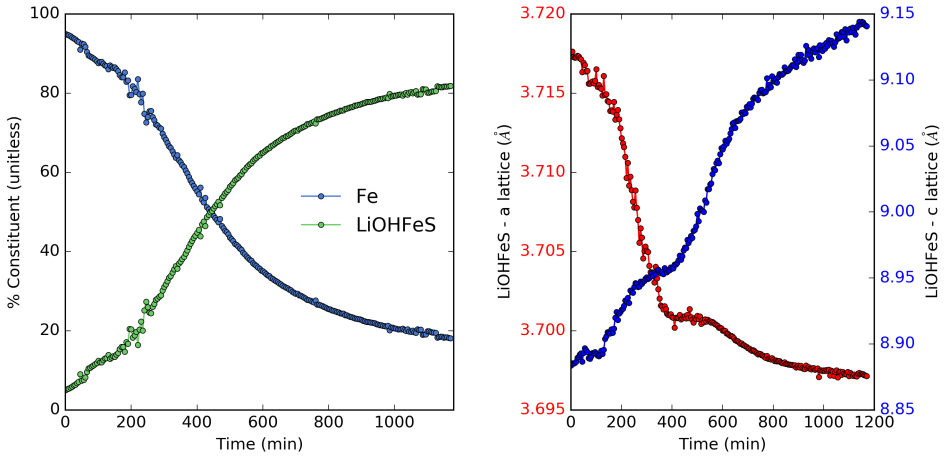

Fig. 6.1: Rietveld refinement results for *in-situ* synthesis of (LiOH)FeS showing the phase fraction of starting Fe powder and (LiOH)FeS product as a function of time with accompanying lattice parameter evolution of the (LiOH)FeS phase.

Thus, we have worked to develop a method in which x-ray diffraction patterns can be collected and analyzed in a high-throughput manner so that many different reactions and conditions can be scanned. We hope this work can shed light on how these metastable phases form and are stabilized in these reaction schemes. In addition, time resolved x-ray diffraction will allow kinetic analysis of the formation of these phases which is an under-studied aspect of hydrothermal synthesis. This work offers a light into the realm of hydrothermal synthesis of metastable materials and the associated kinetics which may reveal additional interesting avenues for research and exploitation.

Bibliography

[1] Kamerlingh Onnes, H. *Commun. Phys. Lab. Univ. Leiden, b* **1911**, *120*.

[2] Meissner, W.; Ochsenfeld, R. *Naturwissenschaften* **1933**, *21*, 787–788.

[3] Bardeen, J.; Cooper, L. N.; Schrieffer, J. R. *Physical review* **1957**, *108*, 1175.

[4] Tinkham, M. *Introduction to superconductivity*; Courier Corporation, 2004.

[5] Cooper, L. N. *Physical Review* **1956**, *104*, 1189.

[6] Pippard, A. B.; Bragg, W. L. *Proceedings of the Royal Society of London. Series A. Mathematical and Physical Sciences* **1953**, *216*, 547–568.

[7] London, F.; London, H.; Lindemann, F. A. *Proceedings of the Royal Society of London. Series A - Mathematical and Physical Sciences* **1935**, *149*, 71–88.

[8] Maxwell, E. *Physical Review* **1950**, *78*, 477.

[9] Fröhlich, H. *Proceedings of the Physical Society. Section A* **1950**, *63*, 778.

[10] McMillan, W. *Physical Review* **1968**, *167*, 331.

[11] Ashcroft, N. W. *Physical Review Letters* **1968**, *21*, 1748.

[12] Proust, C.; Taillefer, L. *Annual Review of Condensed Matter Physics* **2019**, *10*, 409–429.

[13] Tsuei, C.; Kirtley, J. *Reviews of Modern Physics* **2000**, *72*, 969.

[14] Park, C.; Snyder, R. L. *Journal of the American Ceramic Society* **1995**, *78*, 3171–3194.

[15] Norman, M.; Pepin, C. *Reports on Progress in Physics* **2003**, *66*, 1547.

[16] Wu, M. K.; Ashburn, J. R.; Torng, C. J.; Hor, P. H.; Meng, R. L.; Gao, L.; Huang, Z. J.; Wang, Y. Q.; Chu, C. W. *Phys. Rev. Lett.* **1987**, *58*, 908–910.

[17] Maeda, H.; Tanaka, Y.; Fukutomi, M.; Asano, T. *Japanese Journal of Applied Physics* **1988**, *27*, L209.

[18] *Physical Properties of High Temperature Superconductors*; John Wiley and Sons Ltd, 2015; Chapter 8, pp 151–164.

[19] Hüfner, S.; Hossain, M.; Damascelli, A.; Sawatzky, G. *Reports on Progress in Physics* **2008**, *71*, 062501.

[20] Shen, Z.-X.; Spicer, W.; King, D.; Dessau, D.; Wells, B. *Science* **1995**, *267*, 343–350.

[21] Malozemoff, A. P.; Mannhart, J.; Scalapino, D. *Phys. Today* **2005**, *58*, 41–6.

[22] Kamihara, Y.; Watanabe, T.; Hirano, M.; Hosono, H. *J. Amer. Chem. Soc.* **2008**, *130*, 3296–3297.

[23] Johnston, D. C. *Adv. Phys.* **2010**, *59*, 803–1061.

[24] Ishida, K.; Nakai, Y.; Hosono, H. *J. Phys. Soc. Jpn.* **2009**, *78*, 062001–062001.

[25] Wen, H.-H.; Li, S. *Annu. Rev. Condens. Matter Phys.* **2011**, *2*, 121–140.

[26] Wen, J.; Xu, G.; Gu, G.; Tranquada, J.; Birgeneau, R. *Rep. Prog. Phys* **2011**, *74*, 124503.

[27] Paglione, J.; Greene, R. L. *Nature Physics* **2010**, *6*, 645.

[28] Mazin, I. I. *Nature* **2010**, *464*, 183.

[29] Yang, W.; Sorini, A.; Chen, C.; Moritz, B.; Lee, W.-S.; Vernay, F.; Olalde-Velasco, P.; Denlinger, J.; Delley, B.; Chu, J.-H., et al. *Physical Review B* **2009**, *80*, 014508.

[30] Lu, D.; Yi, M.; Mo, S.-K.; Erickson, A.; Analytis, J.; Chu, J.-H.; Singh, D.; Hussain, Z.; Geballe, T.; Fisher, I., et al. *Nature* **2008**, *455*, 81.

[31] Lee, P. A.; Nagaosa, N.; Wen, X.-G. *Reviews of modern physics* **2006**, *78*, 17.

[32] Anderson, P. W. *science* **1987**, *235*, 1196–1198.

[33] Zhang, F.; Rice, T. *Physical Review B* **1988**, *37*, 3759.

[34] Stewart, G. *Reviews of Modern Physics* **2011**, *83*, 1589.

[35] Hirschfeld, P.; Korshunov, M.; Mazin, I. *Reports on Progress in Physics* **2011**, *74*, 124508.

[36] Cvetkovic, V.; Tesanovic, Z. *EPL (Europhysics Letters)* **2009**, *85*, 37002.

[37] Yin, Z.; Haule, K.; Kotliar, G. *Nature materials* **2011**, *10*, 932.

[38] Medici, L. d. *arXiv preprint arXiv:1707.03282* **2017**,

[39] Georges, A.; de'Medici, L.; Mravlje, J. **2013**,

[40] Fanfarillo, L.; Bascones, E. *Physical Review B* **2015**, *92*, 075136.

[41] Lanata, N.; Strand, H. U.; Giovannetti, G.; Hellsing, B.; de'Medici, L.; Capone, M. *Physical Review B* **2013**, *87*, 045122.

[42] Hsu, F.-C.; Luo, J.-Y.; Yeh, K.-W.; Chen, T.-K.; Huang, T.-W.; Wu, P. M.; Lee, Y.-C.; Huang, Y.-L.; Chu, Y.-Y.; Yan, D.-C.; Wu, M.-K. *Proc. Natl. Acad. Sci. USA* **2008**, *105*, 14262–14264.

[43] Kotegawa, H.; Masaki, S.; Awai, Y.; Tou, H.; Mizuguchi, Y.; Takano, Y. *J. Phys. Soc. Jpn.* **2008**, *77*, 113703.

[44] McQueen, T. M.; Huang, Q.; Ksenofontov, V.; Felser, C.; Xu, Q.; Zandbergen, H.; Hor, Y. S.; Allred, J.; Williams, A. J.; Qu, D., et al. *Physical Review B* **2009**, *79*, 014522.

[45] Margadonna, S.; Takabayashi, Y.; McDonald, M. T.; Kasperkiewicz, K.; Mizuguchi, Y.; Takano, Y.; Fitch, A. N.; Suard, E.; Prassides, K. *Chem. Comm.* **2008**, 5607–5609.

[46] Burrard-Lucas, M.; Free, D. G.; Sedlmaier, S. J.; Wright, J. D.; Cassidy, S. J.; Hara, Y.; Corkett, A. J.; Lancaster, T.; Baker, P. J.; Blundell, S. J., et al. *Nature Materials* **2013**, *12*, 15.

[47] Chen, W.; Zeng, C.; Kaxiras, E.; Zhang, Z. *Physical Review B* **2016**, *93*, 064517.

[48] Sun, H.; Woodruff, D. N.; Cassidy, S. J.; Allcroft, G. M.; Sedlmaier, S. J.; Thompson, A. L.; Bingham, P. A.; Forder, S. D.; Cartenet, S.; Mary, N., et al. *Inorganic Chemistry* **2015**, *54*, 1958–1964.

[49] Margadonna, S.; Takabayashi, Y.; Ohishi, Y.; Mizuguchi, Y.; Takano, Y.; Kagayama, T.; Nakagawa, T.; Takata, M.; Prassides, K. *Physical Review B* **2009**, *80*, 064506.

[50] He, S.; He, J.; Zhang, W.; Zhao, L.; Liu, D.; Liu, X.; Mou, D.; Ou, Y.-B.; Wang, Q.-Y.; Li, Z., et al. *Nat. Mater.* **2013**, *12*, 605.

[51] Böhmer, A. E.; Arai, T.; Hardy, F.; Hattori, T.; Iye, T.; Wolf, T.; Löhneysen, H. v.; Ishida, K.; Meingast, C. *Physical Review Letters* **2015**, *114*, 027001.

[52] Wang, Q.; Shen, Y.; Pan, B.; Zhang, X.; Ikeuchi, K.; Iida, K.; Christianson, A.; Walker, H.; Adroja, D.; Abdel-Hafiez, M., et al. *Nature Communications* **2016**, *7*, 12182.

[53] Rahn, M. C.; Ewings, R. A.; Sedlmaier, S. J.; Clarke, S. J.; Boothroyd, A. T. *Physical Review B* **2015**, *91*, 180501(R).

[54] Wang, Q.; Shen, Y.; Pan, B.; Hao, Y.; Ma, M.; Zhou, F.; Steffens, P.; Schmalzl, K.; Forrest, T.; Abdel-Hafiez, M., et al. *Nature Materials* **2016**, *15*, 159.

[55] Pomjakushina, E.; Conder, K.; Pomjakushin, V.; Bendele, M.; Khasanov, R. *Phys. Rev. B* **2009**, *80*, 024517.

[56] Koz, C.; Schmidt, M.; Borrmann, H.; Burkhardt, U.; Robler, S.; Carrillo-Cabrera, W.; Schnelle, W.; Schwarz, U.; Grin, Y. *Z. Anorg. Allg. Chem* **2014**, *640*, 1600–1606.

[57] Greenfield, J. T.; Kamali, S.; Lee, K.; Kovnir, K. *Chem. Mater.* **2015**, *27*, 588–596.

[58] Lai, X.; Zhang, H.; Wang, Y.; Wang, X.; Zhang, X.; Lin, J.; Huang, F. *J. Am. Chem. Soc.* **2015**, *137*, 10148–10151.

[59] Borg, C. K. H.; Zhou, X.; Eckberg, C.; Campbell, D. J.; Saha, S. R.; Paglione, J.; Rodriguez, E. E. *Phys. Rev. B* **2016**, *93*, 094522.

[60] Evans Jr, H. T.; Milton, C.; Chao, E.; Adler, I.; Mead, C.; Ingram, B.; Berner, R. A. *US Geological Survey Professional Paper* **1964**, *475*, 64–69.

[61] Zhou, X.; Wilfong, B.; Vivanco, H.; Paglione, J.; Brown, C. M.; Rodriguez, E. E. *J. Am. Chem. Soc* **2016**, *138*, 16432–16442, PMID: 27935693.

[62] Schuster, W.; Mikler, H.; Komarek, K. L. *Monatshefte für Chemie/Chemical Monthly* **1979**, *110*, 1153–1170.

[63] Zhou, X.; Rodriguez, E. E. *Chem. Mater.* **2017**, *29*, 5737–5752.

[64] Hoffmann, R.; Zheng, C. *The Journal of Physical Chemistry* **1985**, *89*, 4175–4181.

[65] Zheng, C.; Hoffmann, R. *Journal of Solid State Chemistry* **1988**, *72*, 58 – 71.

[66] Hoffmann, R. *Angewandte Chemie International Edition in English* **1987**, *26*, 846–878.

[67] Burdett, J. K. *Progress in Solid State Chemistry* **1984**, *15*, 173 – 255.

[68] Papoian, G.; Hoffmann, R. *Journal of the American Chemical Society* **2001**, *123*, 6600–6608, PMID: 11439046.

[69] Tremel, W.; Hoffmann, R. *Journal of the American Chemical Society* **1987**, *109*, 124–140.

[70] Chandra, P.; Doucot, B. *Phys. Rev. B* **1988**, *38*, 9335–9338.

[71] Shannon, N.; Momoi, T.; Sindzingre, P. *Phys. Rev. Lett.* **2006**, *96*, 027213.

[72] Vannimenus, J.; Toulouse, G. *Journal of Physics C: Solid State Physics* **1977**, *10*, L537–L542.

[73] Skoulatos, M.; Goff, J. P.; Geibel, C.; Kaul, E. E.; Nath, R.; Shannon, N.; Schmidt, B.; Murani, A. P.; Deen, P. P.; Enderle, M.; Wildes, A. R. *EPL (Europhysics Letters)* **2009**, *88*, 57005.

[74] Schmidt, B.; Thalmeier, P.; Shannon, N. *Physical review B* **2007**, *76*, 125113.

[75] Wilfong, B.; Zhou, X.; Vivanco, H.; Campbell, D. J.; Wang, K.; Graf, D.; Paglione, J.; Rodriguez, E. *Phys. Rev. B* **2018**, *97*, 104408.

[76] Dagotto, E. *Rev. Mod. Phys.* **2013**, *85*, 849.

[77] Guo, J.; Jin, S.; Wang, G.; Wang, S.; Zhu, K.; Zhou, T.; He, M.; Chen, X. *Phys. Rev. B.* **2010**, *82*, 180520.

[78] Yan, X.-W.; Gao, M.; Lu, Z.-Y.; Xiang, T. *Phys. Rev. B.* **2011**, *84*, 054502.

[79] Dong, X.; Jin, K.; Yuan, D.; Zhou, H.; Yuan, J.; Huang, Y.; Hua, W.; Sun, J.; Zheng, P.; Hu, W.; Mao, Y.; Ma, M.; Zhang, G.; Zhou, F.; Zhao, Z. *Physical Review B* **2015**, *92*, 064515.

[80] Pachmayr, U.; Nitsche, F.; Luetkens, H.; Kamusella, S.; Brückner, F.; Sarkar, R.; Klauss, H.-H.; Johrendt, D. *Angewandte Chemie International Edition* **2015**, *54*, 293–297.

[81] Lynn, J. W.; Zhou, X.; Borg, C. K. H.; Saha, S. R.; Paglione, J.; Rodriguez, E. E. *Physical Review B* **2015**, *92*, 060510(R).

[82] Zhou, X.; Borg, C. K. H.; Lynn, J. W.; Saha, S. R.; Paglione, J.; Rodriguez, E. E. *J. Mater. Chem. C* **2016**, *4*, 3934–3941.

[83] Hosono, S.; Noji, T.; Hatakeda, T.; Kawamata, T.; Kato, M.; Koike, Y. *J. Phys. Soc. Jpn.* **2014**, *83*, 113704.

[84] Noji, T.; Hatakeda, T.; Hosono, S.; Kawamata, T.; Kato, M.; Koike, Y. *Phys. C: Supercon. and App.* **2014**, *504*, 8–11.

[85] Krzton-Maziopa, A.; Pomjakushina, E.; Pomjakushin, V. Y.; Von Rohr, F.; Schilling, A.; Conder, K. *J. Phys. Condens. Matter* **2012**, *24*, 382202.

[86] Jin, S.; Fan, X.; Wu, X.; Sun, R.; Wu, H.; Huang, Q.; Shi, C.; Xi, X.; Li, Z.; Chen, X. *Chem. Comm.* **2017**, *53*, 9729–9732.

[87] Zhou, X.; Eckberg, C.; Wilfong, B.; Liou, S.-C.; Vivanco, H. K.; Paglione, J.; Rodriguez, E. E. *Chem. Sci.* **2017**, *8*, 3781–3788.

[88] Li, Z.; Pradeep, K. G.; Deng, Y.; Raabe, D.; Tasan, C. C. *Nature* **2016**, *534*, 227–230.

[89] Stein, A.; Keller, S. W.; Mallouk, T. E. *Science* **1993**, *259*, 1558–1564.

[90] Gopalakrishnan, J. *Chem. Mater.* **1995**, *7*, 1265–1275.

[91] Pervov, V.; Manokhina, E.; Dobrokhotova, Z. V.; Zotova, A.; Zavrazhnov, A. Y. *Inorganic materials* **2011**, *47*, 1407–1427.

[92] Berner, R. A. *The Journal of Geology* **1964**, *72*, 293–306.

[93] Lennie, A. R.; Redfern, S. A.; Champness, P. E.; Stoddart, C. P.; Schofield, P. F.; Vaughan, D. J. *American Mineralogist* **1997**, *82*, 302–309.

[94] Lennie, A.; Redfern, S. A.; Schofield, P.; Vaughan, D. *Mineralogical Magazine* **1995**, *59*, 677–683.

[95] Rouxel, J.; Tournoux, M. *Solid State Ionics* **1996**, *84*, 141–149.

[96] Livage, J. *New Journal of Chemistry* **2001**, *25*, 1–1.

[97] Corriu, R. J. *New Journal of Chemistry* **2001**, *25*, 2–2.

[98] Rüdorff, W. *Advances in inorganic chemistry and radiochemistry*; Elsevier, 1959; Vol. 1; pp 223–266.

[99] DiSalvo, F.; Safran, S.; Haddon, R.; Waszczak, J.; Fischer, J. *Physical Review B* **1979**, *20*, 4883.

[100] Gamble, F.; Osiecki, J.; Cais, M.; Pisharody, R.; DiSalvo, F.; Geballe, T. *Science* **1971**, *174*, 493–497.

[101] Whittingha, S. M. *Intercalation chemistry*; Elsevier, 2012.

[102] Dresselhaus, M.; Dresselhaus, G. *Advances in Physics* **1981**, *30*, 139–326.

[103] Whittingham, M. S. *Science* **1976**, *192*, 1126–1127.

[104] Li, Y. J.; Whittingham, M. S. *Solid State Ionics* **1993**, *63*, 391–395.

[105] Whittingham, M. S. *Current Opinion in Solid State and Materials Science* **1996**, *1*, 227–232.

[106] Rajamathi, M.; Seshadri, R. *Current Opinion in Solid State and Materials Science* **2002**, *6*, 337–345.

[107] Yaghi, O.; Li, H. *Journal of the American Chemical Society* **1995**, *117*, 10401–10402.

[108] Yang, S.; Zavalij, P. Y.; Whittingham, M. S. *Electrochemistry Communications* **2001**, *3*, 505–508.

[109] Feng, S.; Xu, R. *Accounts of chemical research* **2001**, *34*, 239–247.

[110] Norton, D. L. *Annual Review of Earth and Planetary Sciences* **1984**, *12*, 155–177.

[111] Tarasov, V.; Gebruk, A.; Mironov, A.; Moskalev, L. *Chemical Geology* **2005**, *224*, 5–39.

[112] Martin, W.; Baross, J.; Kelley, D.; Russell, M. J. *Nature Reviews Microbiology* **2008**, *6*, 805–814.

[113] Russell, M.; Hall, A.; Cairns-Smith, A.; Braterman, P. *Nature* **1988**, *336*, 117–117.

[114] Byrappa, K. *Springer Handbook of Crystal Growth*; Springer, 2010; pp 599–653.

[115] Byrappa, K.; Yoshimura, M. *Handbook of hydrothermal technology*; William Andrew, 2012.

[116] Rabenau, A. *Angewandte Chemie International Edition in English* **1985**, *24*, 1026–1040.

[117] Rudolph, P. *Handbook of crystal growth: Bulk crystal growth*; Elsevier, 2014.

[118] Channei, D.; Phanichphant, S.; Nakaruk, A.; Mofarah, S. S.; Koshy, P.; Sorrell, C. C. *Catalysts* **2017**, *7*, 45.

[119] Bonomi, F.; Werth, M. T.; Kurtz, D. M. *Inorganic Chemistry* **1985**, *24*, 4331–4335.

[120] Zhou, X. Intercalation Chemistry of Tetrahedral Transition Metal Chalcogenides. Ph.D. thesis, 2018; Copyright - Database copyright ProQuest LLC; ProQuest does not claim copyright in the individual underlying works; Last updated - 2019-10-19.

[121] Zhou, X.; Wang, L.; Fan, X.; Wilfong, B.; Liou, S.-C.; Wang, Y.; Zheng, H.; Feng, Z.; Wang, C.; Rodriguez, E. E. *Chemistry of Materials* **2020**, *32*, 769–775.

[122] Neilson, J. R.; McQueen, T. M. *Journal of the American Chemical Society* **2012**, *134*, 7750–7757.

[123] Vivanco, H. K.; Rodriguez, E. E. *J. Solid State Chem* **2016**, *242, Part 2*, 3 – 21, Solid State Chemistry of Energy-Related Materials.

[124] Lu, X.; Wang, N.; Wu, H.; Wu, Y.; Zhao, D.; Zeng, X.; Luo, X.; Wu, T.; Bao, W.; Zhang, G., et al. *Nature Materials* **2015**, *14*, 325.

[125] Shoemaker, D. P.; Chung, D. Y.; Claus, H.; Francisco, M. C.; Avci, S.; Llobet, A.; Kanatzidis, M. G. *Physical Review B* **2012**, *86*, 184511.

[126] Coelho, A. A. *Journal of Applied Crystallography* **2018**, *51*, 210–218.

[127] Cheary, R. W.; Coelho, A. *Journal of Applied Crystallography* **1992**, *25*, 109–121.

[128] Pecharsky, V.; Zavalij, P. *Fundamentals of powder diffraction and structural characterization of materials*; Springer Science & Business Media, 2008.

[129] Squires, G. L. *Introduction to the theory of thermal neutron scattering*; Courier Corporation, 1996.

[130] Pynn, R. *Neutron Scattering: A Primer*; Los Alamos Neutron Science Center, 1990.

[131] Spaldin, N. A. *Magnetic materials: fundamentals and applications*; Cambridge university press, 2010.

[132] Blundell, S. *Magnetism in Condensed Matter*; Magnetism in Condensed Matter, 2001.

[133] MPMS 3 User's Manual. Quantum Design: 11578 Sorrento Valley Rd., San Diego, CA 92121-1311 USA, 2016.

[134] Kittel, C. *Introduction to Solid State Physics*; Wiley, 2005.

[135] Kleiner, R.; Koelle, D.; Ludwig, F.; Clarke, J. *Proceedings of the IEEE* **2004**, *92*, 1534–1548.

[136] PPMS DynaCool Options Manual. Quantum Design: 11578 Sorrento Valley Rd., San Diego, CA 92121-1311 USA, 2014.

[137] Mydosh, J. A. *Spin Glasses: An Experimental Introduction*; Taylor and Francis, 1993.

[138] Mydosh, J. *J. Magn. Magn. Mater.* **1996**, *157*, 606–610.

[139] Binder, K.; Young, A. P. *Rev. Mod. Phys* **1986**, *58*, 801.

[140] Physical Property Measurement System AC Measurement System (ACMS) Option User's Manual. Quantum Design: 11578 Sorrento Valley Rd., San Diego, CA 92121-1311 USA, 2003.

[141] Physical Property Measurement System Resistivity Option User's Manual. Quantum Design: 11578 Sorrento Valley Rd., San Diego, CA 92121-1311 USA, 1999.

[142] Physical Property Measurement System Heat Capacity Option User's Manual. Quantum Design: 11578 Sorrento Valley Rd., San Diego, CA 92121-1311 USA, 2004.

[143] Bachmann, R.; DiSalvo, F. J.; Geballe, T. H.; Greene, R. L.; Howard, R. E.; King, C. N.; Kirsch, H. C.; Lee, K. N.; Schwall, R. E.; Thomas, H.; Zubeck, R. B. *Rev. Sci. Instrum.* **1972**, *43*, 205–214.

[144] Hohenberg, P.; Kohn, W. *Phys. Rev.* **1964**, *136*, B864–B871.

[145] Kohn, W.; Sham, L. J. *Phys. Rev.* **1965**, *137*, A1697–A1705.

[146] Kresse, G. Title. Ph.D. thesis, Technische Universiät Wien, 1993.

[147] Kresse, G.; Hafner, J. *Phys. Rev. B* **1993**, *47*, 558–561.

[148] Kresse, G.; Furthmüller, J. *Comput. Mater. Sci.* **1996**, *6*, 15 – 50.

[149] Kresse, G.; Furthmüller, J. *Phys. Rev. B* **1996**, *54*, 11169–11186.

[150] Blöchl, P. E. *Phys. Rev. B* **1994**, *50*, 17953–17979.

[151] Perdew, J. P.; Burke, K.; Ernzerhof, M. *Phys. Rev. Lett.* **1996**, *77*, 3865–3868.

[152] Monkhorst, H. J.; Pack, J. D. *Phys. Rev. B* **1976**, *13*, 5188–5192.

[153] Martin, R. M.; Martin, R. M. *Electronic structure: basic theory and practical methods*; Cambridge university press, 2004.

[154] Koch, W.; Holthausen, M. C. *A chemist's guide to density functional theory*; John Wiley & Sons, 2015.

[155] Williams, A. J.; McQueen, T. M.; Ksenofontov, V.; Felser, C.; Cava, R. J. *J. Phys. Condens. Matter* **2009**, *21*, 305701.

[156] Wu, M.; Hsu, F.; Yeh, K.; Huang, T.; Luo, J.; Wang, M.; Chang, H.; Chen, T.; Rao, S.; Mok, B., et al. *Physica C Supercond.* **2009**, *469*, 340–349.

[157] Urata, T.; Tanabe, Y.; Huynh, K. K.; Oguro, H.; Watanabe, K.; Tanigaki, K. *arXiv preprint arXiv:1608.01044* **2016**,

[158] Mizuguchi, Y.; Tomioka, F.; Tsuda, S.; Yamaguchi, T.; Takano, Y. *J. Phys. Soc. Jpn.* **2009**, *78*, 074712–074712.

[159] Sines, I. T.; II, D. D. V.; Misra, R.; Popczun, E. J.; Schaak, R. E. *J. Solid State Chem.* **2012**, *196*, 17 – 20.

[160] Denholme, S.; Demura, S.; Okazaki, H.; Hara, H.; Deguchi, K.; Fujioka, M.; Ozaki, T.; Yamaguchi, T.; Takeya, H.; Takano, Y. *Mater. Chem. Phys.* **2014**, *147*, 50 – 56.

[161] Lei, H.; Abeykoon, M.; Bozin, E. S.; Petrovic, C. *Phys. Rev. B* **2011**, *83*, 180503.

[162] Oledzka, M.; Ramanujachary, K.; Greenblatt, M. *Mater. Res. Bull.* **1998**, *33*, 855 – 866.

[163] Oledzka, M.; Lee, J.-G.; Ramanujachary, K.; Greenblatt, M. *J. Solid State Chem.* **1996**, *127*, 151 – 160.

[164] Huan, G.; Greenblatt, M.; Croft, M. *Eur. J. Solid State Inorg. Chem.* **1989**, *26*, 193–220.

[165] Bouroushian, M. *Electrochemistry of metal chalcogenides*; Springer, 2010; pp 57–75.

[166] Wen, H.-H.; Li, S. *Annu. Rev. Condens. Matter Phys.* **2011**, *2*, 121–140.

[167] Rodriguez, E. E.; Stock, C.; Zajdel, P.; Krycka, K. L.; Majkrzak, C. F.; Zavalij, P.; Green, M. A. *Phys. Rev. B* **2011**, *84*, 064403.

[168] Rodriguez, E. E.; Sokolov, D. A.; Stock, C.; Green, M. A.; Sobolev, O.; Rodriguez-Rivera, J. A.; Cao, H.; Daoud-Aladine, A. *Phys. Rev. B* **2013**, *88*, 165110.

[169] Stock, C.; Rodriguez, E. E.; Green, M. A. *Phys. Rev. B* **2012**, *85*, 094507.

[170] Zhang, X.; Oh, Y. S.; Liu, Y.; Yan, L.; Saha, S. R.; Butch, N. P.; Kirshenbaum, K.; Kim, K. H.; Paglione, J.; Greene, R. L.; Takeuchi, I. *Phys. Rev. B* **2010**, *82*, 020515.

[171] Quirinale, D. G.; Anand, V. K.; Kim, M. G.; Pandey, A.; Huq, A.; Stephens, P. W.; Heitmann, T. W.; Kreyssig, A.; McQueeney, R. J.; Johnston, D. C.; Goldman, A. I. *Phys. Rev. B* **2013**, *88*, 174420.

[172] Anand, V. K.; Dhaka, R. S.; Lee, Y.; Harmon, B. N.; Kaminski, A.; Johnston, D. C. *Phys. Rev. B* **2014**, *89*, 214409.

[173] Jayasekara, W.; Lee, Y.; Pandey, A.; Tucker, G. S.; Sapkota, A.; Lamsal, J.; Calder, S.; Abernathy, D. L.; Niedziela, J. L.; Harmon, B. N.; Kreyssig, A.; Vaknin, D.; Johnston, D. C.; Goldman, A. I.; McQueeney, R. J. *Phys. Rev. Lett.* **2013**, *111*, 157001.

[174] Pandey, A.; Quirinale, D.; Jayasekara, W.; Sapkota, A.; Kim, M.; Dhaka, R.; Lee, Y.; Heitmann, T.; Stephens, P.; Ogloblichev, V., et al. *Phys. Rev. B* **2013**, *88*, 014526.

[175] Anand, V. K.; Quirinale, D. G.; Lee, Y.; Harmon, B. N.; Furukawa, Y.; Ogloblichev, V. V.; Huq, A.; Abernathy, D. L.; Stephens, P. W.; McQueeney, R. J.; Kreyssig, A.; Goldman, A. I.; Johnston, D. C. *Phys. Rev. B* **2014**, *90*, 064517.

[176] Mansart, J.; Le Fèvre, P.; Bertran, F. m. c.; Forget, A.; Colson, D.; Brouet, V. *Phys. Rev. B* **2016**, *94*, 235147.

[177] Kovnir, K.; Garlea, V. O.; Thompson, C. M.; Zhou, H.; Reiff, W. M.; Ozarowski, A.; Shatruk, M. *Inorg. Chem.* **2011**, *50*, 10274–10283.

[178] Tan, X.; Fabbris, G.; Haskel, D.; Yaroslavtsev, A. A.; Cao, H.; Thompson, C. M.; Kovnir, K.; Menushenkov, A. P.; Chernikov, R. V.; Garlea, V. O.; Shatruk, M. *J. Am. Chem. Soc.* **2016**, *138*, 2724–2731.

[179] Physical Property Measurement System Heat Capacity Option User's Manual. Quantum Design: 11578 Sorrento Valley Rd., San Diego, CA 92121-1311 USA, 2004.

[180] Hwang, J. S.; Lin, K. J.; Tien, C. *Rev. Sci. Instrum.* **1997**, *68*, 94–101.

[181] Balents, L. *Nature* **2010**, *464*, 199–208.

[182] Shtrikman, S.; Wohlfarth, E. *Phys. Lett. A* **1981**, *85*, 467–470.

[183] Souletie, J.; Tholence, J. L. *Phys. Rev. B* **1985**, *32*, 516–519.

[184] Ogielski, A. T.; Morgenstern, I. *Phys. Rev. Lett.* **1985**, *54*, 928–931.

[185] Ogielski, A. T. *Phys. Rev. B* **1985**, *32*, 7384–7398.

[186] Yang, J.; Chen, B.; Wang, H.; Mao, Q.; Imai, M.; Yoshimura, K.; Fang, M. *Phys. Rev. B* **2013**, *88*, 064406.

[187] Yelland, E.; Yates, S.; Taylor, O.; Griffiths, A.; Hayden, S.; Carrington, A. *Phys. Rev. B* **2005**, *72*, 184436.

[188] Bhattacharyya, A.; Jain, D.; Ganesan, V.; Giri, S.; Majumdar, S. *Phys. Rev. B* **2011**, *84*, 184414.

[189] Liu, Z.; Zhao, Y.; Li, Y.; Jia, L.; Cai, Y.; Zhou, S.; Xia, T.; Büchner, B.; Borisenko, S.; Wang, S. *J. Phys. Condens. Matter* **2015**, *27*, 295501.

[190] Kaul, S. N. *J. Phys.: Condens. Matter* **1999**, *11*, 7597.

[191] Moriya, T. *J. Magn. Magn. Mater.* **1979**, *14*, 1–46.

[192] Tari, A. *The Specific Heat of Matter at Low Temperatures*; World Scientific, 2003.

[193] Mohn, P. *Magnetism in the Solid State: An Introduction*; Springer Science & Business Media, 2006; Vol. 134.

[194] Johnston, D. C. *Phys. Rev. Lett.* **2012**, *109*, 077201.

[195] Yu, R.; Si, Q. *Phys. Rev. Lett.* **2015**, *115*, 116401.

[196] Ma, F.; Ji, W.; Hu, J.; Lu, Z.-Y.; Xiang, T. *Phys. Rev. Lett.* **2009**, *102*, 177003.

[197] Wang, F.; Kivelson, S. A.; Lee, D.-H. *Nature Phys.* **2015**, *11*.

[198] Glasbrenner, J.; Mazin, I.; Jeschke, H. O.; Hirschfeld, P.; Fernandes, R.; Valentí, R. *Nature Phys.* **2015**, *11*, 953–958.

[199] Shannon, N.; Schmidt, B.; Penc, K.; Thalmeier, P. *Eur. Phys. J. B* **2004**, *38*, 599–616.

[200] Liu, Z.-H.; Richard, P.; Xu, N.; Xu, G.; Li, Y.; Fang, X.-C.; Jia, L.-L.; Chen, G.-F.; Wang, D.-M.; He, J.-B., et al. *Phys. Rev. Lett.* **2012**, *109*, 037003.

[201] Qian, T.; Wang, X.-P.; Jin, W.-C.; Zhang, P.; Richard, P.; Xu, G.; Dai, X.; Fang, Z.; Guo, J.-G.; Chen, X.-L.; Ding, H. *Phys. Rev. Lett.* **2011**, *106*, 187001.

[202] Wang, G.; Yi, X.; Shi, X. *Physics Letters A* **2015**, *379*, 2106–2109.

[203] Zhang, G.-Y.; Chou, M.; Lin, C.-T. *Crystals* **2017**, *7*, 167.

[204] Topping, C. V.; Kirschner, F. K. K.; Blundell, S. J.; Baker, P. J.; Woodruff, D. N.; Schild, F.; Sun, H.; Clarke, S. J. *Physical Review B* **2017**, *95*, 134419.

[205] Wu, Y. P.; Zhao, D.; Lian, X. R.; Lu, X. F.; Wang, N. Z.; Luo, X. G.; Chen, X. H.; Wu, T. *Physical Review B* **2015**, *91*, 125107.

[206] Lynn, J.; Moncton, D.; Thomlinson, W.; Shirane, G.; Shelton, R. *Solid State Communications* **1978**, *26*, 493–496.

[207] Lynn, J.; Moncton, D.; Shirane, G.; Thomlinson, W.; Eckert, J.; Shelton, R. *Journal of Applied Physics* **1978**, *49*, 1389–1391.

[208] Moncton, D. E.; Shirane, G.; Thomlinson, W.; Ishikawa, M.; Fischer, O. *Physical Review Letters* **1978**, *41*, 1133.

[209] Lynn, J.; Shelton, R.; Horng, H.-E.; Glinka, C. *Physica B+ C* **1983**, *120*, 224–226.

[210] Lynn, J. W.; Skanthakumar, S.; Huang, Q.; Sinha, S. K.; Hossain, Z.; Gupta, L. C.; Nagarajan, R.; Godart, C. *Phys. Rev. B* **1997**, *55*, 6584–6598.

[211] Gupta, L. *Advances in Physics* **2006**, *55*, 691–798.

[212] Grigereit, T. E.; Lynn, J. W.; Huang, Q.; Santoro, A.; Cava, R. J.; Krajewski, J. J.; Peck, W. F. *Phys. Rev. Lett.* **1994**, *73*, 2756–2759.

[213] Lynn, J. W.; Keimer, B.; Ulrich, C.; Bernhard, C.; Tallon, J. L. *Phys. Rev. B* **2000**, *61*, R14964–R14967.

[214] Tokunaga, Y.; Kotegawa, H.; Ishida, K.; Kitaoka, Y.; Takagiwa, H.; Akimitsu, J. *Physical Review Letters* **2001**, *86*, 5767.

[215] Lynn, J. W.; Clinton, T. W.; Li, W.-H.; Erwin, R. W.; Liu, J. Z.; Vandervoort, K.; Shelton, R. N. *Phys. Rev. Lett.* **1989**, *63*, 2606–2609.

[216] Lynn, J. W.; Dai, P. *Physica C: Superconductivity* **2009**, *469*, 469–476.

[217] Xiao, Y.; Su, Y.; Meven, M.; Mittal, R.; Kumar, C. M. N.; Chatterji, T.; Price, S.; Persson, J.; Kumar, N.; Dhar, S. K.; Thamizhavel, A.; Brueckel, T. *Physical Review B* **2009**, *80*, 174424.

[218] Nandi, S.; Jin, W. T.; Xiao, Y.; Su, Y.; Price, S.; Shukla, D. K.; Strempfer, J.; Jeevan, H. S.; Gegenwart, P.; Brückel, T. *Physical Review B* **2014**, *89*, 014512.

[219] Bao, J.-K.; Willa, K.; Smylie, M. P.; Chen, H.; Welp, U.; Chung, D. Y.; Kanatzidis, M. G. *Crystal Growth & Design* **2018**, *18*, 3517–3523.

[220] Stolyarov, V. S.; Veshchunov, I. S.; Grebenchuk, S. Y.; Baranov, D. S.; Golovchanskiy, I. A.; Shishkin, A. G.; Zhou, N.; Shi, Z.; Xu, X.; Pyon, S., et al. *Science Advances* **2018**, *4*, eaat1061.

[221] Watson, M. D.; Kim, T. K.; Rhodes, L. C.; Eschrig, M.; Hoesch, M.; Haghighirad, A. A.; Coldea, A. I. *Physical Review B* **2016**, *94*, 201107(R).

[222] Watson, M. D.; Kim, T. K.; Haghighirad, A. A.; Davies, N. R.; McCollam, A.; Narayanan, A.; Blake, S. F.; Chen, Y. L.; Ghannadzadeh, S.; Schofield, A. J., et al. *Physical Review B* **2015**, *91*, 155106.

[223] Chubukov, A. V.; Fernandes, R. M.; Schmalian, J. *Physical Review B* **2015**, *91*, 201105(R).

[224] Qin, S.; Hu, L.; Wu, X.; Dai, X.; Fang, C.; Zhang, F.-c.; Hu, J. *arXiv preprint arXiv:1901.03120* **2019**,

[225] Liu, Q. et al. *Physical Review X* **2018**, *8*, 041056.

[226] Ma, M.; Wang, L.; Bourges, P.; Sidis, Y.; Danilkin, S.; Li, Y. *Physical Review B* **2017**, *95*, 100504(R).

[227] Calder, S. et al. *Review of Scientific Instruments* **2018**, *89*, 092701.

[228] Davies, N. R.; Rahn, M. C.; Walker, H. C.; Ewings, R. A.; Woodruff, D. N.; Clarke, S. J.; Boothroyd, A. T. *Physical Review B* **2016**, *94*, 144503.

[229] Pan, B.; Shen, Y.; Hu, D.; Feng, Y.; Park, J.; Christianson, A.; Wang, Q.; Hao, Y.; Wo, H.; Yin, Z. *Nature Communications* **2017**, *8*, 123.

[230] Woodruff, D. N.; Schild, F.; Topping, C. V.; Cassidy, S. J.; Blandy, J. N.; Blundell, S. J.; Thompson, A. L.; Clarke, S. J. *Inorganic Chemistry* **2016**, *55*, 9886–9891.

[231] Gu, Q.; Tang, Q.; Wan, S.; Du, Z.; Yang, X.; Yang, H.; Wang, Q.-H.; Lin, H.; Zhu, X.; Wen, H.-H. *Physical Review B* **2018**, *98*, 134503.

[232] Du, Z.; Yang, X.; Altenfeld, D.; Gu, Q.; Yang, H.; Eremin, I.; Hirschfeld, P. J.; Mazin, I. I.; Lin, H.; Zhu, X., et al. *Nature Physics* **2018**, *14*, 134.

[233] Zhou, H.; Ni, S.; Yuan, J.; Li, J.; Feng, Z.; Jiang, X.; Huang, Y.; Liu, S.; Mao, Y.; Zhou, F., et al. *Chinese Physics B* **2017**, *26*, 057402.

[234] Mao, Y.; Li, Z.; Zhou, H.; Ma, M.; Chai, K.; Ni, S.; Liu, S.; Tian, J.; Huang, Y.; Yuan, J., et al. *Chinese Physics B* **2018**, *27*, 077405.

[235] Prozorov, R.; Kogan, V. G. *Physical Review Applied* **2018**, *10*, 014030.

[236] Urban, C.; Valmianski, I.; Pachmayr, U.; Basaran, A. C.; Johrendt, D.; Schuller, I. K. *Physical Review B* **2018**, *97*, 024516.

[237] Khasanov, R.; Zhou, H.; Amato, A.; Guguchia, Z.; Morenzoni, E.; Dong, X.; Zhang, G.; Zhao, Z. *Physical Review B* **2016**, *93*, 224512.

[238] Wang, C.; Yi, X.; Sun, X.; Tang, Q.; Qiu, Y.; Luo, Y.; Yu, B. *Superconductor Science and Technology* **2017**, *30*, 085004.

[239] Du, Z.; Yang, X.; Lin, H.; Fang, D.; Du, G.; Xing, J.; Yang, H.; Zhu, X.; Wen, H.-H. *Nature Communications* **2016**, *7*, 10565.

[240] Wang, C.; Yi, X.; Qiu, Y.; Tang, Q.; Zhang, X.; Luo, Y.; Yu, B. *Superconductor Science and Technology* **2016**, *29*, 055003.

[241] Lin, H.; Xing, J.; Zhu, X.; Yang, H.; Wen, H.-H. *Science China Physics, Mechanics & Astronomy* **2016**, *59*, 657404.

[242] Wang, Z.; Yuan, J.; Wosnitza, J.; Zhou, H.; Huang, Y.; Jin, K.; Zhou, F.; Dong, X.; Zhao, Z. *Journal of Physics: Condensed Matter* **2016**, *29*, 025701.

[243] Yi, X.; Wang, C.; Tang, Q.; Peng, T.; Qiu, Y.; Xu, J.; Sun, H.; Luo, Y.; Yu, B. *Superconductor Science and Technology* **2016**, *29*, 105015.

[244] Lu, X. F.; Wang, N. Z.; Luo, X. G.; Zhang, G. H.; Gong, X. L.; Huang, F. Q.; Chen, X. H. *Physical Review B* **2014**, *90*, 214520.

[245] Cava, R. *Science* **1990**, *247*, 656–662.

[246] Gao, Z.; Zeng, S.; Zhu, B.; Li, B.; Hao, Q.; Hu, Y.; Wang, D.; Tang, K. *Sci. China Mater.* **2018**, *61*, 977–984.

[247] Stahl, J.; Shlaen, E.; Singer, H.; Johrendt, D. *Dalton Transactions* **2018**, *47*, 3264–3271.

[248] Wu, D.; Guo, Z.; Liu, N.; Zhou, L.; Mao, Y.; Wan, L.; Sun, F.; Yuan, W. *Inorg. Chem. Commun.* **2018**, *91*, 72–76.

[249] Windwer, S.; Sundheim, B. R. *The Journal of Physical Chemistry* **1962**, *66*, 1254–1258.

[250] Zurek, E. *Journal of the American Chemical Society* **2011**, *133*, 4829–4839.

[251] Cotton, F. A.; Wilkinson, G.; Murillo, C. A.; Bochmann, M.; Grimes, R. *Advanced inorganic chemistry*; Wiley New York, 1988; Vol. 5.

[252] Hatakeda, T.; Noji, T.; Sato, K.; Kawamata, T.; Kato, M.; Koike, Y. *J. Phys. Soc. Jpn.* **2016**, *85*, 103702.

[253] Xu, H.; Wang, X.; Gao, Z.; Huang, H.; Long, Y.; Lu, Y.; Tang, K. *J. Alloys Compd.* **2018**, *735*, 2053–2057.

[254] Guo, Z.; Zhou, L.; Jin, S.; Han, B.; Sun, F.; Yuan, W. *RSC Adv.* **2017**, *7*, 17539–17544.

[255] Zhao, L.; Liang, A.; Yuan, D.; Hu, Y.; Liu, D.; Huang, J.; He, S.; Shen, B.; Xu, Y.; Liu, X., et al. *Nature Communications* **2016**, *7*, 10608.

[256] Zhou, X.; Wilfong, B.; Liou, S.-C.; Hodovanets, H.; Brown, C. M.; Rodriguez, E. E. *Chem. Comm.* **2018**,

[257] Toh, M.; Tan, K.; Wei, F.; Zhang, K.; Jiang, H.; Kloc, C. *Journal of Solid State Chemistry* **2013**, *198*, 224–230.

[258] Hatakeda, T.; Noji, T.; Hosono, S.; Kawamata, T.; Kato, M.; Koike, Y. J. Phys.: Conf. Series. 2014; p 022032.

[259] Dines, M.; Levy, R. *The Journal of Physical Chemistry* **1975**, *79*, 1979–1982.

[260] Brown, L. A.; Glaunsinger, W. S.; McKelvy, M. J. *Journal of Solid State Chemistry* **1999**, *147*, 38–44.

[261] Silbernagel, B.; Dines, M.; Gamble, F.; Gebhard, L.; Whittingham, M. *The Journal of Chemical Physics* **1976**, *65*, 1906–1913.

[262] Gamble, F.; Silbernagel, B. *The Journal of Chemical Physics* **1975**, *63*, 2544–2552.

[263] Young Jr, V.; McKelvy, M.; Glaunsinger, W.; Von Dreele, R. *Chemistry of Materials* **1990**, *2*, 75–81.

[264] McKelvy, M.; Glaunsinger, W. *Solid State Ionics* **1987**, *25*, 287–294.

[265] Dunn, J. M.; Glaunsinger, W. S. *Solid State Ionics* **1988**, *27*, 285–294.

[266] Bouwmeester, H.; Wiegers, G. *Journal of Solid State Chemistry* **1988**, *76*, 391–397.

[267] Bernard, L.; McKelvy, M.; Glaunsinger, W.; Colombet, P. *Solid State Ionics* **1985**, *15*, 301–310.

[268] Young Jr, V.; McKelvy, M.; Glaunsinger, W.; Von Dreele, R. *Solid state ionics* **1988**, *26*, 47–54.

[269] Schöllhorn, R.; Zagefka, H.-D. *Angewandte Chemie International Edition in English* **1977**, *16*, 199–200.

[270] Vaqueiro, P. *Inorganic chemistry* **2006**, *45*, 4150–4156.

[271] Vaqueiro, P.; Darlow, D. P.; Powell, A. V.; Chippindale, A. M. *Solid State Ionics* **2004**, *172*, 601–605.

[272] Feng, M.-L.; Ye, D.; Huang, X.-Y. *Inorganic chemistry* **2009**, *48*, 8060–8062.

[273] Feng, M.-L.; Li, P.-X.; Du, K.-Z.; Huang, X.-Y. *European Journal of Inorganic Chemistry* **2011**, *2011*, 3881–3885.

[274] Bensch, W.; Näther, C.; Schur, M. *Chemical Communications* **1997**, 1773–1774.

[275] Schur, M.; Bensch, W. *Zeitschrift für Naturforschung B* **2002**, *57*, 1–7.

[276] Wu, M.; Rhee, J.; Emge, T. J.; Yao, H.; Cheng, J.-H.; Thiagarajan, S.; Croft, M.; Yang, R.; Li, J. *Chemical communications* **2010**, *46*, 1649–1651.

[277] Greenfield, J. T.; Pak, C.; Kamali, S.; Lee, K.; Kovnir, K. *Chemical Communications* **2015**, *51*, 5355–5358.

[278] Pak, C.; Kamali, S.; Pham, J.; Lee, K.; Greenfield, J. T.; Kovnir, K. *Journal of the American Chemical Society* **2013**, *135*, 19111–19114.

[279] Li, W.; Xia, F.; Qu, J.; Li, P.; Chen, D.; Chen, Z.; Yu, Y.; Lu, Y.; Caruso, R. A.; Song, W. *Nano Research* **2014**, *7*, 903–916.

[280] Gao, Q.; Chen, P.; Zhang, Y.; Tang, Y. *Advanced Materials* **2008**, *20*, 1837–1842.

[281] Ogata, H.; Fujimori, H.; Miyajima, S.; Kobashi, K.; Chiba, T.; Taylor, R. E.; Endo, K. *Journal of Physics and Chemistry of Solids* **1997**, *58*, 701–710.

[282] Chen, Z.; Dilks, R. E.; Wang, R.-J.; Lu, J. Y.; Li, J. *Chemistry of materials* **1998**, *10*, 3184–3188.

[283] Spetzler, V.; Rijnberk, H.; Naether, C.; Bensch, W. *Zeitschrift für anorganische und allgemeine Chemie* **2004**, *630*, 142–148.

[284] Hathaway, B.; Wilkinson, G.; Gillard, R.; McCleverty, J. *The synthesis, reactions, properties and applications of coordination compounds* **1987**, *5*, 533–774.

[285] Li, J.; Chen, Z.; Wang, R.-J.; Proserpio, D. M. *Coordination Chemistry Reviews* **1999**, *190*, 707–735.

[286] Sharma, J.; Jiang, Z.; Bhutani, A.; Behera, P.; Shoemaker, D. P. *CrystEngComm* **2019**, *21*, 2718–2726.

[287] Alexander, M. D.; Spillert, C. A. *Inorganic Chemistry* **1970**, *9*, 2344–2346.

[288] Childers Jr, R. F.; Vander Zyl Jr, K.; House, D. A.; Hughes, R. G.; Garner, C. S. *Inorganic Chemistry* **1968**, *7*, 749–754.

[289] Schwarzenbach, G.; Magyar, B. *Helvetica Chimica Acta* **1962**, *45*, 1454–1457.

[290] Allen, F. H.; Bird, C. M.; Rowland, R. S.; Raithby, P. *Acta Crystallographica Section B: Structural Science* **1997**, *53*, 680–695.

[291] Miao, X.; Terao, T.; Yang, X.; Nishiyama, S.; Miyazaki, T.; Goto, H.; Iwasa, Y.; Kubozono, Y. *Phys. Rev. B.* **2017**, *96*, 014502.

[292] Denholme, S.; Demura, S.; Okazaki, H.; Hara, H.; Deguchi, K.; Fujioka, M.; Ozaki, T.; Yamaguchi, T.; Takeya, H.; Takano, Y. *Mater. Chem. Phys.* **2014**, *147*, 50–56.